Phospho-signal flow from a pole-localized microdomain spatially patterns transcription factor activity

Keren Lasker,[1,4] Alex von Diezmann,[2,4] Daniel G. Ahrens,[1] Thomas H. Mann,[1]

W. E. Moerner,[2] and Lucy Shapiro[1,3,*]

[1]Department of Developmental Biology, Stanford University School of Medicine, Stanford, CA 94305

[2]Department of Chemistry, Stanford University, Stanford, CA 94305

[3]Chan Zuckerberg Biohub, San Francisco, CA 94158

[4]Co-first author

*Correspondence: shapiro@stanford.edu

Keywords: bacteria, polarity, phospho-gradient, single molecule tracking, reaction-diffusion modeling, membrane-less microdomains

SUMMARY

Selective recruitment and concentration of signaling proteins within membrane-less compartments is a ubiquitous mechanism for subcellular organization. However, little is known about the effects of such a dynamic recruitment mechanism on intracellular signaling. Here, we combined transcriptional profiling, reaction-diffusion modeling, and single-molecule tracking to study signal exchange in and out of a microdomain at the cell pole of the asymmetrically dividing bacterium *Caulobacter crescentus*. Our study revealed that the microdomain is selectively permeable, and that each protein in the signaling pathway that activates the cell fate transcription factor CtrA is sequestered and uniformly concentrated within the microdomain or its proximal membrane. Restricted rates of entry into and escape from the microdomain enhance phospho-signaling, leading to a sublinear gradient of CtrA~P along the long axis of the cell. The spatial patterning of CtrA~P creates a gradient of transcriptional activation that serves to prime asymmetric development of the two daughter cells.

INTRODUCTION

The ability of a cell to recruit and coalesce biochemically-related components at specific subcellular sites is crucial for achieving functional complexity and different cell fates across all kingdoms of life (Misteli, 2007; Rudner and Losick, 2010; Shapiro et al., 2009; Slaughter et al., 2009; Wodarz, 2002). While the mechanisms controlling the formation and composition of subcellular domains are increasingly understood, less is known about the spatial and temporal implications of reactions taking place within them. In *Caulobacter crescentus*, the disordered polar organizing protein PopZ establishes a space-filling ~100-200 nm microdomain adjacent to the cell pole that is not encapsulated by a protein shell or a membrane (Bowman et al., 2010; Bowman et

al., 2008; Ebersbach et al., 2008; Gahlmann et al., 2013). Here we show that this polar microdomain selectively recruits members of the phospho-signaling pathway that culminates in the activation of the master transcription factor CtrA. We further provide a mechanism for how the concentration and motion of these proteins within the microdomain regulates spatially constrained gene expression and the establishment of asymmetry in the predivisional cell.

Caulobacter divides to produce two morphologically distinct daughter cells: a sessile stalked cell that replicates its chromosome following division, and a motile swarmer cell in which chromosome replication is delayed until it differentiates into a stalked cell (Figure 1A, right). This developmental asymmetry is governed by differentially-localized groups of signaling proteins at the two cell poles (Lasker et al., 2016). The localization of these signaling proteins is dependent on the polar organizing protein PopZ that self-assembles into a branched network of filaments *in vitro* and creates a space-filling microdomain at the cell poles *in vivo* (Bowman et al., 2010; Bowman et al., 2008; Gahlmann et al., 2013). PopZ directly binds at least nine proteins that temporally and spatially regulate cell cycle progression, and deletion of the *popZ* gene leads to delocalization of these proteins and to severe cell cycle defects (Bowman et al., 2010; Bowman et al., 2008; Ebersbach et al., 2008; Holmes et al., 2016; Mignolet et al., 2016; Ptacin et al., 2014). Among these binding partners are two signaling proteins that together play a key role in controlling the levels and activity of the master transcription factor CtrA: the membrane-bound hybrid histidine kinase CckA, which acts as the phosphate source for CtrA, and the small cytoplasmic protein ChpT, which shuttles phosphate from CckA to the master transcription factor CtrA (Figure 1A). In its active phosphorylated form (CtrA~P), CtrA controls the transcription of over 100 genes, including those that are necessary for the formation of the nascent swarmer cell, including the flagellar and chemotaxis transcriptional hierarchy (Figure 1A) (Ardissone and Viollier, 2015; Laub

et al., 2002; Laub et al., 2000). CtrA~P also serves to inhibit the initiation of DNA replication in the swarmer cell by binding to the chromosome origin (Quon et al., 1998). CtrA levels and activity vary as a function of the cell cycle. In swarmer cells, high CtrA~P levels promote the swarmer fate. During the swarmer to stalk cell transition CtrA~P is cleared from the cell to allow initiation of DNA replication. In predivisional cells, CtrA proteolysis ceases and its synthesis and activation resumes. Upon cell compartmentalization but prior to division, CtrA~P is proteolyzed in the stalked compartment, while active CtrA~P remains in the swarmer compartment.

CckA's auto-kinase activity is density-dependent and occurs only when CckA is concentrated at the new pole microdomain of the predivisional cell, where it drives phosphorylation of CtrA (Iniesta et al., 2010a; Jacobs et al., 2003; Jonas et al., 2011; Mann et al., 2016; Tsokos et al., 2011). In contrast, CckA acts as a phosphatase everywhere else in the cell with density-independent activity (Mann et al., 2016). The antagonism between CckA acting as a kinase and as a phosphatase resembles the process by which concentration gradients are formed in much larger eukaryotic cells and tissues (Wartlick et al., 2009).

For the cytosolic ChpT phospho-transfer protein to interact with CckA at the membrane of the new pole, it must pass through the space-filling PopZ microdomain. ChpT~P must then phosphorylate CtrA to complete the signaling pathway. Thus, critical questions are if (and how) the PopZ microdomain influences access of ChpT to the CckA kinase, where ChpT~P encounters CtrA, and ultimately, what spatial distribution of CtrA~P is established as it emanates from the new pole microdomain. With spatially resolved transcriptional measurements as a proxy for CtrA~P activity, we demonstrate that predivisional cells exhibit a sublinear (approximately exponential) gradient of activated CtrA~P emanating from the new cell pole. By imaging the single-molecule trajectories of CckA, ChpT and CtrA relative to the super-resolved PopZ

microdomain, we show that in addition to acting as a localization factor, the microdomain sequesters each member of the CtrA phospho-transfer pathway and restricts the rate at which molecules within the microdomain exchange with the rest of the cell, while restricting polar access for other molecules. Integrating this knowledge with other biochemical data in a comprehensive reaction-diffusion model, we show that both high concentration and slow turnover at the poles are necessary to generate a gradient of CtrA~P activity, in quantitative agreement with our transcriptional measurements. These results demonstrate that a bacterial microdomain adjacent to the cell pole selectively sequesters a phospho-signaling pathway to establish a spatial trajectory of information transfer that controls chromosome readout.

RESULTS

The CtrA activation pathway is sequestered within the PopZ microdomain

To understand the influence of the PopZ microdomain on the CtrA activation pathway, we began by determining to what extent the pathway's proteins were colocalized with PopZ at the old and new poles of predivisional cells. We replaced native *popZ* with an allele for the (photo-activatable) fluorescent protein fusion *PAmCherry-popZ* (Figure S1A, Tables S1-S3). We observed that PopZ forms foci at both poles in predivisional cells as previously shown (Bowman et al., 2008; Ebersbach et al., 2008), with 55% of its signal localized to the old pole and 31% to the new pole on average (Figures 1B-D, S1B). Using strains expressing enhanced yellow fluorescent protein (eYFP) fused to either CckA, ChpT, or CtrA, we measured the co-localization of each pathway component with respect to PAmCherry-PopZ (Figure S1) (at diffraction-limited 200 nm resolution, also see Figures 4 and 5). Consistent with previous studies (Ebersbach et al., 2008), we found that CckA-eYFP co-localized with PopZ at both the new pole and the old pole, with 60% of

total CckA fluorescence intensity localized to the new pole and 27% localized to the old pole (Figure 1B). While CckA clearly associates with PopZ (Holmes et al., 2016), CckA exhibits a greater concentration at the new pole due to additional pole-specific localization factors (Iniesta et al., 2010a). The cytosolic phosphotransferase ChpT, like its interacting membrane histidine kinase CckA, was shown to bind PopZ *in vivo* using the heterologous *Escherichia coli* system (Holmes et al., 2016). We thus speculated that PopZ-binding interactions would also cause ChpT to be enriched within the PopZ microdomain in *Caulobacter*. Indeed, ChpT formed foci at both poles of the cells, with 22% of ChpT signal localized to the new pole and 34% of the signal localized to the old pole (Figures 1C, S1B). While ChpT weakly binds CckA *in vitro* (Blair et al., 2013), ChpT did not show greater localization at the new pole, where most of CckA molecules reside. These results suggest that PopZ is a critical polar localization factor for ChpT in *Caulobacter*.

Unlike ChpT and CckA, CtrA does not colocalize with PopZ when heterologously expressed in *E. coli*, suggesting that binding interactions between CtrA and PopZ are weak or nonexistent (Holmes et al., 2016). We asked whether CtrA forms a focus within the PopZ microdomain in *Caulobacter* without direct binding to PopZ, as does the cytosolic protein DivK (Holmes et al., 2016; Lam et al., 2003). Previous imaging of an N-terminal YFP fusion to CtrA in predivisional cells showed a large diffuse population of CtrA with transient accumulation at the old cell pole prior to proteolysis, independent of CtrA's phosphorylation state or its degradation motif (Ryan et al., 2004), while no CtrA accumulation was detected at the new pole. Because the N-terminal domain of CtrA is important for function, we repeated this experiment using a sandwich fusion that integrated eYFP between CtrA's DNA binding domain and its 14-residue C-terminal degradation tag (Figure S1A) (CtrA-eYFP-14). We observed a localization profile of CtrA-eYFP-14 in synchronized predivisional cells (Figure S1C) in which 17% of the fluorescent

signal was at the new pole and 28% of the signal was located at the old pole. Altogether, our imaging results show that all three members of the phospho-signaling pathway are greatly enriched within the PopZ microdomains of the *Caulobacter* cell.

CtrA exhibits a gradient of activity in predivisional cells

We designed a transcription assay as a proxy for measuring the CtrA~P spatial profile and used it to determine whether polar accumulation of the proteins in the CtrA activation pathway regulates the distribution of CtrA~P across the cell. We introduced a CtrA~P activated promoter (P_{350}, from the CCNA_00350 operon) driving an *eyfp* gene at four different sites along the right arm of *Caulobacter*'s single circular chromosome (loci L1-L4) (Figure 2A, Table S4). Locus L1 is adjacent to the replication origin, which is positioned near the cell pole, while locus L4 is positioned near the chromosome terminus (Figure 2A). Because the position of any given gene on the *Caulobacter* chromosome reflects its position within the cell (Viollier et al., 2004), we can approximate the spatial position of loci L1-L4 within the cell and their time of replication (SI, Table S4).

We used reverse transcription quantitative PCR (RT-qPCR) (Heid et al., 1996) to measure the reporter *eyfp* mRNA transcribed from each locus L1-L4 in synchronized populations beginning from swarmer cells (Figure 2A). This allowed us to quantitatively and directly compare the activity of CtrA~P regulated promoters from each spatial position over the course of the cell cycle. For clarity, we report the transcriptional output relative to the 5-minutes time point of L1 (1 AU). Over the course of the experiment, the single chromosome replicates once. Thus, the replication of the single starting chromosome completes once, thus the output of each locus should double upon replication of that locus on the chromosome. While transcription from all four integration loci

remained low during the first 60 minutes of the cell cycle, the loci began to diverge at the onset of CtrA activation in pre-divisional cells. Critically, at the 90-minutes time point, transcriptional activity at site L1 peaked to 5.5±0.11 AU, while transcription from site 2 peaked to 2.5±0.25 AU, even though both sites had been duplicated far earlier (Figure 2A, Table S4). Transcription from sites L2-L4 peaked at the 120-minute time point, upon completion of DNA replication, with 1.6±0.67 AU and 1.8±0.42 AU for sites L3 and L4 (Figure 2A). As a control for CtrA-independent regulation, the transcription of *eyfp* under the xylose-inducible P_{xylX} promoter showed a ≤ 2-fold increase resulting from chromosome duplication (Figure S2A). In addition, the transcription of *eyfp* under another CtrA regulated promoter P_{pilA} showed chromosome position-specific effects (Figure S2B). Finally, comparing the cumulative occurrences of CtrA ChIP-seq peaks and CtrA binding motifs we observed that despite uniform distribution of CtrA binding motifs across the chromosome, CtrA distribution on the chromosome is not uniform and exhibits a larger concentration of CtrA molecules in the origin-proximal region (Figure 2SC). These results indicate that the activated CtrA~P transcription factor exhibits spatial control of promoter activity, with highest transcription from loci positioned near the newly replicated origin of replication at the new cell pole.

To test our hypothesis that the gradient of CtrA activity results from the spatial regulation of CckA and ChpT activity, we deleted the native *ctrA* gene in the presence of a plasmid-borne, xylose-inducible phosphomimetic mutant, *ctrA*(*D51E*) (Figure 2B). This mutant cannot accept a phosphate, but the glutamate replacing the aspartate results in constitutive CtrA activity, (Domian et al., 1997), decoupling it from the CckA-ChpT phospho-transfer pathway. When *ctrA*(*D51E*) was expressed as the sole copy of CtrA, position-specific effects on transcription from the CtrA-activated P_{350} promoter were lost, demonstrating that the gradient in CtrA activity depended on

the signaling cascade emanating from the cell pole. This effect was not due to changing protein levels, as xylose-induced expression of a plasmid-borne wildtype *ctrA* still resulted in a gradient of P_{350} activity (Figure 2B). Collectively, these experiments argue that localized activity of the CckA phospho-signaling pathway leads to a gradient in CtrA~P and spatial control of CtrA-controlled promoters.

Accumulation of phospho-relay components in the PopZ microdomain governs CtrA~P levels and spatial distribution.

Using previously published biochemical data, we quantitatively interpreted the results of our RT-qPCR experiments to define potential CtrA~P distributions within the cell. Our observation that CtrA~P-regulated promoter activity depended on the promoter's position within the cell indicates a gradient of CtrA~P emanating from the new cell pole. However, the distribution of CtrA~P may not be identical to the gradient in transcriptional activity: CtrA~P binds cooperatively to the P_{ccrM} and P_{fliQ} promoters (Reisenauer et al., 1999; Siam and Marczynski, 2000), and because CtrA~P binds P_{350} as a dimer (Zhou et al., 2015), it is likely to exhibit cooperative activity when promoting the transcription of *350* mRNA as well. Accordingly, we modeled the transcriptional response from P_{350} as a Hill function, with fitting parameters based on previously measured CtrA copy number and cell cycle dependent transcription of *350* (Schrader et al., 2016) (Equation S7, Figure S3A). We examined the effect of several different shapes of CtrA~P gradients on the transcriptional output from the four (L1-L4) integration sites (Figures 3A and 3B). An exponential decrease in CtrA~P levels best reflected the 2-fold decrease in mRNA levels from L2 and a 5 fold decrease in mRNA levels from L3 and L4, with respect to mRNA levels from locus 1 (Figures 3A and 3B *III*). Thus, we concluded that the observed drop in transcriptional activity as a function of

distance of the integration site from the origin is likely the result of an exponential or other sublinear decay in CtrA~P levels from the new pole to the old pole.

The canonical model for forming a gradient of the phosphorylated state of a signal requires that phosphorylation and dephosphorylation events occur at separate cellular locations and that the kinetics of phosphatase activity is fast relative to the diffusion of the signal (Barkai and Shilo, 2009; Brown and Kholodenko, 1999; Kiekebusch and Thanbichler, 2014; Wartlick et al., 2009). As all members of the CtrA activation pathway accumulate inside the PopZ microdomain (Figure 1B-D) we turned to mathematical modeling to explore how this accumulation affects gradient formation properties. We defined a reaction-diffusion model in which a set of partial differential equations track the concentrations of CckA, ChpT, CtrA as a function of diffusion and biochemical interactions inside and outside of the PopZ microdomains (Figures 3C and S3, Table S6). To identify the biochemical parameters that are most important for setting the gradient of CtrA activity, we performed a global sensitivity analysis of our model (SI). We explored the sensitivity of the amplitude and shape of the CtrA~P gradient to changes in the binding affinity to the microdomain, rates of phospho-transfer, and diffusion coefficients inside and outside the microdomain. To reflect the possibility that the PopZ microdomain environment is different at the two cell poles, we also allowed for differential diffusivity and binding rates inside the two microdomains. By comparing the steady-state CtrA~P profiles across these different parameter values, we calculated 'amplitude sensitivity' (total CtrA~P copies in the cell), and 'distribution sensitivity' (the ratio between sum of CtrA~P molecules from the two halves of the cell) for each parameter we had varied.

The amplitude of CtrA~P was highly sensitive to alterations in the K_D of binding between CckA and the new pole microdomain as well as the phospho-transfer rate between CckA to ChpT

(Figure 3C, upper heatmap, Figure 3D). Changing the K_D between CckA and the new pole microdomain alters the concentration of CckA, and because CckA's kinase activity increases nonlinearly with increasing concentration (Mann et al., 2016), this greatly increases the rate at which phosphate is introduced into the pathway (Figure 3D). Meanwhile, faster phospho-transfer rates between CckA and ChpT and between ChpT and CtrA increase the fraction of CtrA~P molecules that is generated at the new pole microdomain, near the CckA source of phosphate.

The distribution of CtrA~P was highly sensitive to changes in ChpT and CtrA binding to the microdomain at the new pole, as well as to CtrA diffusion in the body of the cell (Figure 3C lower heatmap, Figure 3E). Weakening the K_D of ChpT or CtrA for the new pole microdomain led to a shallower gradient across the cell, with a larger contribution from ChpT. Strong interactions between both proteins and the new pole were critical to achieve a CtrA~P distribution that, *in-silico*, recapitulates the transcriptional measurements (Figure 3D). These results suggest that the spatial position of the phospho-transfer between ChpT and CtrA can modulate the shape of the gradient. Additionally, it was critical that CtrA diffusivity in the body not be substantially higher than the effective kinetics of phospho-transfer, as this would disrupt any gradient. Collectively, our model predicts a critical role of the PopZ microdomain in modulating the behavior of the components of phospho-transfer cascade.

CckA molecules are concentrated and their diffusion is slowed within the polar PopZ microdomain

The results of our sensitivity analysis (Figure 3) strongly suggested that the formation of an exponential gradient of CtrA~P depends on the dense concentration and slow diffusion of phospho-signal pathway proteins within the PopZ microdomain. To directly visualize these

properties, we turned to single-molecule tracking of the CtrA pathway proteins combined with super-resolution microscopy of the static PopZ microdomain, beginning with CckA. Because CckA is associated with the curved inner membrane, single-molecule tracks generated from two-dimensional (2D) measurements would appear distorted at the "sides" of the cell, leading to erroneously low estimates of diffusivity in these regions (Figure S4A). Therefore, we used an engineered point spread function (the DH-PSF) (Gahlmann et al., 2013) to localize and follow the motion of CckA-eYFP molecules in three dimensions (3D), avoiding the 30% errors that would be present for 2D trajectories of membrane proteins (Figures S4B and S4C).

By correlating our tracking measurements with 3D super-resolution imaging of a xylose-induced copy of PAmCherry-PopZ in a merodiploid background, we precisely defined what parts of the CckA-eYFP trajectories explored the membrane area of the PopZ microdomains at the new and old poles (Figure 4A). Using mean-squared-displacement (MSD) analysis, we found that CckA diffused most rapidly in the cell body, 2-fold slower in the old pole, and 4-fold slower in the new pole ($D = 0.0082 \pm 0.0020$, 0.0040 ± 0.0014, and 0.0022 ± 0.0013 $\mu m^2/s$, respectively) (Figure 4B). One certain cause for the reduction in diffusivity at the poles is polar binding interactions, both to PopZ and to CckA-specific localization factors at the new pole (Holmes et al., 2016; Iniesta et al., 2010a). Another likely cause is the formation of higher-order CckA assemblies (Mann et al., 2016), which would presumably be enhanced at the high CckA concentrations within the new pole (and to a lesser extent, within the old pole).

To define the average nanoscale distribution of CckA at the new and old poles, we combined CckA and PopZ high-resolution localization data from many individual microdomains (SI). We found that CckA molecules were distributed roughly evenly throughout the 3D membrane region adjacent to PopZ, and that the CckA concentration dropped off sharply away from the

microdomain (Figure 4C, Figure S4D). While the uniform density in the averaged CckA distribution does not preclude the possibility of individual CckA clusters within microdomains (as has been suggested in PopZ overexpression experiments (Ebersbach et al., 2008)) it clearly indicates that CckA does not have a preference for particular positions within the PopZ microdomain. CckA formed a hemispherical cup surrounding PopZ in old poles (Figure 4C), while in new poles, the PopZ microdomain took up a smaller volume, and CckA occupied a proportionally smaller area on the new pole membrane (Figure S4D). Notably, the area taken up by CckA at the new pole was lower despite having a higher total number of CckA molecules (Figure 1C). Combining our measurements of polar radii (r = 108 nm for old poles, and r = 82 nm for new poles) with estimates of the total number of CckA molecules at both poles, we estimated a CckA concentration of ~5,000-10,000 and 1,250 molecules/μm^2 for the new and old poles, respectively, more than 100x greater than the concentration in the cell body (9 molecules/μm^2) (SI). The estimated concentration of CckA at the new pole agrees with the previously determined CckA concentration on liposomes *in vitro* that leads to maximum autokinase activity, while the estimated CckA concentration at the old pole was shown *in vitro* to lead to little or no autokinase activity (Mann et al., 2016).

To determine whether CckA was free to enter and exit the pole over a longer timescale than seconds, we used a diffraction-limited confocal microscope to photobleach CckA at the old pole. We then measured the timescale of fluorescence recovery and loss at the old and new poles (Figure 4D and Figure S5). While targeted photobleaching depleted ~30% of the total cell fluorescence, we found that the ratio of CckA within the new and old poles was restored close to its pre-bleach value after 10 minutes. This was consistent with reaction-diffusion simulations using the experimentally measured diffusivities and assuming transient binding of CckA to species

within the microdomain (Figure S5). Thus, while CckA recovery was slower than would be expected for free diffusion, CckA was still mobile and not irreversibly bound within the polar microdomain. Collectively, the CckA tracking and photobleaching experiments indicate that CckA is concentrated throughout the polar membrane cap of the PopZ microdomain by crowding and reversible binding to other proteins within the microdomain.

ChpT and CtrA molecules are transiently sequestered within the PopZ microdomain volume

We used our correlative single-molecule tracking and super-resolution imaging approach to study the cytoplasmic members of the signaling pathway, ChpT and CtrA, to ascertain their diffusion coefficients, distributions, and residence times within the polar PopZ microdomains. ChpT-eYFP molecules outside the poles diffused rapidly throughout the cell, but were captured within the PopZ volume upon reaching the poles (Figure 5A). While most captured ChpT molecules appeared to diffuse throughout the microdomain volume, a fraction of ChpT-eYFP trajectories exhibited motion only in the plane of the polar membrane (Figure 5B), suggestive of binding to CckA. Similar to ChpT, we observed that CtrA-eYFP-14 entered and was slowed within the PopZ microdomain (Figure 5C). CtrA and ChpT molecules exited the microdomain after a short time period (Figure 5D; ChpT not shown) and immediately regained their previous diffusivity within the cell body.

We combined high-resolution single-molecule data from many predivisional cells to generate average localization profiles of CtrA, ChpT, and PopZ (Figure 5E and Figure S6). As in our diffraction-limited images (Figure 1D-E), while ChpT and CtrA were present throughout the cell, they were much more concentrated at the cell poles, with ChpT being somewhat more concentrated than CtrA. In addition, the higher-resolution single-molecule distribution clearly

indicated that ChpT and CtrA entered the microdomain and were distributed throughout the PopZ volume. As CtrA does not have affinity for PopZ but does bind ChpT (Blair et al., 2013; Holmes et al., 2016), this suggests that ChpT molecules embedded in the microdomain act as binding partners to indirectly recruit CtrA. We also observed a slight enrichment of CtrA at the cytoplasmic face of the microdomain at both the new and old poles, ~50-100 nm from the PopZ centroid (shoulders on green curves in Figure 5E). This may result from CtrA binding to the chromosome origin sequence *ori*, which CtrA binds with nM affinity (Siam and Marczynski, 2000), and is likely within 150 nm of PopZ based on previous super-resolution and chromosome imaging experiments. (Hong et al., 2013; Ptacin et al., 2014).

We used MSD analysis to quantify the diffusivity of ChpT and CtrA, projecting motion onto the 1D cell axis to avoid confinement effects arising from the narrow cell width (Figure 5F). Both ChpT and CtrA exhibited anomalous subdiffusive motion in the cell body, apparent as a slope less than 1 in the log-log MSD plot. Given the short length of our eYFP trajectories, fits to these curves only allowed us to bound the subdiffusive expontent α, indicating $\alpha < 0.7$ and a short-timescale apparent diffusivity $D_{app} = 1.8$ $\mu m^2/s$ (SI, Figure S6). We also observed anomalous subdiffusion in trajectories of free eYFP, which we do not expect to directly bind any targets in *Caulobacter* (Figure S6). Thus, subdiffusion in the cell body likely results from general properties such as crowding in the cytoplasm and obstruction by the nucleoid.

Within the poles, both ChpT and CtrA exhibited MSD values an order of magnitude lower than in the cell body (Figure 5F). ChpT molecules explored the pole on a timescale comparable to our 20 ms integration time (Figure 5A), causing the MSD to immediately reach an asymptotic limit of $\sim 10^{-2.5}$ μm^2 (3x higher than our 24 nm localization precision) independent of lag, implying $D \geq 0.1$ $\mu m^2/s$. We analytically confirmed that this limit is to be expected given the geometry of the

PopZ microdomain, and calculated that free motion within spheroids of 150-200 nm diameter would give rise to asymptotic MSDs of $10^{-2.6}$ to $10^{-2.4}$ (SI). In contrast, polar CtrA exhibited a steady increase of its MSD between the limits of error and free diffusion, as expected from our observation of tracks that slowly explored the PopZ microdomain (Figure 5D), and fits to these data gave $D \approx 0.01$ $\mu m^2/s$ (Figure S6). Overall, these results show that both ChpT and CtrA were relatively free to explore the polar space in which they were concentrated.

We determined the rate of ChpT and CtrA turnover at the poles by calculating the dwell times of eYFP-labeled molecules within the microdomain before returning to the cell body (Figure 5G). The apparent exit rates of both ChpT and CtrA were increased due to competition between true exit events and the rapid photobleaching of eYFP labels. We compensated for this effect by approximating photobleaching and exit as competing exponential processes, scaling the rates by the proportion of tracks that exited before photobleaching (SI). This approximation gave similar dwell times of ChpT and CtrA within the poles: 132±39 ms and 132±28 ms (95% CI), respectively. This was three-fold slower than the rate of exit in simulations of free diffusion, reflecting binding events and slowed diffusion within the crowded PopZ matrix.

The PopZ microdomain creates a barrier to entry for non-client proteins

Ribosomes and chromosomal DNA do not enter the PopZ microdomain, an effect ascribed to such large molecules being unable to pass through the fine pores of a filamentous PopZ matrix (Bowman et al., 2010; Ebersbach et al., 2008). We wondered whether the slowed diffusion and escape rates of ChpT and CtrA within the PopZ microdomain was due in part to percolation through such a matrix. To isolate this effect, we performed single-molecule tracking of proteins heterologous to *Caulobacter*, for which binding interactions to polar localization factors should be

minimal. We selected two proteins: eYFP by itself, and eYFP fused to a 100 amino acid fragment of *A. thaliana* PIF6 which we term fPIF (Levskaya et al., 2009). As eYFP was 0.5 times and fPIF-eYFP was 0.75 times the mass of ChpT-eYFP and CtrA-eYFP-14 (Table S1), as reflected by their faster diffusion in the cell body (Figure S6), we predicted that both proteins would penetrate the PopZ matrix. Yet surprisingly, both eYFP and fPIF-eYFP only explored the 3D volume of the cell up to the edge of PopZ, and did not enter the microdomain (Figure 5H, Figure S6).

We quantified the polar recruitment and exclusion of ChpT, CtrA, fPIF, and eYFP by counting single-molecule localizations that appeared within the super-resolved reconstruction of PopZ, and comparing these patterns to the expected distribution in the absence of microdomain interactions from simulations of free diffusion throughout the cell volume (Figure 5I, Figure S6). Relative to the "free diffusion" case, ChpT and CtrA were concentrated ~3x at the old pole and ~2x at the new pole, reflecting their direct (PopZ-binding) and indirect (ChpT-binding) recruitment. By contrast, fPIF and eYFP were not only not enriched, but were actively excluded from the poles; while a small fraction (4.0 +/- 0.6%) of fPIF molecules were scored as polar, these molecules were generally located at the cytoplasmic interface of the microdomain, not the interior (Figure 5H). As fPIF and eYFP were excluded, despite being smaller than ChpT and CtrA, pore size cannot explain this effect. In contrast to our experiments with wildtype cells, fluorescent proteins are able to enter the PopZ microdomain when PopZ is heterologously expressed in *E. coli* (i.e., in the absence of known clients), or when PopZ is enlarged 10-20 fold to 2-4 μm in Caulobacter, greatly increasing the available volume (Ebersbach et al., 2008; Laloux and Jacobs-Wagner, 2013). This suggests that in addition to the presence or absence of specific binding interactions to PopZ or other polar proteins, general properties such as the volume and client

occupancy of the PopZ microdomain may also control the microdomain permeability in a nonspecific way.

CtrA activation occurs within and modulated by the new pole microdomain

Using our quantitative microscopy measurements of the distributions and dynamics of CckA, ChpT, and CtrA, we comprehensively simulated signaling in the predivisional cell within our reaction-diffusion framework. The simulation included: (i) a calculated effective K_D between the microdomain and CckA, ChpT, and CtrA to match our localization profiles, (ii) the measured diffusion coefficients, and (iii) an adjusted unbinding rate between CckA and the microdomain to match the measured exit rates (Figure S4). In our model, steady state distributions of CckA, ChpT, and CtrA recapitulated localization profiles observed both by diffraction-limited and single-molecule imaging (Figures 1B-D, 5E, S7A). Similarly, steady state profiles of all three proteins revealed the concentration of the phosphorylated state at the new cell pole microdomain (93% of CckA~P, 68% of ChpT~P, and 10% of CtrA~P). ChpT~P concentration sharply dropped from the new pole microdomain and continued to decline with a shallower sublinear gradient (Figure 6A). In contrast, the CtrA~P concentration declined smoothly away from the new pole microdomain with a sublinear distribution (Figure 6A). Following our calculation of transcriptional response from the P_{350} promoter integrated at the four chromosomal loci (Figure 3A,B), we calculated transcriptional output in response to the modeled CtrA~P distribution. The calculated *eyfp* mRNA values recapitulated the measured mRNA levels in our model (Figures 3A, S7A). Collectively, based on the consistency between multiple sets of independent measurements (biochemical rates from the literature, diffusion coefficients from single-molecule tracking, and transcription activity

based on qRT-PCR), we concluded that CtrA~P exhibits a roughly exponential gradient in predivisional cells.

Sequestration of the phosphorylated form of all three proteins to the new pole microdomain suggests that forward phospho-transfer events happen within the microdomain. We used our reaction-diffusion framework to count transfer events as a function of time and cellular position. We observed that more than 95% of forward transfer events (from CckA~P to ChpT and from ChpT~P to CtrA) occur within the new pole microdomain, while back transfer events (from CtrA~P to ChpT and from ChpT~P to CckA) occur everywhere away from the new pole (Figure 6B, Figure S7). Our sensitivity analysis predicted that the binding affinity between ChpT and the new pole microdomain strongly affects the CtrA~P gradient (Figure 3C). Counting phospho-transfer events in an *in-silico* mutant with a weakened binding affinity between ChpT and the microdomain (K_D between ChpT and the microdomain reduced from 10 nM to 10 μM), we observed a drastic change in the spatial distribution of forward phospho-transfer events (Figure 6B). 46% of ChpT~P molecules left the pole before passing the phosphate to CtrA, which led to 60% of ChpT~P to CtrA transfer events occurring outside of the new pole hub. Collectively, phospho-transfer count analysis provides evidence that CtrA is phosphorylated within the new pole microdomain and that binding to the microdomain facilitates this process.

Our single-molecule measurements showing protein exclusion from the pole demonstrate that selective entry into the limited cytosolic polar volume may be controlled not only by the strength of specific binding interactions, but by mechanisms that control global permeability for all potential clients. One potential mechanism is client density: if many clients bind within the microdomain, they may occupy free volume or binding sites and prevent competing proteins from entering. To model such (occupancy-based) universal regulation of microdomain permeability, we

altered the density of cytosolic client proteins inside the PopZ microdomain by introducing a separate cytosolic protein with high binding affinity for the microdomain while keeping the binding affinities of CckA, ChpT and CtrA to the microdomain constant (SI). This perturbation led to competition for limited binding sites within the PopZ microdomain, mimicking the effect of changing the global permeability of the microdomain. The simulated reduction in the microdomain permeability led to a 50% decrease in the relative proportion of ChpT and CtrA inside the poles, driving a dramatic reduction in the effectiveness of CtrA~P signaling (quantified by CtrA~P amplitude and CtrA~P distribution, Figure 6C). These simulations illustrate the critical role microdomain permeability plays in modulating CtrA~P amplitude and shape by regulation of the concentration of members of the activation pathway.

CtrA molecules are cleared from the cell during differentiation and resynthesized in predivisional cells over the course of 60 minutes (Domian et al., 1997; Quon et al., 1996). We used our model to determine how the CtrA~P gradient evolves from newly synthesized CtrA molecules in predivisional cells. We found that for a given number of total CtrA molecules, CtrA is rapidly phosphorylated and that the CtrA~P amplitude reaches steady state within five minutes of simulation time (Figure 6D). The nonlinear gradient in CtrA~P distribution is established immediately at the beginning of the simulation and is maintained until reaching its steady state. Thus, the quasi-steady-state CtrA~P gradient is established early in predivisional cells as CtrA molecules are synthesized, robustly priming the nascent daughter cells for asymmetry.

DISCUSSION

Membrane-enclosed compartments, such as the nucleus (Meldi and Brickner, 2011), mitochondria (Nunnari and Suomalainen, 2012), and chloroplasts (Eberhard et al., 2008) in eukaryotes, and thylakoids (Nevo et al., 2007), magnetosomes (Komeili et al., 2006), and the periplasmic space (Bos et al., 2007) in bacteria, are an effective means for concentrating functional complexes to isolated environments within the cell. Alternatively, membrane-less compartments have emerged as a widespread organizational unit. These include membrane-less organelles in eukaryotes (Alberti, 2017; Banani et al., 2017; Shin and Brangwynne, 2017) such as Cajal bodies (Mao et al., 2011) and germ granules (Voronina et al., 2011), and protein-encapsulated microcompartments in prokaryotes and archaea (Kerfeld and Erbilgin, 2015; Kerfeld et al., 2010) such as carboxysomes (Kerfeld and Melnicki, 2016) and encapsulins (Giessen, 2016). Bacterial cells also employ low complexity multivalent proteins as membrane-less localization platforms to direct cellular development (Ben-Yehuda et al., 2003; Bowman et al., 2008; Ebersbach et al., 2008; Lin et al., 2017; Yoshiharu et al., 2012).

Eukaryotic membraneless compartments are held together by weak interactions between their components that form agglomerated condensates (Molliex et al., 2015; Nott et al., 2015). Unlike structurally defined macromolecular complexes, such as the ribosome or the 26S proteasome, the size and internal organization of such condensates are both heterogeneous and dynamic (Shin and Brangwynne, 2017). Here, we showed that the *Caulobacter* PopZ microdomain, which lacks both a membrane enclosure and a protein shell, differs from bacterial microcompartments while sharing key qualities with eukaryotic condensed compartments. Most significantly for function, the PopZ microdomain size is dynamic, client entry into the microdomain is selective, and clients dynamically exchange with the cytosol. We further showed

that these properties facilitate accelerated phospho-transfer reactions and modulation of the amplitude and distribution of CtrA~P in the predivisional cell.

Organization and selective permeability of the space-filling PopZ microdomain

PopZ self-assembles to organize a space-filling microdomain (Bowman et al., 2013; Gahlmann et al., 2013; Ptacin et al., 2014) that coordinates a suite of cell polarity functions including the phospho-transfer cascade controlling CtrA activity (Berge and Viollier, 2017; Ptacin and Shapiro, 2013). Whereas PopZ itself is cytoplasmic, both transmembrane and cytosolic client proteins are (to our imaging resolution) uniformly distributed adjacent to and throughout the space-filling PopZ microdomain for transmembrane and cytosolic proteins, respectively (Figure 4, Figure 5) (Ptacin et al., 2014). PopZ is recruited to the membrane by direct binding to several membrane-bound factors, and mislocalization of these factors can seed ectopic PopZ microdomains (Berge et al., 2016; Holmes et al., 2016; Perez et al., 2017). Thus, the shape of the PopZ microdomain appears to be defined by a condensation and wetting process that balances cohesive forces (self-interaction) and adhesive forces (membrane-protein interactions), similar to that observed for tau protein droplets on microtubules (Hernandez-Vega et al., 2017). This balance allows PopZ to lie across a substantial membrane surface area while still creating a large but porous space-filling volume, bridging the membrane and the cytoplasm and jointly concentrating both membrane and cytoplasmic proteins.

The PopZ microdomain selectively captures and concentrates target proteins at the cell pole, including the three CtrA pathway proteins. Proteins are recruited to the PopZ microdomain either by direct binding to PopZ, as shown for at least nine client proteins (Berge et al., 2016; Holmes et al., 2016), or indirectly by binding to one or more proteins which bind PopZ, as shown

for the membrane protein DivJ (Perez et al., 2017) and the cytosolic protein CtrA (Figures 1D, 5, and 7). Whereas large molecules and complexes such as DNA and ribosomes (Bowman et al., 2008; Ebersbach et al., 2008) are excluded from the microdomain, we have shown that small proteins lacking a microdomain binding partner, such as free eYFP and fPIF-eYFP, cannot penetrate the PopZ microdomain despite being similar in size and charge to proteins that do enter (Figure 5H, Figure 7, Table S1). Notably, when the PopZ microdomain is drastically expanded by exclusively overexpressing *popZ*, fluorescent proteins, including eYFP, can enter the microdomain (Ebersbach et al., 2008; Laloux and Jacobs-Wagner, 2013), suggesting that changes in the microdomain such as occupancy can regulate its permeability prosperities. Indeed, studies of eukaryotic condensates have identified multiple factors that affect permeability, including occupancy by additional binding partners (Banani et al., 2017), charged proteins (Nott et al., 2016), or RNAs (Wei et al., 2017), as well as environmental properties including viscosity, dielectric constant, and scaffold-scaffold interaction strength within the condensate. Our observation that eYFP and fPIF-eYFP cannot enter the wildtype microdomain interior even transiently (Figure 5H) demonstrate that even without membrane barriers or a protein shell, the PopZ microdomain forms a compartmentalized volume of strictly defined composition.

Efficient phospho-transfer within the PopZ microdomain

Joint sequestration of CckA, ChpT, and CtrA acts to locally enhance pathway activity within the PopZ microdomain (Figures 3, 5, 6C, and 7). We previously reported *in vitro* reconstitution experiments showing that high densities of CckA on liposomes enhance its autokinase activity (Mann et al., 2016). In keeping with these results, CckA functions as a kinase *in vivo* solely when sequestered at the new pole of predivisional cells (Iniesta et al., 2010a; Jacobs et al., 2003; Jacobs

et al., 1999), where the new pole-specific factor DivL is recruited to allosterically modulate CckA kinase activity (Childers et al., 2014; Iniesta et al., 2010a; Tsokos et al., 2011). CckA positioned elsewhere in the cell primarily acts as a phosphatase (Iniesta et al., 2010a; Mann et al., 2016). Indeed, the dependence of CckA autokinase activity on concentration implies that the ~500-1,000x higher CckA density achieved within the new pole is necessary for CckA to act as a phosphate source (SI) (Mann et al., 2016). Further, the elevated concentrations of all three proteins increase the probability of intermolecular binding and phosphate transfer events between CckA and ChpT, and ChpT and CtrA via mass action (Figure 3D), and the vast majority of phospho-transfer events take place within the microdomain (Figure 6B). Similarly, a model for the function of the chromosome partitioning protein ParA (Ptacin et al., 2014) suggests that high ParA concentration and thus an increased rate of homodimerization within the PopZ microdomain is critical for chromosome segregation. More broadly, membrane-less compartments are emerging as an important mechanism for creating specialized condensed signaling environments (Chong and Forman-Kay, 2016; Li et al., 2012; Su et al., 2016). This function is reminiscent of scaffolding molecules that bind multiple signaling proteins simultaneously to regulate selectivity and adaptation to stress (Atay and Skotheim, 2017; Good et al., 2011). Quantitative characterization of the unique properties of each architecture would provide insight into the advantages of using either subcellular organization strategy.

Our results show that in addition to concentrating proteins, the intrinsic character of the PopZ microdomain slows turnover between the pole and the cell body. The observed rates of ChpT and CtrA exit from the pole, on the order of 100 ms (Figure 5), are several times slower than would be expected without sequestration within the microdomain. This slow turnover results from a combination of binding to PopZ and other polar proteins (as implied by localization to the pole),

and to percolation through the microdomain volume (reflected by the slow, anomalous polar diffusion of CtrA, Figures 5D, 5F, and 7). Similarly, while CckA still diffuses freely (though more slowly) at the polar membrane, binding interactions slow the exchange of CckA between the polar microdomain and the rest of the cell (Figure 4D). Tracking experiments with gold nanobead labels in mammalian cells have shown that physical obstruction by cortical actin networks causes transmembrane proteins to exhibit "hop diffusion" between nanoscale domains on the sub-ms timescale (Fujiwara et al., 2016). While such phenomena are below the resolution of our experiments, obstruction by PopZ polymers close to the membrane may slow CckA motion at the poles.

A sequestered phospho-signaling cascade drives a gradient of active CtrA

Sensitivity analysis in our reaction-diffusion model showed that sequestration of all three proteins within the new pole microdomain is critical for establishing a CtrA~P gradient (Figure 3C). Both ChpT and CtrA must be localized at high density for rapid phospho-transfer within the pole, while allowing ChpT to transfer its phosphate to CtrA outside of the microdomain would reduce or eliminate the gradient (Figure 3E and 6). Critically, we found replacing *ctrA* with its phosphomimetic mutant *ctrA*(*D51E*), which is active independent of the polar signaling cascade, abolished the gradient of transcriptional activity and disrupts normal cell cycle progression (Figure 2B).

Spatial separation of opposing enzymes in activation–deactivation cycles of protein modification is necessary for maintaining a protein activity gradient (Brown and Kholodenko, 1999). Because the phospho-transfer cascade that activates CtrA is conducted via the intermediate cytosolic protein ChpT, the requirements for maintaining a steady state gradient of CtrA~P are

more complex than a canonical gradient established by two factors. In systems with one phospho-transfer step, in which the phosphatase is far from saturating, the gradient decays almost exponentially as a function of the ratio between diffusion of signal and phosphatase rate (Barkai and Shilo, 2009; Tropini et al., 2012; Wartlick et al., 2009). Examples include GTPase RAN (Kalab et al., 2002), the yeast mAPK Fus3 (Maeder et al., 2007), and the yeast protein kinase Pom1 (Moseley et al., 2009). In systems with a cascade of phospho-transfer steps, co-localization of the pathway components plays a key role in gradient shape (Kholodenko et al., 2010). Scaffolding proteins have been shown to modulate signal processing and propagation by recruitment of multiple components to a restricted space and the induction of allosteric effects. Examples include β-arrestin that coordinates multiple pathways downstream of G-proteins coupled receptors (DeWire et al., 2007) and Ste5 that functions in the yeast mating MAPK pathway (Atay and Skotheim, 2017; Bhattacharyya et al., 2006; Good et al., 2009). Here we demonstrated that a bacterial microdomain exhibits a similar function to eukaryotic scaffolds by sequestering all members of the CtrA activation pathway and effectively combining the forward phospho-transfer activities of CckA and ChpT into one localized enhanced source, generating a gradient of CtrA~P across the entire cell (Figure 6 and Figure 7).

A stable CtrA~P gradient facilitates asymmetric division

Caulobacter asymmetric cell division yields daughter cells that exhibits different genetic readouts despite having identical genomes (McAdams and Shapiro, 2009). Differences in gene expression profiles stem from the asymmetric inheritance of the CtrA~P transcription factor controlling the expression of over 100 cycle-regulated genes, many of which encode swarmer cell-specific functions (Laub et al., 2002; Laub et al., 2000). We showed that the CtrA~P distribution is not

only skewed toward the new pole but decreases rapidly away from the new pole forming a stable sublinear CtrA~P gradient (Figure 2, Figure 6A). In our simulations, the CtrA~P gradient is formed rapidly and maintains its shape, showing that this output is reached quickly and reliably (Figure 6D). We demonstrated using RT-qPCR that timing of the CtrA-regulated gene expression can be modulated by altering the position of the gene on the chromosome (Figure 2A). These results suggest that the induced asymmetry in CtrA~P concentration before division may be used by the cell as regulator of gene expression timing. Indeed, the relative positions of CtrA regulated genes is conserved across alpha-proteobacteria (Ash et al., 2014) and movement of the *ctrA* transcriptional unit from the vicinity of the origin to the vicinity of the termini disrupts normal cell cycle progression (Reisenauer and Shapiro, 2002).

The skewed inheritance of CtrA~P, primed by the gradient, is critical for the differential ability of the two daughter cells to initiate chromosome replication. The daughter stalked cell, in which inherited CtrA~P levels are low, initiates a new round of DNA replication immediately after cytokinesis, whereas the daughter swarmer cell, with high levels of CtrA~P, is arrested in G1 phase until it differentiates into a stalked cell (Quon et al., 1996; Quon et al., 1998). In its phosphorylated form, CtrA~P inhibits initiation of DNA replication by binding to specific sites in the origin region (Quon et al., 1998). Indeed, it was previously suggested that CtrA~P is skewed towards the new cell pole based on the observation that additional replication events happened more often at the stalked cell pole when normal cytokinesis and cell cycle progression was disrupted (Chen et al., 2011). Maintaining a sharp gradient of CtrA~P concentration in the predivisional cell therefore facilitates the robustness of asymmetric division by controlling both differential gene expression and replication initiation.

Outlook

It was recently shown that signaling proteins in eukaryotic cells can not only spontaneously separate into liquid-like agglomerated condensates with distinct physical and biochemical properties, but that these condensates can selectively exclude proteins with antagonist function (Su et al., 2016). Our work highlights how selective sequestration of a signaling pathway within a bacterial membrane-less microdomain provides an environment for accelerated biochemistry that directs signaling across the entire cell with exquisite spatial control culminating in differential activity of a key transcription factor that controls an asymmetric division. Although we do not know the physical nature of the microdomain, nor whether the microdomain separates into a liquid- or gel-like phase, its major constituent, PopZ, is a low complexity protein that forms a mesh-like structure *in vitro,* and self assembles into a distinct cytoplasmic microdomain *in vivo*. The selective permeability of the PopZ microdomain is reminiscent of the eukaryotic nuclear pore complex (NPC), which mediates active transport between nucleus and cytoplasm (Knockenhauer and Schwartz, 2016). The NPC gains a remarkable sorting selectivity from disordered domains that come together in a meshwork and selectively bind to pockets in the proteins that are marked for transport, suggesting a possible functional parallel to the organization and function of the PopZ microdomain (Fu et al., 2017) . Notably, similarities have been drawn between the NPC low complexity domains and P granules, a well-studied membrane-less organelle (Schmidt and Gorlich, 2016). Thus, further structural and functional characterizations of the bacterial PopZ microdomain will be pivotal for revealing fundamental principles for subcellular organization on the mesoscale.

ACKNOWLEDGMENTS

We thank Justin W. Kern for help with plasmid design and construction, Michael D. Melfi for providing a RT-qPCR protocol, Alberto Lovell and Michael R. Eckart at Stanford PAN Facility for their support in conducting RT-qPCR, Jared M. Schrader for sharing unpublished data on mRNA half-life in *Caulobacter*, Andrew Olson at the Stanford Neuroscience Microscopy Service for assistance with photobleaching experiments, as well as Allison Squires for critical feedback on the manuscript. We also thank Harley H. McAdams for helpful discussions on modeling of signal transduction, Darshankumar Pathak and all members of the Shapiro and Moerner labs for helpful discussions throughout the project. We acknowledge support from the Gordon and Betty Moore Function GBMF 2550.03 to Life Sciences Research Foundation [to K.L.], the Weizmann Institute of Science National Postdoctoral Award Program for Advancing Women in Science [to K.L.], and from NIGMS of the National Institutes of Health under award numbers T32GM007276 [to T.H.M], R01-GM086196 [to W.E.M. and L.S.], R35-GM118067 [to W.E.M.], and R35-GM118071 [to L.S.]. L.S. is a Chan Zuckerberg Biohub Investigator.

The content is solely the responsibility of the authors and does not necessarily represent the official views of the National Institutes of Health.

FIGURES

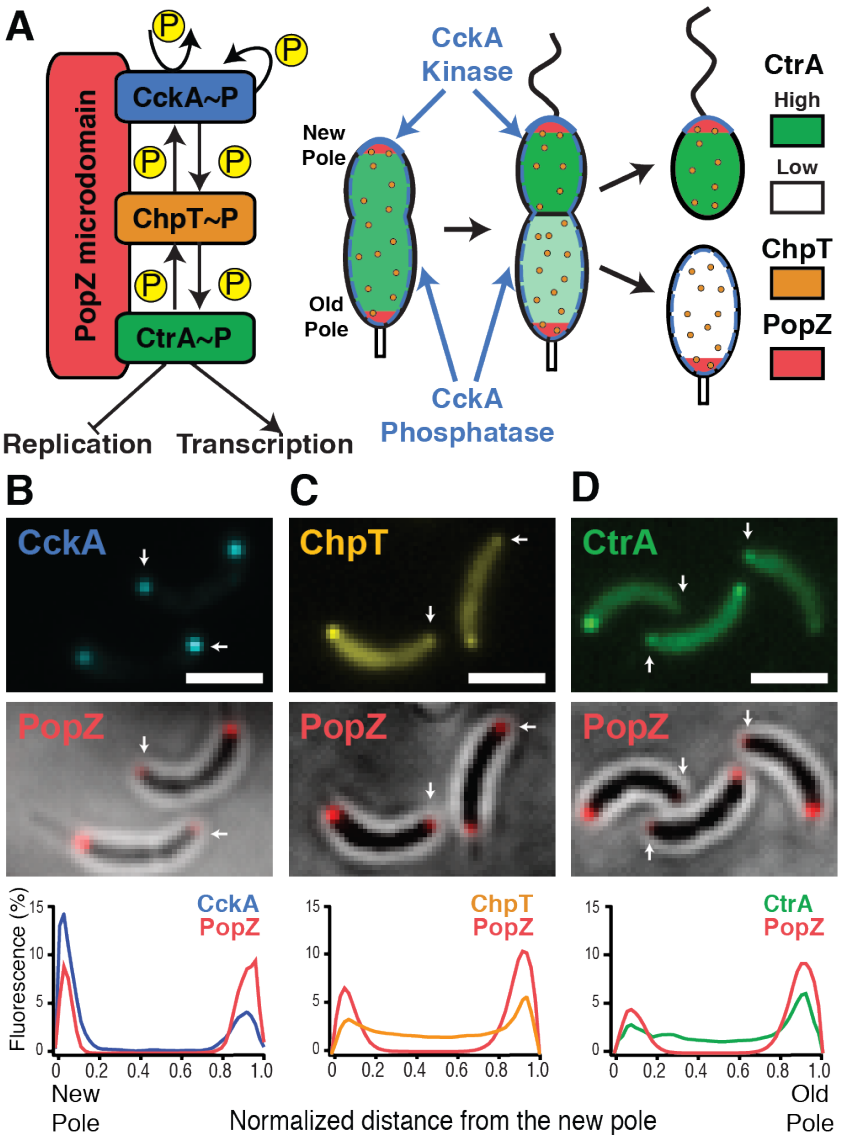

Figure 1. A phospho-signaling cascade sequestered within the PopZ microdomain at the new cell pole culminates in the activation of the cell fate transcription factor CtrA.

(A) The spatially sequestered phospho-signaling cascade. (Left) The hybrid histidine kinase CckA (blue) autophosphorylates upon localization at the new cell pole (Iniesta et al., 2010a; Jacobs et al., 2003; Jonas et al., 2011; Mann et al., 2016; Tsokos et al., 2011) and subsequently transfers

phosphate through the phospho-transfer protein ChpT (orange) to the master transcription factor CtrA (green) (Biondi et al., 2006). Phosphorylated CtrA (CtrA~P) directly controls the transcription of more than 100 cell cycle regulated genes and inhibits the initiation of DNA replication (Laub et al., 2000; Quon et al., 1996; Zhou et al., 2015) . Both CckA and ChpT weakly bind to the disordered PopZ protein (Holmes et al., 2016) that self assembles in a space-filling polar hub (Gahlmann et al., 2013) (red). (Right) In the predivisional cell, CckA is positioned at both the new and old cell poles. CckA acts as a kinase exclusively at the new pole to activate CtrA and as a phosphatase away from the new pole (Mann et al., 2016). Upon compartmentalization prior to division, CtrA is degraded in the stalked compartment and remains phosphorylated (and active) in the incipient swarmer compartment (Domian et al., 1997), yielding distinct transcriptional profiles for the two daughter cells. **(B-D)** Diffraction limited images of *Caulobacter* expressing CckA-eYFP (B), ChpT-eYFP (C), or CtrA-eYFP-14 (D) (top row), with accompanying PAmCherry-PopZ images (middle row), new poles marked with white arrow. The fluorescent intensities of PAmCherry-PopZ and each eYFP-labeled protein are plotted versus normalized cell length for a typical cell (bottom row). CckA, ChpT, and CtrA fluorescence intensity profiles were averaged based on 55, 129, and 143 predivisional cells, respectively. Scale bar for B-D is 2 μm.

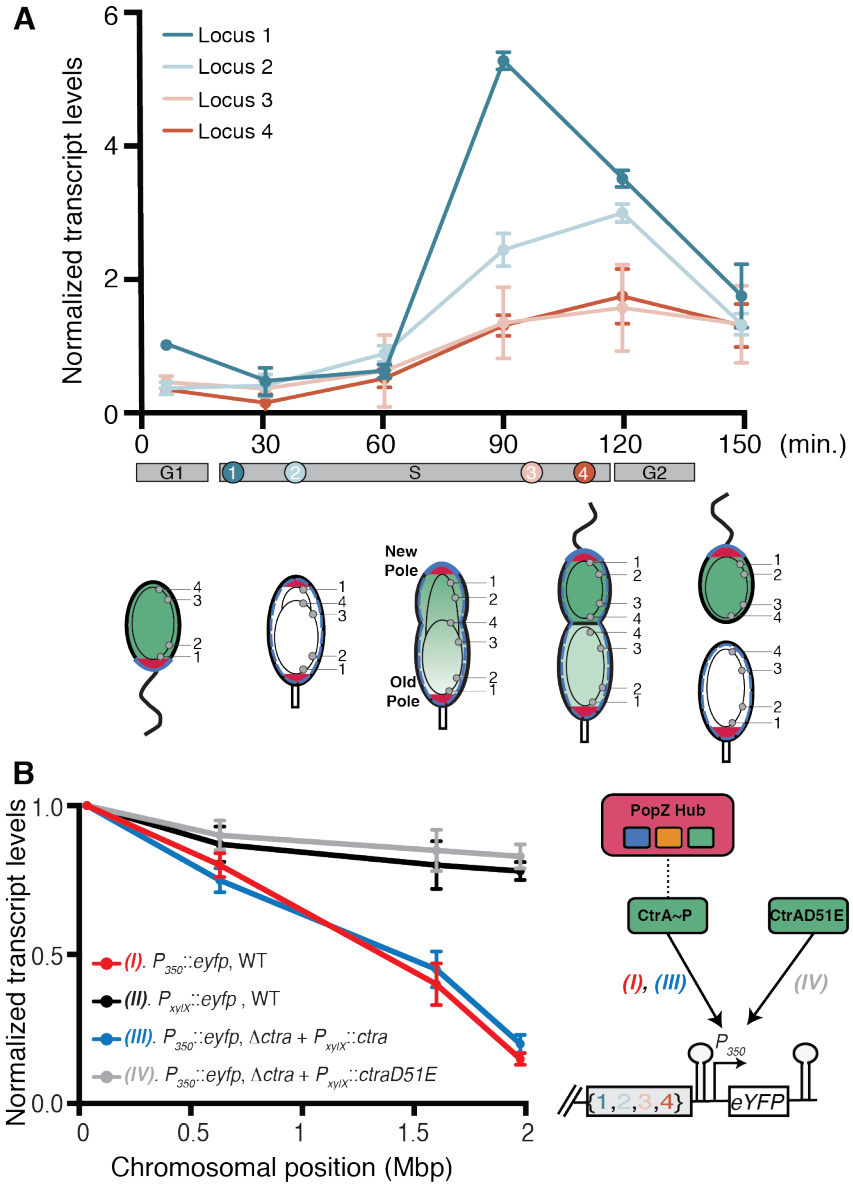

Figure 2. Predivisional cells exhibit a spatial gradient of CtrA~P activity.

(A) Time resolved RT-qPCR of mRNA from an *eyfp* gene under the control of the CtrA-regulated P_{350} promoter integrated at four loci of the chromosome (L1-L4). Transcript levels were assayed every 30 minutes during the 150-minutes cell cycle. A cell cycle schematic illustrating the four chromosomal loci and the progression of DNA replication and segregation. Replication times of loci L1-L4 are shown below the qPCR time points. The chromosome is represented by black ovals

and theta structures within each cell. The red areas of the cell poles indicate the PopZ microdomain and the green tone indicates CtrA~P levels. Transcription is normalized to the five-minutes time point of site 1. Transcription from locus L1 peaked at the 90 minute time point and reached an activity level of 6 AU while transcription from loci L2-L4 peaked at the 120 minutes time point, reaching values of 3, 1.9, and 1.8 AU respectively. **(B)** RT-qPCR of mRNA from an *eyfp* gene integrated at four loci of the chromosome measured in mixed population cells in four different strain backgrounds. Transcription of *eyfp* was driven by either the xylose-inducible P_{xyl} (black), or by the CtrA~P activated promoter, P_{350}. WT CtrA was produced from its native locus (red), or on a plasmid in cells lacking chromosomal *ctrA* (blue). The phospho-mimetic *ctrA*(*D51E*) was produced from a plasmid in a background also lacking native *ctrA* (gray). On the right, a diagram shows the signal pathway for the CtrA~P-controlled promoters and for the phospho-mimetic CtrA(D51E)-controlled promoters that are independent of the signaling cascade. Error bars for A and B represent the standard deviation of three independent experiments.

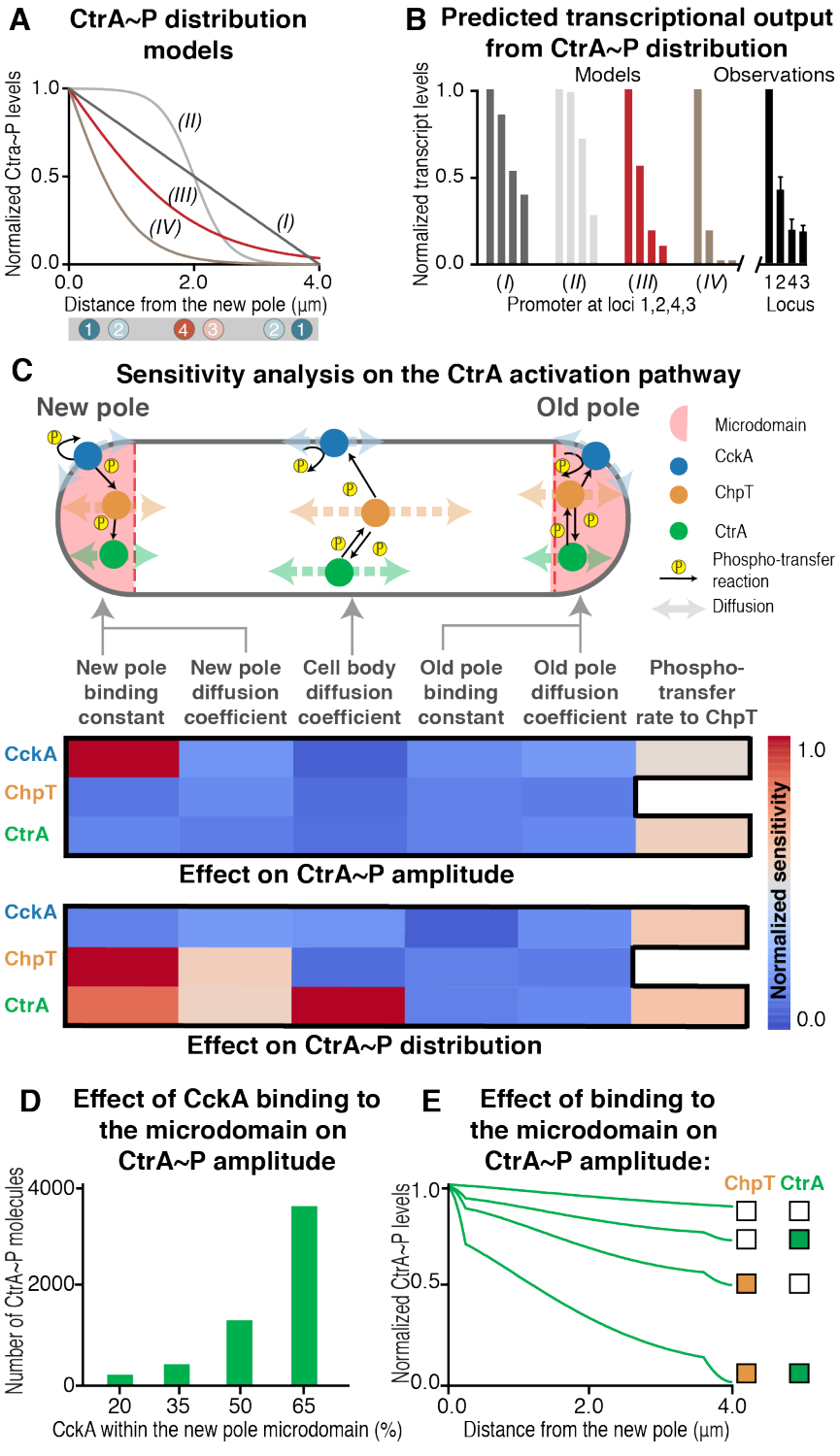

Figure 3. Accumulation of phospho-relay components in the PopZ microdomain governs CtrA~P levels and spatial distribution.

(A) Four possible profiles of CtrA~P distribution along the long axis of the predivisional cell. Note that CckA acts as a kinase specifically at the new pole microdomain. The positions of loci L1-L4 in the predivisional cell are shown in colors along a gray bar. **(B)** Calculated transcript levels of *eyfp* gene driven by the P_{350} CtrA-regulated promoter integrated at chromosomal loci L1-L4 for each of the models (I-IV). Despite the cooperative activity of CtrA~P at P_{350}, neither linear (i, dark gray) no sigmoidal (ii, light gray) CtrA~P profiles recapitulated the measured mRNA production. By contrast, an appropriately steep sublinear distribution (iii, red) recapitulated the transcriptional output obtained experimentally for RT-qPCR of predivisional cells (black, Figure 2A). **(C)** Global analysis of the effect of diffusion coefficients and reaction rates on CtrA~P amplitude and distribution. Sensitivity of CtrA~P amplitude (upper heat map) and CtrA~P distribution (lower heat map) to changes in (i) the rate of CckA, ChpT, and CtrA binding to either the new pole or old pole microdomains, (ii) diffusion coefficients of either CckA, ChpT, or CtrA, and (iii) phospho-transfer rates. Each heat map rectangle specifies one parameter (*e.g.* top/left rectangle specifies sensitivity to changes in the binding rate between CckA and the new pole microdomain). The color of the rectangle indicates the normalized sensitivity value (from low sensitivity (blue) to high sensitivity (red)) to changes in parameter value. An illustration of the examined parameters within the topology of the cell is shown in the diagram above the heat maps. The two microdomains at the new and old pole are shown in pink. CckA (blue) kinase activity is restricted to the new pole while CckA phosphatase activity is around the cell body and the old pole. Phospho-transfer (black arrows) between CckA and ChpT and between ChpT and CtrA can occur everywhere across the cell. Diffusion of CckA (light blue), ChpT (light orange), and CtrA (light green) is shown. **(D)**

Steady-state levels of CtrA~P as a function of CckA accumulation at the new pole microdomain. **(E)** CtrA~P distribution as a function of new pole accumulation of ChpT and CtrA. Steady-state distribution of CtrA~P in four conditions altering the polar accumulation of ChpT and CtrA. In these four conditions ChpT and CtrA are either uniformly distributed (empty boxes) or have 40% total protein accumulated at the two poles (filled boxes).

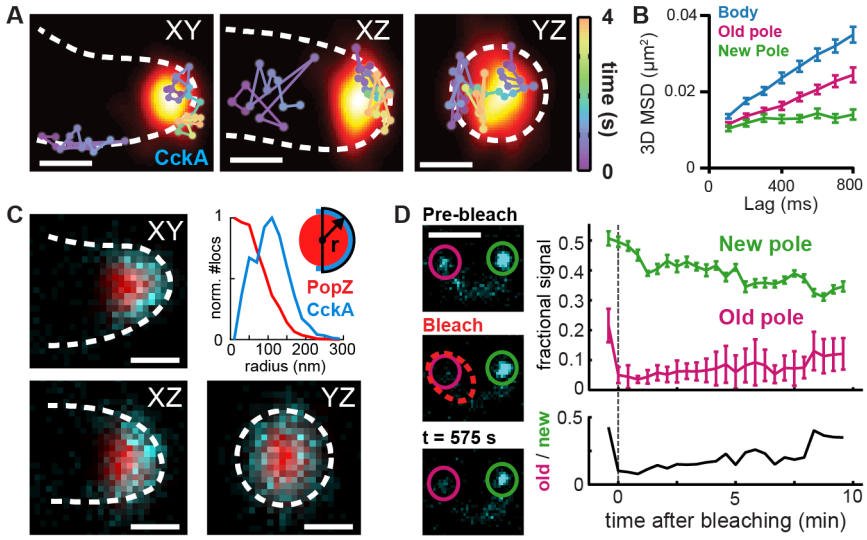

Figure 4. CckA dynamics and distribution within the poles.

(A) 3D single-molecule tracking of CckA (time-coded connected dots) relative to a super-resolution reconstruction of PopZ (yellow-orange). Two example tracks are shown in three different orientations. **(B)** Mean-squared-displacement curves for CckA tracks within selected cellular regions. Errorbars: 95% CI from bootstrap analysis of tracks. **(C)** Average CckA and PopZ polar distributions using 3D localization data from N = 29 old poles (2006 and 5282 localizations respectively). To emphasize the radial distribution of CckA on the membrane, each view shows a 200 nm thick slice (perpendicular to the page). Plot shows the radial distribution of CckA and PopZ from the PopZ centroid with volume-normalized density. **(D)** Loss/recovery from the new and old poles following targeted photobleaching of old pole CckA-eYFP. Signal is defined as the fraction of total cell fluorescence (upper plot, errorbars show ± 95% CI). After 10 minutes, while the total amount of fluorescent CckA-eYFP has been reduced by targeted photobleaching, the initial ratio of old to new pole signal is restored (lower plot). Average of N = 6 cells. Scale bar in **(D)**, 2 μm; all other scale bars, 200 nm.

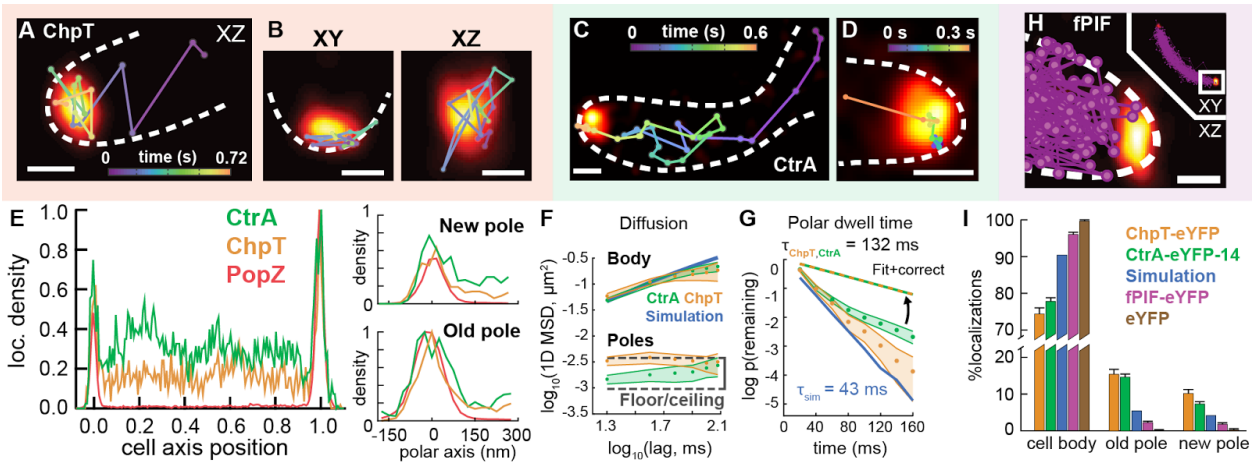

Figure 5. The polar microdomain concentrates and slows ChpT and CtrA, while excluding other small cytoplasmic proteins.

(A-B) Two cells showing representative single-molecule trajectories of ChpT-eYFP (time-coded connected dots) with PAmCherry-PopZ super-resolution reconstructions (yellow-orange). **(A)** ChpT entry into the pole and capture by the PopZ microdomain. This example shows the old pole. **(B)** Two views of the same ChpT molecule as it exhibits apparent membrane-associated motion within the PopZ microdomain at the new pole. **(C-D)** Two cells showing 2D single-molecule trajectories of CtrA-eYFP-14 relative to PAmCherry-PopZ. **(C)** CtrA entering the PopZ microdomain at the new pole. **(D)** CtrA transiting through and leaving the old pole microdomain. **(E)** Average distributions of CtrA (N = 60 cells), ChpT (N = 27), and PopZ (N = 27), along the cell axis and in the local coordinate system of the cell poles. **(F)** Log-log MSD plots of CtrA (green) and ChpT (orange) motion projected along the *Caulobacter* cell axis in both the body and poles. Shaded area: 95% CI from bootstrap analysis of tracks. Blue line: MSD for simulated free diffusion with D = 1.8 $\mu m^2/s$ (Figure S6). Floor/ceiling: the minimum and maximum MSD values within the pole, corresponding to static molecules and molecules that explore the pole within a frame. **(G)** The decay rates of ChpT and CtrA escaping from the pole or bleaching before escape.

Shaded area: 95% CI from bootstrap analysis of tracks. Linearity of the cumulative distribution function of survival, p(remaining), on the semi-log plot indicates an exponential distribution (Distributions from N = 434 and 1149 events of which 77.1% and 80.9% were due to bleaching, respectively.) Blue line: distribution of escape rates from the pole for simulated molecules diffusing with D = 1.8 $\mu m^2/s$ without hindrance by PopZ (Figure S6). Exponential fit lifetimes (1/e) shown. **(H)** Representative cell displaying an overlay of 92 total 3D single- molecule tracks of fPIF-eYFP shown relative to a PAmCherry-PopZ super-resolution reconstruction. **(I)** The proportion of localizations within the cell body, the new pole, and the old pole, as observed for tracks of ChpT-eYFP, CtrA-eYFP-14, fPIF-eYFP, and eYFP, and for simulated diffusing molecules unconstrained by PopZ (Figure S6). Magnitude of 95% CI shown as lines above data. Scale bars: 200 nm.

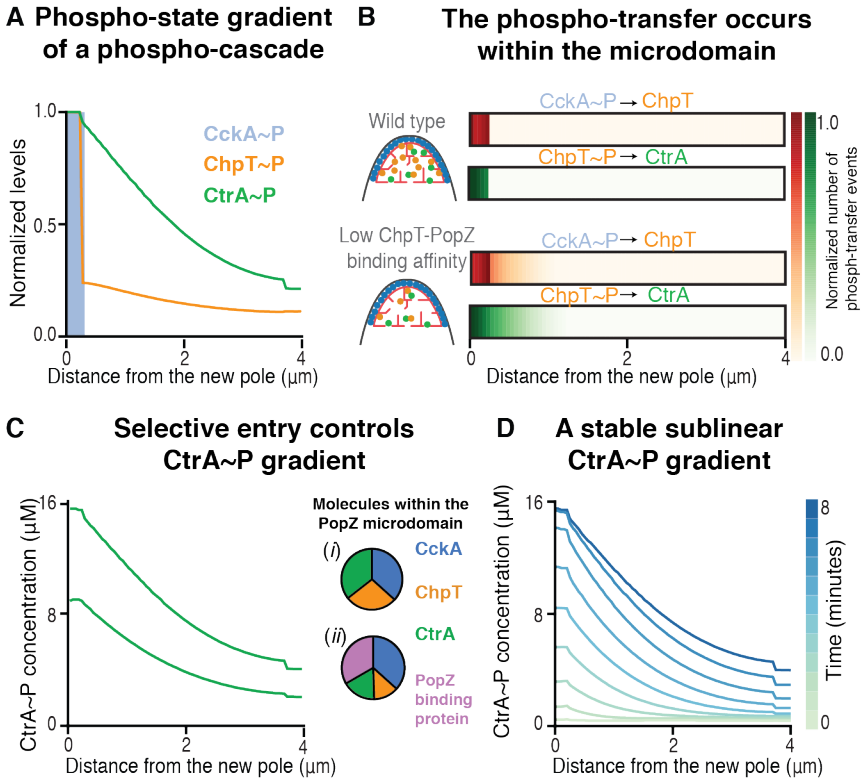

Figure 6. PopZ microdomain modulates CtrA activity gradient.

(A) The predivisional cell maintains a gradient of ChpT~P and CtrA~P. Steady state distributions of CckA~P, ChpT~P, and CtrA~P (light blue, orange, and green) as derived from our reaction-diffusion model incorporating measured diffusion coefficients (Figures 4 and 5). The phosphorylated forms of all three proteins are localized to the new pole microdomain, where CckA acts as a kinase. Both ChpT~P and CtrA~P exhibit a gradient descending from the new pole. CtrA~P forms a steep sublinear gradient, such that most CtrA~P molecules reside in the nascent daughter swarmer cell compartment. Phospho-transfer from ChpT~P to form CtrA~P occurs rapidly within the pole, depleting most ChpT~P molecules before exit and causing the relative levels of ChpT~P in the body to be much lower than those of CtrA~P, although still maintaining

a shallow gradient. In comparison to the phospho-gradients of ChpT and CtrA, the total populations of ChpT/ChpT~P and CtrA/CtrA~P within the cell body were evenly distributed (Figure S7A). **(B)** Phospho-transfer events occur at the new pole microdomain. "Phospho-graphs" showing the number of CckA~P to ChpT and ChpT~P to CtrA phospho-transfer events at steady state. The phospho-transfer events occur exclusively within the new pole microdomain in a simulation using our measured parameters (upper phospho-graph). However, in an *in-silico* mutant with weak binding between ChpT and the PopZ microdomain, phospho-transfer events are dispersed across the cell (lower phospho-graph). **(C)** Introduction of a competitor for PopZ binding sites in the new pole microdomain decreases the polar concentration of signaling proteins and diminishes the CtrA~P gradient. Steady-state distributions of CtrA~P concentration along the long axis of the cell is shown in wildtype conditions (*i*) and with the addition of a new protein (purple) that competes for PopZ binding sites in the new pole microdomain (*ii*). The pie charts (right) show the relative occupancy of PopZ binding sites by CckA, ChpT, CtrA, and the competitive binder (blue, orange, green, purple). With the addition of the competitive binder the number of ChpT and CtrA molecules within the microdomain is reduced ((*ii*), pie chart). Under this condition, the total amount of CtrA~P molecules is reduced by 42% and the gradient shape becomes less steep. **(D)** The predivisional cell maintains a sublinear CtrA~P gradient. Starting with 10,000 unphosphorylated CtrA molecules, within the course of 8 minutes of simulation, 63% of CtrA molecules are phosphorylated and a gradient of CtrA~P is established. CtrA~P maintains a similar sublinear distribution over time, as shown at 10 equally spaced time intervals (light green to blue lines). In each interval at least 70% of all CtrA~P molecules are found in newly formed daughter swarmer cell (at most 2 μm away from the new pole).

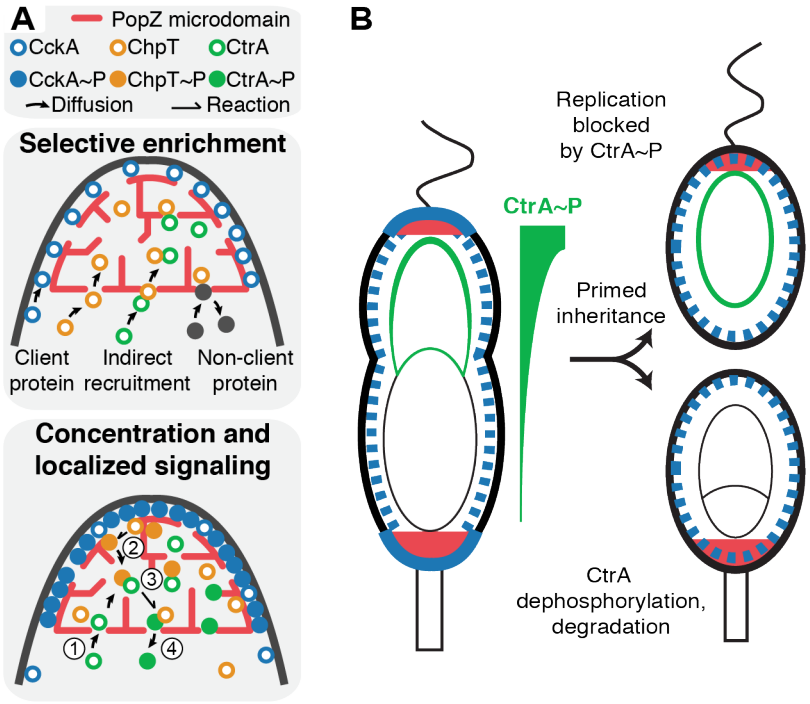

Figure 7. A transcriptional gradient propagates from the PopZ microdomain at the new pole, in which cell fate signaling flow is altered.

(A) Specialized properties of the new pole PopZ microdomain establish a local zone of differential signaling flow. Selective entry of client proteins is permitted via direct interaction with PopZ or by interaction with a PopZ client (indirect recruitment), whereas non-client proteins cannot enter. Proteins localized to PopZ are concentrated in the microdomain due to extended dwell times relative to the cell body. Increased concentration of CckA-ChpT-CtrA pathway components leads to a local increase in CckA kinase activity and thus CtrA~P output. The numbers represent stages of the phospho-transfer pathway; 1) recruitment of proteins to the microdomain, 2) complex formation and transfer of phosphate from CckA~P to ChpT, 3) complex formation and transfer of phosphate from ChpT~P to CtrA, and 4) exit of CtrA~P from the microdomain, establishing a local source of CtrA~P. **(B)** CckA acts as a kinase while accumulated at the new cell pole (blue wedge) while its phosphatase activity dominates when it is diffusely localized (blue dashes) in the

rest of the cell. This localized source of kinase signaling flow, in conjunction with slowed CtrA~P diffusion across the long axis of the cell, ultimately leads to a phospho-gradient that primes each daughter cell for a distinct cell fate. High CtrA~P blocks DNA replication in the swarmer progeny, whereas CckA phosphatase activity in the stalked progeny leads to dephosphorylation and ultimately degradation of CtrA, permitting DNA replication and differential readout of the chromosome in the two progeny cells. The theta structure represents the partially replicated chromosome in the predivisional cell and stalked progeny, while the swarmer cell has a single circular chromosome. Green shading along the chromosome represents binding by CtrA~P to the origin, which forms a gradient in predivisional cells, is uniform in swarmer progeny, and is absent in stalked progeny.

SUPPLEMENTARY INFORMATION

Plasmid construction

All vectors were constructed by Gibson assembly (Gibson et al., 2009). Table S2 provides a description of all plasmids used in the study.

pKL400-pKL403: The template vector pXVENN-2 (Thanbichler et al., 2007) was amplified using primers GGGCGGGGATGAACTGACAAATAAAACGAAAGGCTCAGTC-GA and GCCCGAACTTCATGGTCCCACGTCCTCAAGA. The 1000 base-pair regions used to integrate P_{XylX}::*eyfp* at loci L1-L4 were amplified with primers as indicated in Table S4.

pKL410, pKL433, pKL415, and pKL416: Vectors pKL400-pKL403 were each amplified using primers GGGTGGGGACGAGATGGTGAGCAAGGGCGAGGAGC and CGGTTTCGC-GGCAGAAGCTCAAGCTTATATAAAAACTGTTGTAATTCATTAAGC. The P_{350} promoter region (coordinates 365185 to 365305) was amplified from the *Caulobacter* genome using primers CAACAGTTTTTATATAAGCTTGAGCTTCTGCCGCGAAACCG and CCTTGCTCACCAT-CTCGTCCCCACCCGCTTCAG.

pKL412, pKL420-pKL422: Vectors pKL400-pKL403 were each amplified using primers AGGAGACCAAGTCATGGTGAGCAAGGGCGAGGAGC and TCGCTGCCAAGCCGTCC-CTTATTCGCACCTGGCGG. The P_{pilA} promoter region (coordinates 3198523 to 3198523) was amplified from the *Caulobacter* genome using primers GCGAATAAGGGACGGCT-TGGCAGCGATCGCG and CCCTTGCTCACCATGACTTGGTCTCCTAAACCAGAGC.

chpT-eYFP: pYFPC-1 was amplified with primers CTGGGTCCCGGCGGGTACCTTA-AGATCTCGAGCTCCG and GTGGTCTCGGTGACAATTAAGGCGCCTGCAGG. ChpT was

amplified from the *Caulobacter* genome using primers AGGCGCCTTAATTGTCACCGAGAC-CACCGCCCC and ATCTTAAGGTACCCGCCGGGACCCAGGCGGC.

PIF-eYFP: pVYFPN-1 was amplified with primers GCAATAAACATGTTGACTAAGG-TACCTTAAGATCTCGAGCTCCGG and CGGTTGGTAAGAACATCATATGCATATTAAT-TAAGGCGCCTGCAGG. PIF was amplified from pHR-YFP-PIF-SOScat plasmid (Addgene plasmid #50851) using primers GGCGCCTTAATTAATATGCATATGATGTTCTTACCAAC-CGATTATTGTTGC and GCTCTAAGGGTACCTTAGTCAACATGTTTATTGCTTTCCAAC-ATG.

Strains, Cell growth, and synchrony

All *Caulobacter* strains used in this study were derived from the synchronizable wild-type strain CB15N (Poindexter, 1964). *Caulobacter* cells were grown in PYE (peptone-yeast extract) media (Poindexter, 1964), M2 minimal medium (Ely, 1991), or in minimal media supplemented with 0.2% D-glucose (M2G). Cells were grown in M2G media in log phase for at least 12 hours before synchronizing the cultures (Tsai and Alley, 2001). When appropriate, growth media was supplemented with the following antibiotics: 0.5 μg/mL gentamicin, 5 μg/mL kanamycin, 1 μg/mL oxytetracycline, 25 μg/mL spectinomycin, and/or 1 μg/mL chloramphenicol. Expression of specific genes was induced by addition of vanillate (pH 7.5) or D-xylose at the indicated concentrations and for the indicated time periods before imaging. Generalized transduction was performed with phage *ϕCr30* as described (Ely, 1991). Strains were imaged at mid-exponential growth phase (OD_{600} = 0.3-0.5). Description of all strains used in this study is in Table S3.

Localization profile analysis

Image analysis code was written in Matlab Version 9.2 with the Control System, Curve Fitting, Image Processing, Optimization, Signal Processing and Statistics toolboxes. Cell outlines were identified from the binary image of intensity-thresholded brightfield images. Cells were selected for further analysis with length and width filters, preventing analysis of *e.g.* overlapping cells. Fluorescent images were registered to their corresponding brightfield images by cross-correlation. A local cellular coordinate system was determined for each cell by first fitting a spline to the cell outline, then defining the cell axis as the midpoint of this outline. The poles of the cells were defined as the points of the cell outline with maximum curvature. Cells were orientated from new pole to old pole based on PopZ focus size, with larger focus assigned to the old pole. Fluorescent profile for each cell was calculated as total signal within segments along the local cellular coordinate system following background substation.

Approximate gene position along the long axis of the cell

We used previously published data on the spatial organization of the *Caulobacter* genome and the rate of chromosome duplication to estimate gene positions over the course of the cell cycle (Viollier et al., 2004).

The length of the cell, defined as the pole-to-pole distance along the contour of the cell medial axis, increases exponentially in rich media with a time constant of 125±8 minutes, starting at 1.6±0.2 μm for swarmer cells and reaching 4.3±0.3 μm prior to division (Iyer-Biswas et al., 2014; Wright et al., 2015) (Equation S1).

$$l(t) = l_0 + \alpha e^{\beta t} \quad (S1)$$

, where l(t) is the length of the cell as a function of the cell cycle time ($0 \leq t \leq 140$ min), l_0 is the swarmer cell length at the beginning of the cell cycle ($l_0 = 1.6$), $\alpha = 0.85$ and $\beta = 0.0078$ min^{-1}.

Caulobacter possesses a single circular chromosome. DNA replication initiates at a unique origin of replication (*Cori*) and proceeds bidirectionally (Brassinga and Marczynski, 2001; Dingwall and Shapiro, 1989). In the swarmer cell and in the stalked cell before chromosome replication, *Cori* is positioned near the old cell pole, where it is physically tethered to the PopZ microdomain *via* the ParB protein (Bowman et al., 2008; Ebersbach et al., 2008; Ptacin et al., 2014) (Figure 2A). Loci along the circular chromosome occupy well-defined and reproducible spatial coordinates, with position along the cell axis proportional to their distance from *Cori* on the chromosome (Le et al., 2013; Umbarger et al., 2011; Viollier et al., 2004). The rate of chromosome duplication by the replisome is constant over the 90 minutes total replication time (Kozdon et al., 2013). The newly replicated DNA segments are immediately and rapidly directed to their final subcellular positions following replication (Viollier et al., 2004) (Figure 2A). We used Equations S2 and S3 to approximate the spatial position of each chromosomal locus (*bp*) on the original chromosome, ($P_{orig}(bp)$), and its newly replicated copy ($P_{replicated}(bp,t)$) during DNA replication (minutes 20 to 110 in the cell cycle), along the cell axis relative to the old pole. Because the spatial organization of the old chromosome does not change, $P_{orig}(bp)$ is independent of time,

$$P_{orig}(bp) = l_{pole} + \left(l(0) - l_{pole}\right) * \begin{cases} \dfrac{bp}{M} & bp \leq M \\ 1 - \dfrac{bp - M}{M} & bp > M \end{cases} \qquad (S2)$$

, where l_{pole} is the diameter of the old pole microdomain, from which the chromosome is excluded, and M is the base-pair coordinate of the terminus region, which is positioned approximately halfway along the circular chromosome.

By contrast, the positions of loci on the new chromosome are defined by the time-dependent position of the new pole,

$$P_{replicated}(bp,t) = \begin{cases} l(0) + (l(t) - l_{pole} - l(0)) * \begin{cases} 1 - \frac{bp}{M}, & bp \le M \\ \frac{bp - M}{M}, & bp > M \end{cases}, & t \ge rt(bp) \\ N/A, & t < rt(bp) \end{cases} \quad (S3)$$

, where $rt(bp)$ is the "replication time" at which the chromosomal locus bp is duplicated ($20 \le rt(bp) \le 110$ minutes).

RT-qPCR gene expression

The effects of gene position on the transcription rate of the *eyfp* gene driven by various promoters were determined by measuring *eyfp* mRNA levels with RT-qPCR. To obtain RNA samples, 0.5 mL of cells with OD_{600} = 0.3-0.5 were centrifuged for 3 minutes at 15,000 r.p.m. in a benchtop centrifuge at 4°C temperature. Cell pellets were immediately flash frozen in liquid nitrogen. The pellets were resuspended in TRIzol (Ambion) and extracted using Phase Lock Gel-Heavy tubes (5 PRIME), and RNA was purified using the RNA Clean and Concentrator-5 kit (Zymo Research). Genomic DNA was eliminated by treating the samples twice with 1 MBU Baseline-ZERO DNAse (Epicentre) at 37°C for 20 minutes. RNA was recollected using Zymo-Spin columns and subsequently reverse transcribed using the SuperScript III reverse transcriptase kit (Invitrogen). Following reverse transcription, remaining RNA was degraded via RNAse H treatment, and the cDNA was diluted tenfold before beginning qPCR.

Expression levels were determined using on an Applied Biosystems 7500 Fast Real-Time PCR system, using 7500 Software v 2.0.1. The 15 mL qPCR reaction contained 2 mL of cDNA, 7.5 mL of SYBR Green Dye master mix and 5.5 mL of primer mix. The primer mix contained the forward and reverse primers to form ~100 base-pairs amplicons in the genes of interest, at a final

primer concentration in the reaction of 230 nM. Expression measurements were then made by comparing cycle-threshold (C_T) of the amplicons of interest to an internal standard amplicon in *rho*, a house-keeping gene that is insensitive to cellular concentrations or activity of CtrA. As a negative control, we verified the removal of genomic DNA template contamination by measuring C_T of RNA samples not treated with reverse transcriptase. We additionally measured amplification of a genomic DNA standard curve to verify that the Rho and eYFP amplicons formed unique products and with amplification efficiencies within 10% of one another: we measured amplification efficiencies of 96.86% and 95.85%, respectively. Data was analyzed using the delta–delta-C_T method (Schmittgen and Livak, 2008) or the normalized ratio method (Pfaffl, 2001). Final gene expression measurements represent the average and s.d. of three biological replicates, each composed of at least two technical replicates.

Modeling an array of CtrA~P gradients and their effect on transcription of a CtrA- regulated gene

To determine what qualitative features would match our transcriptional data, we explored three types of CtrA~P concentration gradient profiles in predivisional cells: linear, exponential, and sigmoidal (Figures 3A and 3B):

$$CtrA{\sim}P(x) = \alpha \cdot (L - \beta x) \quad 0 \le \beta \le 1 \quad (S4)$$

$$CtrA{\sim}P(x) = \alpha \cdot e^{-(\frac{x}{L})/\beta} \quad 0 < \beta \le 1 \quad (S5)$$

$$CtrA{\sim}P(x) = \alpha \cdot \frac{\gamma^n}{\gamma^n + x^n} \quad \begin{matrix} 0 \le \gamma \le L \\ 0 < n \le 20 \end{matrix} \quad (S6)$$

, where in all three cases the phosphate source resides at the new pole, at $x = 0$. L is the length of the cell ($0 \le x \le L$) and α is the concentration of CtrA~P at $x = 0$. β determines the steepness of the linear and exponential decrease in equations S4 and S5, while γ determines the start position of the gradient and n its steepness in equation S6.

CtrA~P binds multiple promoters cooperatively (Reisenauer et al., 1999; Siam and Marczynski, 2000). Because CtrA~P binds P_{350} as a dimer (Zhou et al., 2015), it is likely to exhibit cooperative activity when promoting the transcription of *350* mRNA as well. Accordingly, we modeled the transcriptional response from P_{350} as a Hill function (Equation S7).

$$\frac{[mRNA_i(t)]}{dt} = k_s \cdot \frac{[CtrA{\sim}P(x_{i1})]^n}{{K_1}^n + [CtrA{\sim}P(x_{i1})]^n} + k_s \cdot \frac{[CtrA{\sim}P(x_{i2})]^n}{{K_1}^n + [CtrA{\sim}P(x_{i2})]^n} - k_d \cdot [mRNA_i(t)] \quad (S7)$$

, where $[mRNA_i(t)]$ is the concentration of *eyfp* mRNA integrated at site (i=1,2,3,4) as a function of time. The first two terms model synthesis of *eyfp* mRNA from each chromosome. k_s is the maximum transcription rate of the *eyfp* gene, K_1 is the binding constant between CtrA~P and the *350* promoter and n is the Hill coefficient describing the degree of cooperativity. x_{i1} is the spatial position of the *eyfp* gene in the original chromosome while x_{i2} is the spatial position of the gene on the newly replicating chromosome. The last term models first order degradation of *eyfp* mRNA with rate constant k_d. The value of the Hill coefficient, n, was fitted to match *in vivo* measurements of CtrA~P levels in the cell and time resolved RNAseq measurements of P_{350} promoter activity, with k_s, K_1, and k_d defined by published biochemical measurements (Table S5, Figure S3A).

A spatiotemporal model of CckA activation pathway

We constructed a spatiotemporal model that tracks the concentration and phosphorylation state of CckA, ChpT, and CtrA throughout predivisional *Caulobacter* cells, defining the cell cytoplasm and the two microdomains at the new and old poles as three distinct environments. In the interest of simplicity, we work in one spatial dimension with the variable $0 \leq x \leq L$ corresponding to the distance from the new pole. The following assumptions and experimental observations are used to set the kinetic and thermodynamic parameters of the model. These assumptions and parameters

were used to calculate the spatiotemporal evolution of protein concentrations with the algorithm described in the "Governing Equation" section below.

Protein copy number

We combined RNA-seq and ribosome profiling datasets collected at six time points over the cell cycle (Schrader et al., 2016), protein localization profiles (Figure 1B-D), and protein abundance measurements (Bowman et al., 2008; Chen et al., 2009; Jacobs et al., 1999), to determine the copy number of PopZ, CckA, and ChpT proteins as a function of time in the cell cycle. In *Caulobacter* (as in *E. coli*), the density of ribosomes bound to mRNA of a given gene is proportional to the synthesis rate of the protein encoded by that mRNA (Li et al., 2014; Schrader et al., 2016). To determine the proportionality between ribosome density and synthesis rate, we divided the average ribosome density for all genes by the total amount of proteins synthesized during one cell cycle when grown in minimal media (Schrader et al, personal communication). From this relationship and the measured ribosome density of each gene, we calculated translation rates of 55, 5, and 10 molecules per cell per minute for PopZ, CckA, and ChpT, respectively. We combined our protein localization profiles prior to cell division (Figure 1B-D) with correct partition protein quantities between the two daughter cells, and *in vivo* measurements showing that these three proteins are all present in constant levels throughout the cell cycle (Bowman et al., 2008; Chen et al., 2009; Jacobs et al., 1999). Using these parameters, we could then estimate that the cell maintains 3500±200 copies of PopZ, 400±50 copies of CckA and 1200±80 copies of ChpT. We could not use our approach to determine protein copy number for CtrA, as its levels vary throughout the cell cycle due to regulated transcription and targeted proteolysis (Domian et al., 1997; Reisenauer et al., 1999). Instead, we used previously published measurements of CtrA copy number: 9500±2000

molecules of CtrA in a swarmer cell and 22000±4000 molecules in a predivisional cell (Judd et al., 2003).

Protein localization and polar K_D values

Quantitative analysis of epifluorescence images shows that CckA, ChpT, and CtrA accumulate at both the new pole and old pole microdomains (Figure 1B-D). While we observed that movement of each of these molecules was slowed inside the polar microdomain (Figures 4 and 5), it is important to note that reduced diffusion at the poles is not sufficient to localize proteins. This follows from Fick's second law given inhomogeneous diffusion (Equation S8)

$$\frac{\partial C(x,t)}{\partial t} = \mathrm{D(x)} \cdot \frac{\partial C^2(x,t)}{\partial x^2} + \frac{\partial D(x)}{\partial x} \cdot \frac{\partial C(x,t)}{\partial x} \quad (S8)$$

, where $C(x,t)$ is the protein concentration at position x and time t and $D(x)$ is its local diffusion coefficient at position x. Considering an initial condition of homogeneous distribution ($\partial C/\partial x = 0$), it is clear that while variation in D(x) might affect the time evolution of a concentration gradient, such variation cannot cause passively diffusing particles to be concentrated. Similarly, as we show in Figure S3D, an initial distribution focused at the poles quickly relaxes to a homogeneous distribution. In other words, to form foci, there must be an attractive free energy difference at the poles, not just a reduction in diffusion coefficient. Of course, the apparent reduction in single-molecule diffusion coefficient we observe within the polar regions provides support for such local binding interactions.

Given that CckA, ChpT, and CtrA form foci at the cell poles, the question becomes what attracts them there. While biomolecules can be localized to the poles by several potential mechanisms (such as sensing of polar curvature (Lenarcic et al., 2009; Ramamurthi and Losick, 2009) or occlusion of large aggregates by the chromosome (Coquel et al., 2013; Laloux and

Jacobs-Wagner, 2013)), we expect the primary attractive effect for CckA, ChpT, and CtrA proteins is direct binding to polar binding partners. These include either PopZ itself, or in the case of CtrA, to ChpT and other polar proteins localized by PopZ (*i.e.* indirect recruitment). Because measuring these (multiple) binding interactions *in vivo* is not tractable, we defined a set of virtual binding sites on a "new pole" or "old pole" species to represent these interactions. The concentration of available microdomain binding sites and the rates of association and dissociation to the microdomain determine the extent of the polar accumulation of CckA, ChpT, and CtrA at steady state, which is defined empirically by our polar localization measurements.

We applied the Nelder–Mead minimization procedure (Nelder and Mead, 1965) to determine the K_D of CckA, ChpT, and CtrA to the microdomain in a simplified system composed of coupled diffusion and binding reactions (reactions 9-12,19-30 in Table S6). At each step of the optimization procedure we ran our system to steady state and used a Gaussian function (Equation S9) to score the distribution of CckA, ChpT, and CtrA at the poles.

$$\sum_{1\le i\le 6} e^{\left(\frac{f_i-\overline{f}_i}{\sigma_i}\right)^2} \quad (S9)$$

, where f_1 , f_3 , f_5 are the concentrations of CckA, ChpT, and CtrA at the new pole microdomain and f_2 , f_4 , f_6 are the concentrations of CckA, ChpT, and CtrA at the old pole microdomain. σ_i is determined based on measured standard deviation of protein localization profile (Figure S1B).

CckA k_{off} from the microdomain

We fitted the unbinding rate of CckA from the new pole microdomain to match the following data: (i) derived K_D's between the microdomains and CckA, (ii) measured diffusion coefficients of CckA at the body of the cell and the two microdomains, (iii) timescale of fluorescence recovery

and loss at the old and new poles. Starting from steady state, we marked CckA molecules at the old pole microdomain as "bleached" and simulated CckA molecules recovery and loss at the old and new pole microdomains by tracking the concentration of the "unbleached" CckA molecules. We ran the simulation with different k_{off} between CckA and the microdomains and looked for a range of k_{off} values that would match our data of fluorescent recovery and loss at the poles, achieving good agreement.

CckA autokinase activity

CckA acts as an auto-kinase-only when it accumulates at the new cell pole of the predivisional cell, where it introduces phosphate to the CtrA pathway (Iniesta et al., 2010a; Jonas et al., 2011 Curr. Biol. 2011; Mann et al., 2016; Tsokos et al., 2011). CckA autokinase activity is density dependent in *vitro* (Mann et al., 2016). CckA molecules densely packed on 100 nm diameter liposomes (~6200 molecules/μm^2) exhibited 10-fold higher autophosphorylation at the assay ten minutes' end point than CckA in the sparsely packed state (~650 molecules/μm^2, maintaining the same total CckA copy number between experiments), with activity at intermediate CckA concentrations increasing monotonically. The density-dependent activity of CckA was fitted to a sigmoidal curve with a concentration at half-maximal velocity (H) of 2615 molecules/μm^2 and exponential (n) of 1.6 (Mann et al., 2016) (Equation S10). We scaled the value of H from the observed *in vitro* Hill function based on constraints from the following *in vivo* observations: (i) CckA levels are constant throughout the cell cycle, (ii) the percent of phosphorylated CckA molecules is low in swarmer cells and is 50% at the 90 minute and 120 minute time points (Jacobs et al., 2003), (iii) CckA acts as a kinase exclusively at the new pole of the predivisional cell (i.e.

only new-pole CckA, 60% of the total, may be phosphorylated), and (iv) the calculated CckA has a local density of 5,000-10,000 molecules/μm^2 at the new pole, as described below.

These measurements indicated a set number and density of CckA molecules at the new pole, and that these molecules were rapidly and almost completely phosphorylated upon the cell reaching predivisional phase. To match this behavior, we linearly scaled the CckA activity derived from *in vitro* data by a constant factor γ such that: (i) 90% of CckA molecules at the new pole would be phosphorylated in predivisional cell steady state and, (ii) the system would reach the steady within ten minutes of simulation time.

CckA phosphatase activity

Unlike its kinase activity, , the phosphatase activity of CckA is density independent and can occur anywhere away from the new pole microdomain (Mann et al., 2016). CckA kinase activity is inhibited and its phosphatase activity is promoted by binding to either the second messenger cyclic diguanylate (c-di-GMP) (Lori et al.; Mann et al., 2016), the DivK~P-DivL complex (Childers et al., 2014), or to DivL molecules (Mann, unpublished). *In vitro* measurements show that CckA~P half-life is reduced from ~25 minutes (Mann et al., 2016) to 3 minutes when bound to c-di-GMP (Dubey et al., 2016), and to 2.5 minutes when bound to DivL (Mann, unpublished). We expect CckA phosphatase activity to be promoted in predivisional cells due either to binding to c-di-GMP, which are present in intermediate levels in predivisional cells (Abel et al., 2013), or binding to DivL that is found across the cell membrane (Iniesta et al., 2010b). Accordingly, we set the CckA~P half-life to 3 minutes in our simulations of predivisional cells.

Governing equation

Concentrations of each molecular species (C_i) in the system were modeled as a function of position along the long axis of the cell (x), and time (t). The governing partial differential equation (PDE) for each species is (Equation S10):

$$\frac{dC_i(t)}{dt} = \sum_i \alpha_i \cdot C_i(t,x) + \sum_{i,j} \beta_{i,j} \cdot C_i(t,x) \cdot C_j(t,x) + \gamma \cdot \sum_{i \in L} \frac{[\sum_{i \in L} C_i(t,x)]^n}{H^n + [\sum_{i \in L} C_i(t,x)]^n} \cdot C_i(t,x) \quad (S10)$$

$$+ D(x) \cdot \frac{\partial^2 C_i(t,x)}{\partial^2 x} + \frac{\partial D(x)}{\partial x} \cdot \frac{\partial C_i(t,x)}{\partial x}$$

where the first term includes all first order reactions of species C_i at rate α_i, such as (de)phosphorylation and unbinding. The second term describes all second order reactions (such as binding) between species C_i and C_j with rate $\beta_{i,j}$. The third term models the auto-kinase activity of CckA as a Hill function (Mann et al., 2016) (CckA autokinase activity above), where L is the set of indexes of CckA species (*e.g.* CckA, CckA~P, CckA-ChpT). The last term defines diffusion, where D(x) is the diffusion coefficient as a function of cellular microdomain environment (Equation S11):

$$D(x) = D_{NP} + \frac{(D_B - D_{NP})}{2} \cdot \left(\tanh\left(\frac{x - NP}{s_1}\right) + 1\right) - \frac{D_B}{2} \cdot \left(\tanh\left(\frac{x - OP}{s_1}\right) + 1\right) \quad (S11)$$

$$+ \frac{D_{OP}}{2} \cdot \left(\tanh\left(\frac{x - OP}{s_1}\right) + 1\right)$$

where D_{NP}, D_B, and D_{OP} are diffusion coefficients at the new pole, cell body, and the old pole. *NP* and *OP* are the boundary positions for the new pole and the old pole microdomains (*NP*=0.2 and *OP*=3.75). To avoid unphysical behavior resulting from a sharp step function in diffusivity, we smoothed $D(x)$ with smoothing coefficient s_1.

The solution to these equations was approximated as a set of ordinary differential equations (ODEs). The spatial dimension of a 4 μm cell is discretized into n = 80 bins, each representing a

0.05 μm section of the cell. Each species is broken into *n* sub-species, one per bin. The simulation advances in 0.1 second steps. We use the second-order center difference formula to approximate the Laplacian operator and convert each PDE into a set of ordinary differential equations (ODEs), Equation S12:

$$\frac{dC_i(t)}{dt} = reaction\ terms + D_{i-1} \cdot \frac{C_{i-1}(t) - C_i(t)}{h^2} + D_{i+1} \cdot \frac{C_{i+1}(t) - C_i(t)}{h^2} \quad (S12)$$

where D_i is a discretization of $D(x)$. We ensure flux into and out of the bins is balanced by matching flux at the boundaries.

Sensitivity analysis

To measure sensitivity, we varied the value of each of the 17 critical parameters in Table S6 over 3 orders of magnitude from its established literature value, across multiple combinations of all other parameters, and calculated the averaged impact this change had on the system. Simultaneously, we assessed whether small changes in other parameters could negate the effect caused by the large change in the parameter of interest. Parameters were deemed sensitive if alterations to their values irreparably altered CtrA phospho-gradient properties, indicating the importance of that parameter.

Single-molecule imaging optics and acquisition

Two-color, 3D single-molecule imaging with eYFP and PAmCherry labels was performed using a microscope setup and protocols similar to previously published studies (Gahlmann et al., 2013; Ptacin et al., 2014) with minor modifications. Briefly, we employed an inverted microscope (Nikon Diaphot 200) with an oil-immersion, super-corrected objective (Olympus PLAPON60XOSC, 60X/NA1.4). The sample was illuminated with an activation wavelength of 405 nm (Coherent,

OBIS 50 mW), and with detection lasers at 514 nm (Coherent, Sapphire 514-100 CW) and 561 nm (Coherent, Sapphire 561-100 CW diode-pumped solid state lasers in an epifluorescence (wide-field) configuration. Laser light was directed to the sample and emission filtered by the microscope dichroic mirror (Chroma, zt440/514/561rpc), and fluorescence was further selected with appropriate filters for eYFP and PAmCherry: a 514 nm long pass filter (Semrock, LP02-514RE), 561 nm notch filter (Semrock, NF03-561E) and dual band pass filter (Semrock, FF01-523/610). The fluorescence from eYFP and PAmCherry was collected with a f = 400 mm tube lens, split with a 560 nm dichroic (Semrock, FF560-FDi01) and directed through two 4f imaging systems each using f = 120 mm lenses to form a 2.54 mm diameter Fourier transform of the image. Quartz-relief phase masks for each emission wavelength (Gahlmann et al., 2013) (Double-Helix Optics, LLC) were placed at the Fourier plane with high-repeatability magnetic mounts to generate the double-helix PSF for 3D imaging, and were removed for 2D imaging. Phase mask alignment was confirmed by using a dense sample of fluorescent beads to image the overlap of the phase mask and the Fourier plane of the microscope, with an auxilliary single-lens imaging system focused at the Fourier plane of the 4f system. Single-molecule fluorescence data were collected on separate regions of an EMCCD camera (Andor Ixon DU-897E).

In all cases, eYFP labels were used for single-molecule tracking and PAmCherry labels were used for super-resolution imaging of PopZ. Under our expression conditions, many fluorescently labeled proteins are present in every cell: to ensure that only one actively fluorescent emitter was present simultaneously, emitters were either shelved in transient dark states which stochastically recover (eYFP) or were stochastically photoactivated from the dark state (PAmCherry). For CckA/PopZ imaging, data was taken with an interleaved-illumination sequence of frames with 100 ms integration times. A typical acquisition sequence used 40 frames with 514

nm illumination for acquisition of CckA-eYFP data followed by 5 frames with only 405 nm illumination, 35 frames with both 405 and 561 nm illumination to image activated PAmCherry-PopZ molecules, and 5 dark frames before restarting the cycle. For tracking of all other proteins (ChpT, CtrA, fPIF-eYFP, eYFP), data was taken with a sequential illumination sequence, beginning with eYFP imaging with 514 nm illumination using 20 ms integration times followed by PAmCherry-PopZ imaging with both 405 and 561 nm illumination and 100 ms integration times. Typical irradiances were ~0.1-0.5 kW/cm^2 for 514 nm and 0.5-3 kW/cm^2 for 561 nm light; to maintain an optimal density of active PAmCherry emitters, the 405 nm irradiance was increased manually over the course of the acquisition by adjusting a continuously variable neutral density filter, and typical irradiances were in the range of ~0.1-10 W/cm^2.

Sample preparation for single-molecule experiments

Samples of *Caulobacter* cells were prepared for single-molecule microscopy by outgrowth of frozen -80°C stocks in PYE at 28°C for 8 hours, followed by inoculation into M2G and overnight growth. Liquid cultures were spun down (3 minutes, 8,000 r.p.m.) at an OD_{600} = 0.3-0.5 and were washed 2-3x in clean M2G at room temperature. Cell pellets were suspended in M2G at a final concentration of 20-50x relative to growth conditions. Fluorescent polystyrene beads (100 nm 540/560 FluoSpheres, Life Technologies) were sonicated for 3 minutes before addition to a final concentration of roughly 10^5/μL, providing 1-4 beads in each ~30 μm field of view. 1 μL of suspended cells was added to 1.5% agarose/M2G pads and imaged on 22x22 mm^2 no. 1.5 glass coverslips (Fisher 12-541-B or VWR 48366-227) that had been cleaned by etching in argon plasma for 10-15 minutes.

To maximize the number of predivisional cells in some experiments with ChpT and CtrA-eYFP-14, cells were synchronized as described above. Cells were collected in M2 and either immediately prepared for recovery or stored on ice until use (< 4 hours). For recovery, cells were suspended in M2G and let progress through the cell cycle at 28°C for 50 minutes before beginning the spin-down protocol above. Predivisional cells recovered through a synchrony and those from within a mixed population (defined by cell length and bipolar PopZ foci) exhibited similar behavior in terms of protein diffusivities and localization profiles, but quantitative analysis for ChpT-eYFP and CtrA-14-eYFP reported in the main text was derived from synchronized cell populations only. Results reported for CckA, ChpT, and CtrA used predivisional cells with clearly identifiable old and new poles judged by the presence of a stalk in the brightfield images and/or dramatically different PAmCherry-PopZ copy numbers (as the new pole contains fewer PopZ molecules than the old pole).

For strains with inducible PAmCherry-PopZ or eYFP tagged proteins, we used relatively low amounts of inducing agent for single-molecule experiments: either 0.06-0.09% xylose or 100-150 uM vanillate. When imaging mixed populations, induction was performed for 60-90 minutes before preparation for imaging, while for synchronies, induction was begun 60 minutes before synchrony and continued during the recovery phase.

Processing of single-molecule data

All analysis was performed using custom scripts written in Matlab (The Mathworks, Inc., Natick, MA) except as noted below. For 3D imaging using the double-helix PSF, we used a modified form of the Easy-DHPSF analysis suite (Lew et al., 2013 Prot. Exch. 2013). Following single-molecule localization, all data were registered into the yellow channel (eYFP) coordinate space for

visualization of tracks and super-resolution reconstructions and for all downstream quantitative analysis. Multicolor registration in 3D was performed using a locally weighted quadratic function optimized by least-squares error (Gahlmann et al., 2013) using a nanohole array to generate field-dependent calibrations and to acquire control points as described in (von Diezmann et al.) for each day of experiments. 1000s of control points were used to generate each transformation function, with rms target registration errors of 9-18 nm. For 2D imaging, we used ThunderSTORM (Ovesny et al., 2014 Bioinformatics 2014) to localize single molecules from raw data, then performed further analysis using custom scripts. Multicolor registration in 2D was performed using the fitgeotrans function of Matlab with an affine transformation using dozens of control points generated with fluorescent beads, providing rms fiducial registration errors of < 5 nm.

For both 2D and 3D data, the effects of drift were removed by localizing fiducials in each frame and subtracting out sample translations. Fiducial localization precision in each frame was generally < 5 nm, and was reduced further by low-pass filtering with a boxcar average or wavelet filter (Gahlmann et al., 2013). Fiducials in different parts of the field of view gave the same correction within 10 nm, suggesting that a rigid translation was appropriate for drift compensation over the field of view. When more than one fiducial was present, we used the average of the fiducials' motion. Localizations were filtered to avoid false positives by using PSF parameters including interlobe distance and size (for 3D imaging with the DH-PSF) and total amplitude (for both 2D and 3D imaging), and overlapping localizations were not analyzed.

Super-resolution reconstructions of the PopZ matrix shown in Figure 4 and Figure 5 were generated by convolving point localizations with a 2D (3D) Gaussian kernel with $\sigma_{x,y}$ ($\sigma_{x,y,z}$) roughly equal to the empirical localization precision. For the averaged single-molecule data

described below, data were rendered using histograms with 25 nm x 25 nm bins, with contrast ranging from 0 localizations to the maximum bin amplitude.

Definition of cellular coordinate systems and polar averaging analysis

Single-molecule localizations were transformed from lab coordinates to the local coordinate system of their cells for image rendering and quantitative analysis. The cell axis was defined by a low-order polynomial fit to a brightfield image of the cell, with points along the cell axis either defined from maximum intensity or by manual selection. Because the brightfield image only provides 2D information and may not be exactly aligned with fluorescence data, the cell axis fit was registered to single-molecule data by minimizing the least squares distances from single-molecule localizations to the nearest point on the backbone. For 3D data, the *z* position of the backbone was allowed to vary as a quadratic function of length along the cell axis in the minimization. For 3D CckA data on the membrane, the fit was optimized to minimize the error between localizations and a locally cylindrical envelope centered on the cell axis.

The new and old poles were user-defined based on the observation of a stalk in the brightfield image as well as the relative size of the PopZ microdomains (smaller at the new pole). Polar PopZ localizations were used to classify molecules as belonging to the poles by scoring each localization's position relative to a threshold of local PopZ density. In 3D, the PopZ densities were defined along the cell axis coordinate, where PopZ localizations were convolved with a Gaussian kernel. In 2D, polar densities were defined by fitting a 2D histogram of PopZ localizations to an elliptical 2D Gaussian function. (We achieved similar results regardless of the exact method chosen.)

For polar averages (Figure 4C, Figure 5E), polar coordinate systems were defined relative to the centroid of polar PAmCherry-PopZ localizations, oriented relative to the cell axis fit described above. Ventral vs. dorsal positioning was preserved by defining the local coordinate systems $\{x, y, z\}$ with x the tangent to the cell axis at the pole, y the dorsal projection in plane of the cell axis, and z perpendicular to the plane of the cell axis.

Analysis of CckA density in the PopZ-adjacent membrane

We obtained the radius of hemispherical CckA at the old poles from the radial distances of all polar CckA molecules ($x > 0$, for x along the cell axis and $x = 0$ defined by the PopZ centroid). As shown in Figure 4C, these values were weighted by $1/r^2$ to account for the volume scaling of hemispherical shells. The weighted mean radial value of CckA at the old poles was $r_{\text{old}} = 108$ nm. As shown in Figure S4, this approach did not work at the new poles, as the PopZ microdomain was more oblate and did not approximate a hemisphere. Instead, we chose to define CckA's dimensions on the new pole membrane from the full-width at half-maximum (FWHM) defined by the standard deviation of CckA distributions along the transverse axes multiplied by $2\log(2)$. The radius was thus the half-width at half-maximum, with geometric mean value $r_{\text{new}} = 82$ nm.

To calculate polar surface area, we used the relations for a hemisphere and for a circle respectively: $A_{old} = 2\pi r_{old}^2 = 0.073$ μm^2 and $A_{new} = \pi r_{new}^2 = 0.021$ μm^2. Because the new pole does exhibit a small degree of curvature, A_{new} represents a lower bound, while the equivalent value for a hemisphere (0.042 μm^2) would be a possible upper bound. However, it is likely that the value is closer to 0.021 μm^2: not only is the CckA distribution at the new pole only somewhat curved, but this value does not include contributions to the size due to both localization error (30-45 nm) and registration errors in the pole averaging.

The concentration of CckA regulates its kinase activity. *In vitro* reconstitution experiments on liposomes have shown that CckA autokinase activity per molecule scales as a Hill function, increasing at least linearly with concentration below 10,000 molecules/μm^2 (Mann et al., 2016). We expect a predivisional *Caulobacter* cell to contain on the order of 350 molecules of CckA (SI), and from our intensity profiling experiments (Figure 1C), this implies an average of 210 and 95 CckA molecules within the new and old poles, for concentrations of ~5,000-10,000 and 1,250 molecules/μm^2, respectively, using the areas calculated above. Given the ~3 nm radius of CckA (Mann et al., 2016), this corresponds to ~14-28% and 3.5% of the polar membrane by area at the new and old poles. By contrast, the nonpolar area of the *Caulobacter* cell has a surface area of ~5 μm^2 and only 13% of cellular CckA molecules, resulting in a concentration of 9 molecules/μm^2. The ~500-1,000-fold dilution factor of CckA outside the new pole is itself sufficient to ensure that CckA away from the poles cannot act as a source for the CtrA phospho-cascade.

Analysis of single-molecule tracking dynamics

We extracted trajectories of single proteins fused to eYFP from processed single-molecule localizations (i.e. a matrix of $\{x\ y, z, t\}$ values). Trajectories we generated by chaining together localizations that belonged to the same cell and had a maximum time interval Δt and Euclidean distance Δr. To avoid categorization errors, if at any time two localizations appeared in the same cell in the same frame, they and the tracks they belonged to were discarded. Δr was set based on the typical displacement of the molecule per frame due to diffusion, with values of 300 nm for CckA and 800 nm for cytoplasmic proteins. Δt was set based on the false negative (molecules blinking or localizations not passing amplitude and shape filters) and false positive (noise erroneously fit as a molecule, new molecules turning on within the cell) localization rates. For 3D

data, Δt values could be set up to 10-15 frames while maintaining false positive rates less than 5%, owing to low background, robust identification of the DH-PSF, and relatively slow rates of eYFP molecule photorecovery. For 2D data, Δt was set to 1 frame (continuous, no missed localizations) to avoid contamination by false positives appearing due to noise in the data, which is more difficult to filter out for the standard PSF (single bright spots are more common than two bright spots of well-defined separation, as for DH-PSF data analysis). We detected virtually no spurious tracks of 2 or more frames outside of cells for 2D imaging.

Mean-squared-displacement analysis was performed using the average displacements from all tracks belonging to a given population (stalked pole, swarmer pole, cell body). For ChpT and CtrA, swarmer and stalked poles gave statistically indistinguishable results and were pooled to increase statistical strength. Fits to 3D CckA data used an adapted form of the standard equation for Brownian motion including static and dynamic errors (Savin and Doyle, 2005):

$$MSD(\tau) = 4D\tau - \frac{4D\Delta t}{3} + 2\sigma_x^2 + 2\sigma_y^2 + 2\sigma_z^2 \qquad (S13)$$

with frame integration time Δt and lag time τ, with diffusion coefficient D and total dynamic error $(2\sigma_x^2 + 2\sigma_y^2 + 2\sigma_z^2)$ as free parameters determined using nonlinear least-squares estimation. This equation assumes isotropic 2D Brownian motion in the local plane of the membrane, with added 3D measurement error. While this neglects the curvature of the cell surface, the typical square displacement per frame for CckA ($6Dt = 0.001$ μm^2) is approximately 60x less than the square radius of curvature of *Caulobacter*. ($0.25^2 \approx 0.06$ μm^2), and in simulations, our approach accurately recovered the true diffusion coefficient (Figure S4).

For CtrA and ChpT, we used a common anomalous diffusion model including the effects of motion blur and localization precision (Backlund et al., 2015; Savin and Doyle, 2005). However, fitting the MSD curves in the cell body (shown in Figure 5F, Figure S6G) to this equation was not

able to precisely specify D and α owing to the short track durations available. We observed that the fit values of D and α were strongly correlated and were able to jointly vary while still providing good fits to the MSD curves. We show this in Figure S6H by plotting fits values of D and α generated from 200 resamples of CtrA and ChpT tracks either from the cell body or from the poles (ChpT data in the poles not shown, as this motion is limited by the pole size as described below). While this prevented us from precisely measuring α, combinations of D and α obtained from the fits all yielded similar apparent diffusion coefficients D_{app} for a short-time Brownian approximation. We show this by calculating $D_{app} = D\tau^{1-\alpha}$ for $D_{app} = 1.8$ μm^2/s and $\tau = 20$ ms (the frame integration time, right line) or $\tau = 100$ ms (the maximum time included in the fit, left line): all obtained fit values for CtrA fall within these two time regimes of short-time diffusion coefficients. Values for ChpT begin to diverge for $\alpha < 0.2$ due to poor support in the optimization in this region, but fits to the ChpT MSD for $\alpha > 0.2$ also agreed with $D_{app} = 1.8$ μm^2/s. Thus, while this value is not precise, we use a value of $D = 1.8$ μm^2/s in our Brownian motion simulations to approximate the motion of both CtrA and ChpT, and we show that both proteins exhibit subdiffusive motion with $\alpha < 0.7$. (Because simulations of free motion within a confining cell geometry did not exhibit anomalous diffusion, as shown in Figure S6G, confinement was not the cause of the observed subdiffusion.)

By contrast, motion of CtrA in the pole fit better to the anomalous diffusion model, yielding values of $D \approx 0.006$ μm^2/s$^\alpha$ and $\alpha \approx 0.8$ (Figure S6), consistent with a short-time approximate value $D_{app} = 0.01$ μm^2/s. While it was difficult for us to define the diffusion coefficient of ChpT within the pole, as it quickly reaches the asymptotic maximum within the polar space (described below), because it reaches an MSD value of 0.003 μm^2 within 20 ms, this suggests a diffusion coefficient of at least 0.1 μm^2/s including the contribution of error. We did not observe a

statistically significant difference in the diffusivities of ChpT and CtrA between the old and new poles, though it should be noted that the extremely small volumes of the polar microdomain makes precisely discriminating such differences difficult. To estimate the static error of CtrA and ChpT for the localization error floor of Figure 5F, we fit the MSD values of both proteins within the pole using either a 1D Brownian model of a 1D anomalous diffusion model. In all cases (either model, either protein), we obtained a localization error of approximately 24 nm.

Asymptotic limits to the MSD

To determine the upper bound of MSDs within the PopZ microdomain, we can calculate the asymptotic limit of the MSD for trajectories that remain within a boundary but for which diffusion is otherwise homogeneous. For simplicity, and consistency with our experimental measurements, we will treat observations of 1D Brownian diffusion within an arbitrary-dimensional volume of maximum dimension L along the diffusion axis. As a common starting place with other analytical approaches (Kusumi et al., 1993), we note that the time evolution of the MSD is found by taking the integral over starting and ending positions

$$\langle x^2(t)\rangle = \iint_0^L (y-x)^2 P(y,t|x,0)\, P(x,0) dy\, dx \qquad \text{(S14)}$$

assuming normalization such that $\int_0^L P(x,0)dx = 1$. This shows that the propagator $P(y,t|x,0)$ determines the MSD for a given geometry, diffusivity, and initial distribution. For confined geometries in the long-time limit, the problem becomes much simpler: the value of $P(x,\infty)$ is a uniform distribution within the confining boundary regardless of initial condition or diffusion process. Given this and a uniform starting distribution, (S14) simplifies to

$$\langle x^2(\infty)\rangle = \iint_0^L (y-x)^2 P(x)P(y) dx\, dy \qquad \text{(S15)}$$

where $P(x)$ is the projection of a uniform distribution within the true volume onto the observed dimension, $\mathbb{R}^n \rightarrow \mathbb{R},\ n \epsilon [1,2,3]$. For a 1D square-well potential of length L along the x dimension, $P(x) = 1/L$, and thus

$$\langle x^2(\infty)\rangle = \frac{1}{L^2}\iint_0^L (y-x)^2\, dx\, dy = \frac{L^2}{6} \approx 0.17L^2 \qquad \text{(S16)}$$

While this is a reasonable approximation, intuitively, we know the curved shape of PopZ will generally result in more localizations appearing towards the center of the microdomain, resulting in a $P(x)$ distribution that is not constant (cf. Figure 5E). If we move to a 2D barrier (diffusion along the perpendicular axis of a hollow cylinder of diameter L), this is borne out: $P(x) = \pi \sin(\pi x/L)/2L$, and

$$\langle x^2(\infty)\rangle = \frac{\pi^2}{4L^2}\iint_0^L (y-x)^2 \sin(\pi x/L)\sin(\pi y/L)\, dx\, dy = L^2\left(\frac{1}{2} - \frac{4}{\pi^2}\right) \approx 0.095L^2 \text{ (S17)}$$

where we see that the asymptotic MSD will be lower, as molecules will appear more often towards the wider center of the microdomain. This is taken a step further for a 3D barrier (diffusion within a spheroid along the axis with diameter L), for which $P(x) = 2\sin^2(\pi x/L)/L$ and

$$\langle x^2(\infty)\rangle = \frac{4}{L^2}\iint_0^L (y-x)^2 \sin^2(\pi x/L)\sin^2(\pi y/L)\, dx\, dy = L^2\left(\frac{1}{6} - \frac{1}{\pi^2}\right) \approx 0.065L^2 \text{ (S18)}$$

Thus, for a more realistic approximation of the microdomain shape, the MSD reaches an asymptotic value of ~39% the value we would calculate using the 1D square-well approximation. The MSD of experimental localizations includes an additional error term of $2\sigma^2$ term, given our static error σ = 24 nm. Using this relation, and given a typical PopZ diameter of 150-200 nm along the cell axis, we predict an asymptotic polar MSD of 0.0026-0.0038 μm^2 including error. This was

close to the observed value of the MSD of polar ChpT-eYFP at all lag times and for CtrA-eYFP-14 at long times (~0.003 μm^2).

Motion blur of fast-moving molecules within a confined space can affect this analysis and erroneously "centralize" localizations and reduce the observed MSD (Ritchie et al., 2005). Indeed, ChpT-eYFP reached the asymptotic MSD within the first 20 ms time lag, indicating it diffuses relatively quickly within the pole. However, as ChpT and CtrA exhibited the same asymptotic MSD, and ChpT-eYFP trajectories fully explored the PopZ microdomain (Figure 5A), we do not believe motion blur significantly compromised our measurements of polar diffusion.

Analysis of ChpT and CtrA dwell times inside the poles

To determine the rate of protein turnover at the poles, we calculated the rate at which ChpT and CtrA molecules returned to the cell body after an excursion within the microdomain. Plotting the fraction of molecules remaining in the pole as a function of time, we noted that escape events were distributed roughly exponentially (i.e. linear on a semilogarithmic scale in Figure 5G). Surprisingly, simulations of free diffusion (D = 1.8 $\mu m^2/s$, no slowing at the poles) gave a similar exponential exit distribution to those of ChpT and CtrA captured by PopZ. This apparent contradiction was due to the effect of single-molecule photobleaching: of N = 434 and 1149 events from ChpT and CtrA, respectively, 77.1% and 80.9% were due to bleaching. (Bleaching was defined as the last localization of a track being within the pole, while exit events were defined as subtrajectories that inhabited the pole for at least one frame before detecting a subsequent localization outside the pole.)

Photobleaching before exit lowers the chance of detecting long-lived residence events times and thus lowers the apparent dwell times. To compensate for this effect, we fit the short-

time (≤ 100 ms, i.e. first five points) of the dwell time distributions of ChpT and of CtrA with exponentials. We scaled the resulting rates by the proportion of tracks that exited before photobleaching. This is appropriate within the approximation of competing exponential processes, which provides that 1) the rate of the either process (bleaching or exit) occurring is equal to the sum of the rates of the individual processes, and 2) that the chance of detecting a given process first is proportional to its rate. This allows us to determine the rate of exit λ_{out} from the observed decay rate, $\lambda_{decay} = \lambda_{out} + \lambda_{bleach}$ and the chance of a given decay event being due to exiting the pole p_{exit} using the relation $\lambda_{out} = (\lambda_{out} + \lambda_{bleach})p_{exit}$. Within this approximation, we calculated similar dwell times of ChpT and CtrA within the poles: 132±39 ms and 132±28 ms (95% CI), respectively. As CtrA exhibited a heavy tail (visible as the distribution curving up in Figure 5G), this is likely an underestimate of CtrA's true lifetime, consistent with its lower diffusivity within the pole compared to ChpT.

Brownian motion simulations

We performed simulations of single-particle diffusion using home-built Matlab (The Mathworks, Natick, MA) scripts. We generated normally distributed displacements with mean 0 and variance $2D\Delta t$ in each dimension to simulate Brownian diffusion in either 2D (membrane protein motion) or 3D (cytoplasmic protein motion), using time steps Δt that resulted in typical displacements $6D\Delta t < 10$ nm. In both cases, we adapted trajectories for free motion to the geometry of a 3D cylindrical cell of length *l* and radius *r* with hemispherical caps of radius *r*.

For membrane protein motion, projection of free 2D diffusion was performed in two ways, for motion of molecules within the cylindrical body vs. in the hemispherical caps. For membrane protein motion within the cylindrical body, we projected 2D motion from a 2D sheet with periodic

boundary conditions onto the cylinder. For motion within the hemisphere, we projected each displacement from its 2D manifold onto the 3D surface while ensuring that the magnitude of displacements was not changed.

For cytoplasmic protein motion, we modeling the confining boundary of the cell envelope using either absorptive or reflective boundary conditions. In both cases we achieved similar results; in the simulations present in Figure 5 and Figure S6, we use absorbing boundary conditions. For computational convenience, we simulated both behaviors similarly: 3D motion that went beyond the surface of the cell was reflected at the tangent plane of the surface, and the reflected motion was scaled either by a factor of 1.0 (full reflection) or 0.003 (absorption, avoiding problematic numerical behavior when molecules appeared to be within the cell surface).

To represent the experimental conditions, we binned the finely sampled trajectories into either 20 ms or 100 ms points to represent the effect of motion blur, then added isotropic Gaussian localization errors at each observed position of 35 nm for membrane protein trajectories or 40 nm for cytoplasmic protein trajectories.

Photobleaching experiments

Photobleaching experiments were performed using *Caulobacter* cells expressing CckA-eYFP as a full replacement and the marker StpX-mChy as an inducible merodiploid copy (THM 176, Table S3) using an LSM710 line scanning confocal microscope (Zeiss). Imaging of CckA-eYFP was performed at 43 μW power at the objective back aperture, 0.7 μs dwell time per 90 nm pixel collected with a 1 Airy Unit pinhole and 800 V PMT gain. CckA-eYFP at the old poles of predivisional cells (determined using the StpX-mChy label, Figure S5) was photobleached with high-intensity 514 nm laser light (490 μW at the objective back aperture, ~100 μs dwell time per

targeted pixel: > 1,000 larger dose than used for imaging) after which cells were imaged for many frames at set intervals without further photobleaching.

As shown in Figure S5, after photobleaching, cells exhibited further photobleaching due to the imaging laser. Further, in cells that were uniformly bleached (rather than only bleached at the pole), we observed a small overall recovery in CckA-eYFP. Because cells with a greater photobleaching dose exhibited greater recovery over time, this effect is likely primarily due to photorecovery of eYFP. There may also be a smaller contribution from synthesis of new CckA-eYFP.

To account for this further photobleaching and photorecovery, we enforced that total signal in the cell after the high-intensity targeted photobleaching pulse be constant. We did this by calculating the average decay profile of whole-cell fluorescence for multiple cells bleached under the same conditions, fit the decay to a single exponential, and divided the pole-specific photobleaching curves by this fit. Because there exists a differential spatial distribution of bleached CckA-eYFP in these cells, the true fluorescence decay profile in the absence of diffusion may be slightly spatially dependent: i.e., the bleached pole may exhibit some photorecovery, while the other pole may exhibit relatively greater bleaching. To test the effect of errors in the correction factor we used, we corrected the same data using correction factors either from cells that had not undergone targeted photobleaching, or cells that were uniformly photobleached before imaging. In both cases, we still observed both new pole loss and old pole recovery over the span of 10 minutes, indicating that the recovery we observed was not due solely to photorecovery or new CckA-eYFP synthesis, nor was loss due to photobleaching during imaging (Figure 5).

SUPPLEMENTARY FIGURES AND TABLES

Table S1. Sequences and properties of fusion proteins used in this study.

Protein pI was predicted with the ExPASy "ProtParam" tool (Swiss Institute of Bioinformatics) using the pKa values of individual residues. We obtained the same trend with other tools including "ProtCalc" (Innovagen). All masses provided for monomer forms, and all proteins are predicted to be cytoplasmic except for CckA (which contains two transmembrane domains).

Protein	Amino acid sequence	MW (kD)	Predicted pI
PAmCherry-PopZ	/PAmCherry (1-236) MVSKGEEDNMAIIKEFMRFKVHMEGSVNGHVFEIEGEGEG RPYEGTQTAKLKVTKGGPLPFTWDILSPQFMYGSNAYVKH PADIPDYFKLSFPEGFKWERVMKFEDGGVVTVTQDSSLQD GEFIYKVKLRGTNFPSDGPVMQKKTMGWEALSERMYPEDG ALKGEVKPRVKLKDGGHYDAEVKTTYKAKKPVQLPGAYNV NRKLDITSHNEDYTIVEQYERAEGRHSTGGMDELYK /Linker (237-247) PAGALINMHGT /PopZ (248-424) MSDQSQEPTMEEILASIRRIISEDDAPAEPAAEAAPPPPP EPEPEPVSFDDEVLELTDPIAPEPELPPLETVGDIDVYSP PEPESEPAYTPPPAAPVFDRDEVAEQLVGVSAASAAASAF GSLSSALLMPKDGRTLEDVVRELLRPLLKEWLDQNLPRIV ETKVEEEVQRISRGRGA	46.9	4.68
CckA-eYFP	/CckA (1-691) MADLQLQDKVSTGAPRRRFDPWLVGAAVFFVAAAALSAAP ALKAGPTTLAGLLLLLGVAGVAVLGLVAIRGSALSGGDAD QAEGFIEALAEPAALAAADGRVLAANGPWREVMGEQRRLP KGVAGSSLFAALVQARQGQMAEGMLSAGGTDYTAKVSRLA GGRLMIRLAPIVVAEPVVEDASPAPVAERAAPPPSSLDAF AGASPFGAALLEGLEPFTSRVLETNPALTTMTGAKAGVLF GDLIDAASRAEAETRLNEGRAGPYEVRLARDPSRIAHLYL YRAEGRLVAYMIDVSEQKQIELQLSQAQKMQAIGQLAGGV AHDFNNLLTAIQLRLDELLHRHPVGDPSYEGLNEIRQTGV RAADLVRKLLAFSRKQTVQREVLDLGELISEFEVLLRRLL REDVKLITDYGRDLPQVRADKSQLETAVMNLAVNARDAVR AAKGGGVVRIRTARLTRDEAIQLGFPAADGDTAFIEVSDD GPGIPPDVMGKIFDPFFTTKPVGEGTGLGLATVYGIVKQS DGWIHVHSRPNEGAAFRIFLPVYEAPAGAVAVQAVAEPAK	100.5	5.31

	PRAARDLSGAGRILFVEDEDAVRSVAARLLRARGYEVLEA ADGEEALIIAEENAGTIDLLISDVIMPGIDGPTLLKKARG YLGTAPVMFISGYAEAEFSDLLEGETGVTFLPKPIDIKTL AERVKQQLQAD /Linker (692-695) RSAT /eYFP (696-934) MVSKGEELFTGVVPILVELDGDVNGHKFSVSGEGEGDATY GKLTLKFICTTGKLPVPWPTLVTTFGYGLQCFARYPDHMK QHDFFKSAMPEGYVQERTIFFKDDGNYKTRAEVKFEGDTL VNRIELKGIDFKEDGNILGHKLEYNYNSHNVYIMADKQKN GIKVNFKIRHNIEDGSVQLADHYQQNTPIGDGPVLLPDNH YLSYQSALSKDPNEKRDHMVLLEFVTAAGITLGMDELYK		
ChpT-eYFP	/ChpT (1-225) MTETVTETTAPASPEADVQGPDFAAMLAARLCHDFISPAS AIVSGLDLLEDPSAQDMRDDAMNLIASSARKLADLLQFTR VAFGASASAENFDSRELEKLAQGVFAHVRPTLDWQIEPQA MNKPSSRAVLNIAQIAASALPAGGVATVKGVAADGRFSII ADAKGPRARLRPEVLAGLKGEPLAEGLGGPWVQAAYLNAL VRAAGGQIAVEIGEDRASIAAWVPA /Linker (226-245) GTLRSRAPENSNVTRHRSAT /eYFP (227-484) MVSKGEELFTGVVPILVELDGDVNGHKFSVSGEGEGDATY GKLTLKFICTTGKLPVPWPTLVTTFGYGLQCFARYPDHMK QHDFFKSAMPEGYVQERTIFFKDDGNYKTRAEVKFEGDTL VNRIELKGIDFKEDGNILGHKLEYNYNSHNVYIMADKQKN GIKVNFKIRHNIEDGSVQLADHYQQNTPIGDGPVLLPDNH YLSYQSALSKDPNEKRDHMVLLEFVTAAGITLGMDELYK	52.5	5.47
CtrA-eYFP-14	/CtrA (1-217) MRVLLIEDDSATAQTIELMLKSEGFNVYTTDLGEEGVDLG KIYDYDLILLDLNLPDMSGIDVLRTLRVAKINTPIMILSG SSEIDTKVKTFAGGADDYMTKPFHKDEMIARIHAVVRRSK GHAQSVIKTGDIVVNLDAKTVEVNGNRVHLTGKEYQMLEL LSLRKGTTLTKEMFLNHLYGGMDEPELKIIDVFICKLRKK LAASAHGKHHIETVWGR /Linker (218-231) GSGSGSVTRHRSAT /eYFP (232-470) MVSKGEELFTGVVPILVELDGDVNGHKFSVSGEGEGDATY GKLTLKFICTTGKLPVPWPTLVTTFGYGLQCFARYPDHMK QHDFFKSAMPEGYVQERTIFFKDDGNYKTRAEVKFEGDTL VNRIELKGIDFKEDGNILGHKLEYNYNSHNVYIMADKQKN GIKVNFKIRHNIEDGSVQLADHYQQNTPIGDGPVLLPDNH YLSYQSALSKDPNEKRDHMVLLEFVTAAGITLGMDELYK /14-aa degradation tag (471-484) GYVLRDPNEQVNAA	54.1	6.00

fPIF-eYFP	/fPIF (1-100) MMFLPTDYCCRLSDQEYMELVFENGQILAKGQRSNVSLHN QRTKSIMDLYEAEYNEDFMKSIIHGGGGAITNLGDTQVVP QSHVAAAHETNMLESNKHVD /Linker (101-120) GTLRSRAPENSNVTRHRSAT /eYFP (121-359) MVSKGEELFTGVVPILVELDGDVNGHKFSVSGEGEGDATY GKLTLKFICTTGKLPVPWPTLVTTFGYGLQCFARYPDHMK QHDFFKSAMPEGYVQERTIFFKDDGNYKTRAEVKFEGDTL VNRIELKGIDFKEDGNILGHKLEYNYNSHNVYIMADKQKN GIKVNFKIRHNIEDGSVQLADHYQQNTPIGDGPVLLPDNH YLSYQSALSKDPNEKRDHMVLLEFVTAAGITLGMDELYK	40.4	5.67
eYFP	/eYFP (1-239) MVSKGEELFTGVVPILVELDGDVNGHKFSVSGEGEGDATY GKLTLKFICTTGKLPVPWPTLVTTFGYGLQCFARYPDHMK QHDFFKSAMPEGYVQERTIFFKDDGNYKTRAEVKFEGDTL VNRIELKGIDFKEDGNILGHKLEYNYNSHNVYIMADKQKN GIKVNFKIRHNIEDGSVQLADHYQQNTPIGDGPVLLPDNH YLSYQSALSKDPNEKRDHMVLLEFVTAAGITLGMDELYK	26.9	5.58
PopZ (WT)	/PopZ (1-177) MSDQSQEPTMEEILASIRRIISEDDAPAEPAAEAAPPPPP EPEPEPVSFDDEVLELTDPIAPEPELPPLETVGDIDVYSP PEPESEPAYTPPPAAPVFDRDEVAEQLVGVSAASAAASAF GSLSSALLMPKDGRTLEDVVRELLRPLLKEWLDQNLPRIV ETKVEEEVQRISRGRGA	19.1	4.02

Table S2. Plasmids used in this study

Plasmid number	Plasmid information	Strain number	Source or reference
pXVENN-2	Integration of N-terminal *venus*-fusions at *Caulobacter* P_{xylX} locus (kanr)	MT4275	(Thanbichler et al., 2007)
pMCS-2	Integration at a *Caulobacter* site of interest (kanr)	MT4247	(Thanbichler et al., 2007)
pBVMCS-6	High-copy vector for vanillate inducible gene expression	MT4420	(Thanbichler et al., 2007)
pVYFPN-1	Integration of N-terminal *eyfp*-fusions at *Caulobacter* P_{vanA} locus (specr)	MT4242	(Thanbichler et al., 2007)
pKL400	pMSC-2 P_{xylX}::*eyfp* integrated at locus 1 (kanr)	KL6076	This study
pKL401	pMSC-2 P_{xylX}::*eyfp* integrated at locus 2 (kanr)	KL6077	This study
pKL402	pMSC-2 P_{xylX}::*eyfp* integrated at locus 3 (kanr)	KL6078	This study
pKL403	pMSC-2 P_{xylX}::*eyfp* integrated at locus 4 (kanr)	KL6079	This study
pKL410	pMSC-2 P_{350}::*eyfp* integrated at locus 1 (kanr)	KL5919	This study
pKL433	pMSC-2 P_{350}::*eyfp* integrated at locus 2 (kanr)	KL5951	This study
pKL415	pMSC-2 P_{350}::*eyfp* integrated at locus 3 (kanr)	KL5921	This study
pKL416	pMSC-2 P_{350}::*eyfp* integrated at locus 4 (kanr)	KL5922	This study
pKL412	pMSC-2 P_{pilA}::*eyfp* integrated at locus 1 (kanr)	KL6027	This study
pKL420	pMSC-2 P_{pilA}::*eyfp* integrated at locus 2 (kanr)	KL6028	This study
pKL421	pMSC-2 P_{pilA}::*eyfp* integrated at locus 3 (kanr)	KL6029	This study

pKL422	pMSC-2 P_{pilA}::*eyfp* integrated at locus 4 (kanr)	KL6030	This study
N/A	pYFPC-3 P_{cckA}::*cckA-eyfp* (rifr)	NJH429	(Iniesta et al., 2010a)
pKL229	pMCS-1 P_{chpT}::*chpT-eyfp* (specr)	KL5556	This study
pKL464	pBVMCS-6 P_{vanA}::*ctrA-eyfp*-14 (chlorr)	KL6037	This study
pKL397	pVYFPN-1 P_{vanA}::*fPIF-eyfp* (specr)	KL5885	This study
pJP341	P_{xylX}::*PAmCherry-popZ* (kanr)	eJP453	(Gahlmann et al., 2013)

Table S3. *Caulobacter* strains used in this study

Used in figures	Strain number	Description	Construction, source, or reference
N/A	*C. crescentus* CB15N	Synchronizable derivative of *Caulobacter* CB15	(Evinger and Agabian, 1977)
N/A	JP350	P_{xylX}::*PAmCherry-popZ* integrated at the P_{xylX} locus (kanr)	(Gahlmann et al., 2013)
N/A	JP643	P_{popZ}::*PAmCherry-popZ* integrated at the P_{popZ} locus (gentr)	(Gahlmann et al., 2013)
N/A	LS4473	P_{cckA}::*cckA-eyfp* integrated at the P_{cckA} *locus*	(Iniesta et al., 2010a)
1B, S1B	THM81	P_{cckA}::*cckA-eyfp* and P_{popZ}::*PAmCherry-popZ* (rifr and gentr)	JP350 transduced into LS4473
4	THM80	P_{cckA}::*cckA-eyfp* and P_{xylX}::*PAmCherry-popZ* (rifr and kanr)	JP463 transduced into LS4473

1C ,5, S1B, S6	KL5852	P_{xylX}:: *PAmCherry-popZ* and P_{chpT}::*chpT-eyfp* (kanr and specr)	pKL229 electroporated into JP350
1D ,5, S1, S6	KL6039	P_{xylX}::*PAmCHY-popZ* and P_{vanA}::*ctrA-eyfp*-14 (kanr and chlorr)	pKL464 electroporated into JP350
2A, 2B	KL5923	P_{350}::*eyfp* integrated at locus 1 (kanr)	pKL410 electroporated into CB15N
2A, 2B	KL5960	P_{350}::*eyfp* integrated at locus 2 (kanr)	pKL433 electroporated into CB15N
2A, 2B	KL5925	P_{350}::*eyfp* integrated at locus 3 (kanr)	pKL415 electroporated into CB15N
2A, 2B	KL5926	P_{350}::*eyfp* integrated at locus 4 (kanr)	pKL416 electroporated into CB15N
S2A	KL5927	P_{xylX}::*eyfp* integrated at locus 1 (kanr)	pKL400 electroporated into CB15N
S2A	KL5928	P_{xylX}::*eyfp* integrated at locus 2 (kanr)	pKL401 electroporated into CB15N
S2A	KL5929	P_{xylX}::*eyfp* integrated at locus 3 (kanr)	pKL402 electroporated into CB15N

S2A	KL5930	P_{xylX}::*eyfp* integrated at locus 4 (kanr)	pKL403 electroporated into CB15N
S2B	KL6031	P_{pilA}::*eyfp* integrated at locus 1 (kanr)	pKL412 electroporated into CB15N
S2B	KL6032	P_{pilA}::*eyfp* integrated at locus 2 (kanr)	pKL420 electroporated into CB15N
S2B	KL6033	P_{pilA}::*eyfp* integrated at locus 3 (kanr)	pKL421 electroporated into CB15N
S2B	KL6034	P_{pilA}::*eyfp* integrated at locus 4 (kanr)	pKL422 electroporated into CB15N
N/A	LS2716	Δ*ctrA*, P_{xylX}::*ctrA*D51E (specr and chlorr)	(Domian et al., 1997)
2B	KL5989	Δ*ctrA*, P_{xylX}::*ctrA*D51E, P_{350}::*eyfp* integrated at locus 1 (specr, chlorr, and kanr)	pKL410 electroporated into LS2716
2B	KL6011	Δ*ctrA*, P_{xylX}::*ctrA*D51E, P_{350}::eyfp integrated at locus 2 (specr, chlorr, and kanr)	pKL433 electroporated into LS2716
2B	KL5990	Δ*ctrA*, P_{xylX}::ctraD51E, P_{350}::eyfp integrated at locus 3 (specr, chlorr, and kanr)	pKL415 electroporated into LS2716
2B	KL5991	Δ*ctrA*, P_{xylX}::ctraD51E,P_{350}::eyfp integrated at locus 4 (specr, chlorr, and kanr)	pKL416 electroporated into LS2716

N/A	LS2535	Δ*ctrA*, P_{xylX}::*ctrA* (specr and chlorr)	(Domian et al., 1997)
2B	KL6007	Δ*ctrA*, P_{xylX}::ctrA, P_{350}::*eyfp* integrated at site 1 (specr, chlorr, and kanr)	pKL410 electroporated into LS2535
2B	KL6008	Δ*ctrA*, P_{xylX}::ctra, P_{350}::*eyfp* integrated at site 2 (specr, chlorr, and kanr)	pKL433 electroporated into LS2535
2B	KL6009	Δ*ctrA*, P_{xylX}::ctra, P_{350}::*eyfp* integrated at site 3 (specr, chlorr, and kanr)	pKL415 electroporated into LS2535
2B	KL6010	Δ*ctrA*, P_{xylX}::ctra, P_{350}::*eyfp* integrated at site 4(specr, chlorr, and kanr)	pKL416 electroporated into LS2535
5, S6	KL6055	P_{xylX}::PAmCHY-popZ, P_{vanA}::PIF-*eyfp* (kanr and specr)	pKL397 electroporated into JP350

Table S4. Integration site coordinates and replication time.

An operon composed of the *eyfp* gene driven by either P_{xylX}, P_{350}, or P_{pilA} was integrated at four sites along the right arm of the chromosome via homologous recombination based on homology with a continuous 1000 base-pairs site as indicated in by columns Start coordinate and End coordinate. The replication time estimation for these four sites is approximated based on *in vivo* characterization of cell cycle and replication fork progression (Kozdon et al., 2013; Toro et al., 2008; Viollier et al., 2004).

Site	Start coordinate (bp)	End coordinate (bp)	Replication time (minute)	Primers used to amplify the region (Forward / Reverse)
1	35,500	34,500	21.725	TGAGCTCTTAAGATCTACGTACCGGTGCAACACCTTTAGCATCACATCC/ TAGTGGATCCCCCGGGCTGCAGCTAGCGCGCGCCATGTACCTACC
2	474,500	475,500	43.775	ATCTACGTACCGGCTTCCTTGGGCGAGAGGCCTTCC / AGAACTAGTGGATCGGCACCGACATCGACATCGC
3	1,498,000	1,499,000	94.95	TGAGCTCTTAAGATCTACGTACCGGTCACCCCCTATCTCCCCGTCATCC/ TAGTGGATCCCCCGGGCTGCAGCTAGCGTGGGTCGCGATGGCGCC
4	1,976,000	1,977,000	108.85	TGAGCTCTTAAGATCTACGTACCGGTTGACGATTCCTGCGTACGAG/ TAGTGGATCCCCCGGGCTGCAGCTAGCCATTTTCTCACGGGGCGC

Table S5. Parameters for modeling P_{350}::*eyfp* expression.

Symbol	Parameter	Value	Source / Note
k_s	Maximum rate for *eyfp* gene production from the P_{350} promoter.	1.2 nM/s	Based on temporally resolved RNA-seq (Schrader et al., 2016), we estimated the number of *ccna_00350* mRNA molecules in predivisional cell to be ~ 8% of *ctrA* mRNA. Accordingly, we choose a low transcriptional rate.
K_1	Binding constant between CtrA~P and P_{350} promoter site.	8000 nM	CtrA~P directly activates expression from P_{350} promoter (Zhou et al., 2015). Its transcription activity is low in swarmer and stalked cells and peaks in late predivisional cells (Schrader et al., 2016) (Figure S3A). The binding constant is chosen such that the expression of P_{350} is fully activated when CtrA~P concentration exceeds 12000 nM.
k_d	Rate of *eyfp* mRNA degradation	0.003 1/s	Gemone-wide study of mRNA half-life in *Caulobacter* cells indicates an averaged half-life of 3.5 minutes (J. Schrader, personal communication)

Table S6. Reaction-diffusion model parameters

Rate constants, diffusion coefficients, and other key parameters used in the CtrA activation model. Reaction numbers correspond to Figure S3 A-B.

Reactions				
Reaction number	**Reaction**	**Description**	**Parameter values**	**Comments and references**
1	$CckA \rightarrow CckA{\sim}P$	CckA autokinase activity	$v_{max} \cdot \frac{[CckA + CckAP]^n}{H^n + [CckA + CckAP]^n}$ $n = 1.8$ $H = 340\ nM/\mu m^2$ $v_{max} = 0.005$	Detailed description provided in the SI section: "A spatiotemporal model of CckA activation pathway"
2	$CckA{\sim}P \rightarrow CckA$	CckA phosphatase activity	$k_1 = \frac{\log(2)}{60 \cdot 3.5} 1/s$	Detailed description provided in the SI section: "A spatiotemporal model of CckA activation pathway"
3	$CckA{\sim}P + ChpT \rightarrow CckA{\sim}PChp$	ChpT binding to CckA~P	$k_{on} = 61uM^{-1}s^{-1}$	The K_D of CckA and ChpT binding was measured *in vitro* as 61uM (Blair et al., 2013). K_D of binding between CckA~P and ChpT as well as between CckA and ChpT~P are assumed to have the same value. We set k_{off} to be 1 (1/s).
4	$CckA{\sim}PChpT \rightarrow CckA{\sim}P + ChpT$	ChpT unbinding form CckA~P	$k_{off} = 1s^{-1}$	
5	$CckA{\sim}PChpT \rightarrow CckAChpT{\sim}P$	Phosphorylation of ChpT by CckA~P	$k = 100s^{-1}$	Based on *in vitro* data showing fast completion of ChpT phosphorylation (Blair et al., 2013), we

				bound the phospho-transfer rate to 100 1/s.
6	$CckAChpT{\sim}P \rightarrow CckA{\sim}PChp$	Dephosphorylation of ChpT by CckA	$k = 100\ s^{-1}$	Same as 5
7,8	$CckA + ChpT{\sim}P \leftrightarrow CckAChpT{\sim}$	ChpT~P binding and unbinding to CckA	$k_{on} = 61uM^{-1}s^{-1}$ $k_{off} = 1s^{-1}$	Same as 3-4.
9,10	$CckA + ChpT \leftrightarrow CckAChpT$	ChpT binding and unbinding to CckA	$k_{on} = 61uM^{-1}s^{-1}$ $k_{off} = 1s^{-1}$	Same as 3-4.
11	$ChpT + CtrA \rightarrow ChpTCtrA$	CtrA binding to ChpT	$k_{on} = 61uM^{-1}s^{-1}$	We use the same K_D as measured between CckA and ChpT
12	$ChpTCtrA \rightarrow ChpT + CtrA$	CtrA unbinding from ChpT	$k_{off} = 1s^{-1}$	
13,14	$ChpT + CtrA{\sim}P \leftrightarrow ChpTCtrA{\sim}$	CtrA~P binding and unbinding to ChpT	$k_{on} = 61uM^{-1}s^{-1}$ $k_{off} = 1s^{-1}$	Same as 11-12
15	$ChpT{\sim}PCtrA \rightarrow ChpTCtrA{\sim}$	CtrA phosphorylation by ChpT	$k = 100s^{-1}$	*In vitro* measurements show fast completion of CtrA phosphorylation. We bound the phospho transfer rate to 10 1/s.
16	$ChpTCtrA{\sim}P \rightarrow ChpT{\sim}PCtr$	CtrA~P dephosphorylation by ChpT	$k = 100s^{-1}$	Same as 15

17,18	$ChpT{\sim}P + CtrA{\sim}P \leftrightarrow ChpT{\sim}PCtr$	CtrA binding and unbinding to ChpT~P	$k_{on} = 61uM^{-1}s^{-1}$ $k_{off} = 1s^{-1}$	Same as 11-12
19,20	$NP + CckA \leftrightarrow NPCckA$	CckA binding and unbinding to the new pole	$k_{on} = 100uM^{-1}s^{-1}$ $k_{off} = 0.1s^{-1}$	Detailed description provided in the SI section: "A spatiotemporal model of CckA activation pathway"
21,22	$NP + CtrA \leftrightarrow NPCtrA$	CtrA binding and unbinding to the new pole	$k_{on} = 0.0001uM^{-1}s^{-1}$ $k_{off} = 0.1s^{-1}$	Detailed description provided in the SI section: "A spatiotemporal model of CckA activation pathway"
23,24	$NP + ChpT \leftrightarrow NPChpT$	ChpT binding and unbinding to the new pole	$k_{on} = 0.01uM^{-1}s^{-1}$ $k_{off} = 0.1s^{-1}$	Detailed description provided in the SI section: "A spatiotemporal model of CckA activation pathway"
25,26	$OP + CckA \leftrightarrow OPCckA$	CckA binding and unbinding to the old pole	$k_{on} = 10uM^{-1}s^{-1}$ $k_{off} = 0.1s^{-1}$	Detailed description provided in the SI section: "A spatiotemporal model of CckA activation pathway"
27,28	$OP + CtrA \leftrightarrow OPCtrA$	CtrA binding and unbinding to the old pole	$k_{on} = 0.1uM^{-1}s^{-1}$ $k_{off} = 1s^{-1}$	Detailed description provided in the SI section: "A spatiotemporal model of CckA activation pathway"
29,30	$OP + ChpT \leftrightarrow OPChpT$	ChpT binding and unbinding to the old pole	$k_{on} = 10uM^{-1}s^{-1}$ $k_{off} = 0.1s^{-1}$	Detailed description provided in the SI section: "A spatiotemporal model

				of CckA activation pathway"
Species				
Protein name, diffusion reaction numbers	**Copy number**	**Diffusion coefficients (starting conditions for sensitivity analysis)**	**Measured diffusion coefficients (new pole, old pole, body)**	**Comments and references**
New pole	1500±150	0	N/A	Detailed description provided in the SI section: "A spatiotemporal model of CckA activation pathway"
Old pole	3000±150	0	N/A	Detailed description provided in the SI section: "A spatiotemporal model of CckA activation pathway"
CckA 31,34,37	400±50	0.0196±0.002	31: 0.0022 ± 0.0013 34:0.0082 ± 0.0020 37: 0.0040 ± 0.0014	As proxy, we used measured values for NagE-YFP from *E. coli* (Kumar et al., 2010). Measured values reported in Figure 4
ChpT 32,35,38	1200±50	0.67±0.02	32: 0.03 35: 0.3 38: 0.03	As proxy, we used measured values for DnaK-YFP from *E. coli* (Kumar et al., 2010).

				Measured values reported in Figure 5.
CtrA 33,36,39	15000±3000	0.04±0.02	32: 0.03 35: 0.3 38: 0.03	As proxy, we used measured values for a lac repressor from *E. coli* (Elf et al., 2007). Measured values reported in Figure 5.

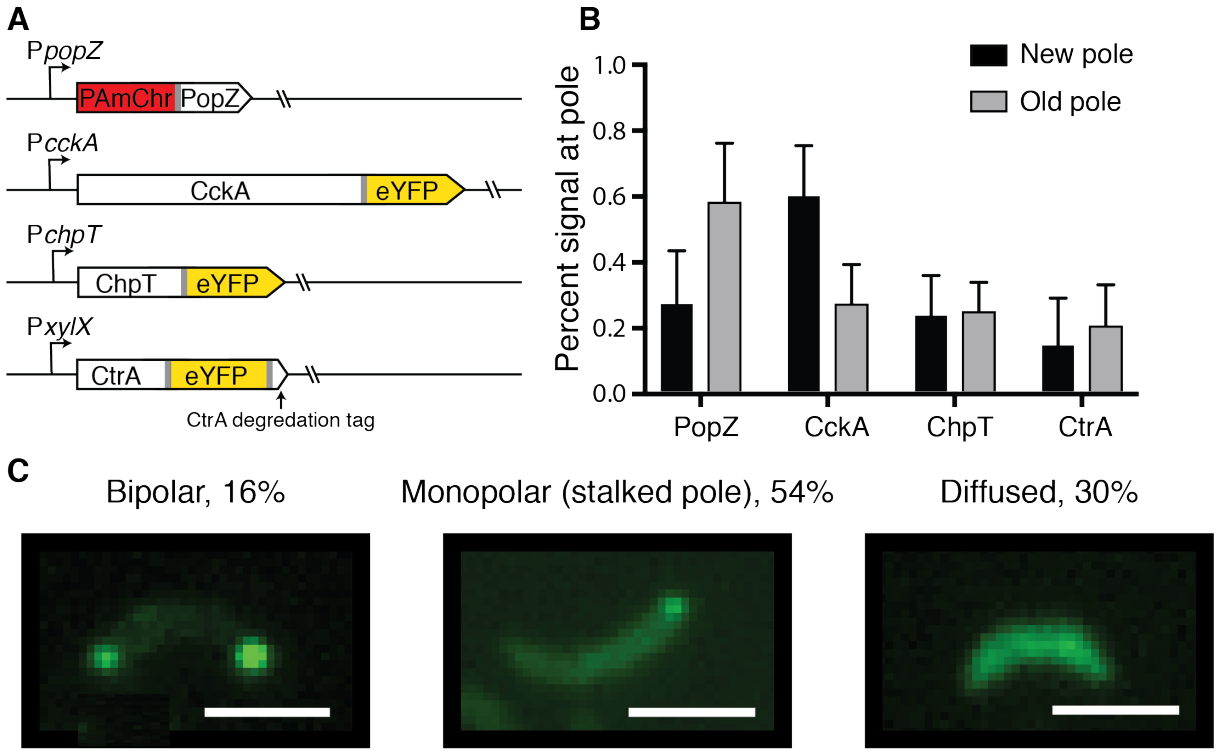

Figure S1. Localization profiles of PopZ, CckA, ChpT, and CtrA, related to Figure 1.

(A) Schematic of the fluorescence constructs used to image the co-localization of CckA, ChpT, and CtrA with respect to PopZ. Gray spacers indicate linkers. PAmCherry-*popZ*, *cckA-eyfp* and *chpT-eyfp* are driven each by their native promoters, integrated at the native locus to replace their corresponding wildtype genes. To image CtrA we fused *eyfp* at the 15th residue from its c-terminus. The last 14 amino acids of the *ctra* gene define its degradation tag that is recognized by ClpXP at specific times in the cell cycle to allow for fast clearance of CtrA and initiation of chromosome replication (Domian et al., 1997). The resulting CtrA-eYFP-14 fusion is driven by an *xylX* promoter and is expressed from a high copy plasmid. **(B)** Averaged integrated signal at the two polar microdomains for PopZ, CckA, ChpT, and CtrA along a normalized cell axis. The normalized averaged integrated signal at the new and old poles are plotted for PAmCherry-PopZ

(*n*=125), CckA-eYFP (*n* =118), ChpT-eYFP (*n* =98), and CtrA-eYFP-14 (*n* =125). **(C)** Quantitation of the proportion of cells in which CtrA-eYFP-14 localized to both cell poles (left), formed a single focus at the stalked pole (middle), or remained diffused (right). Scale bar is 2 µm.

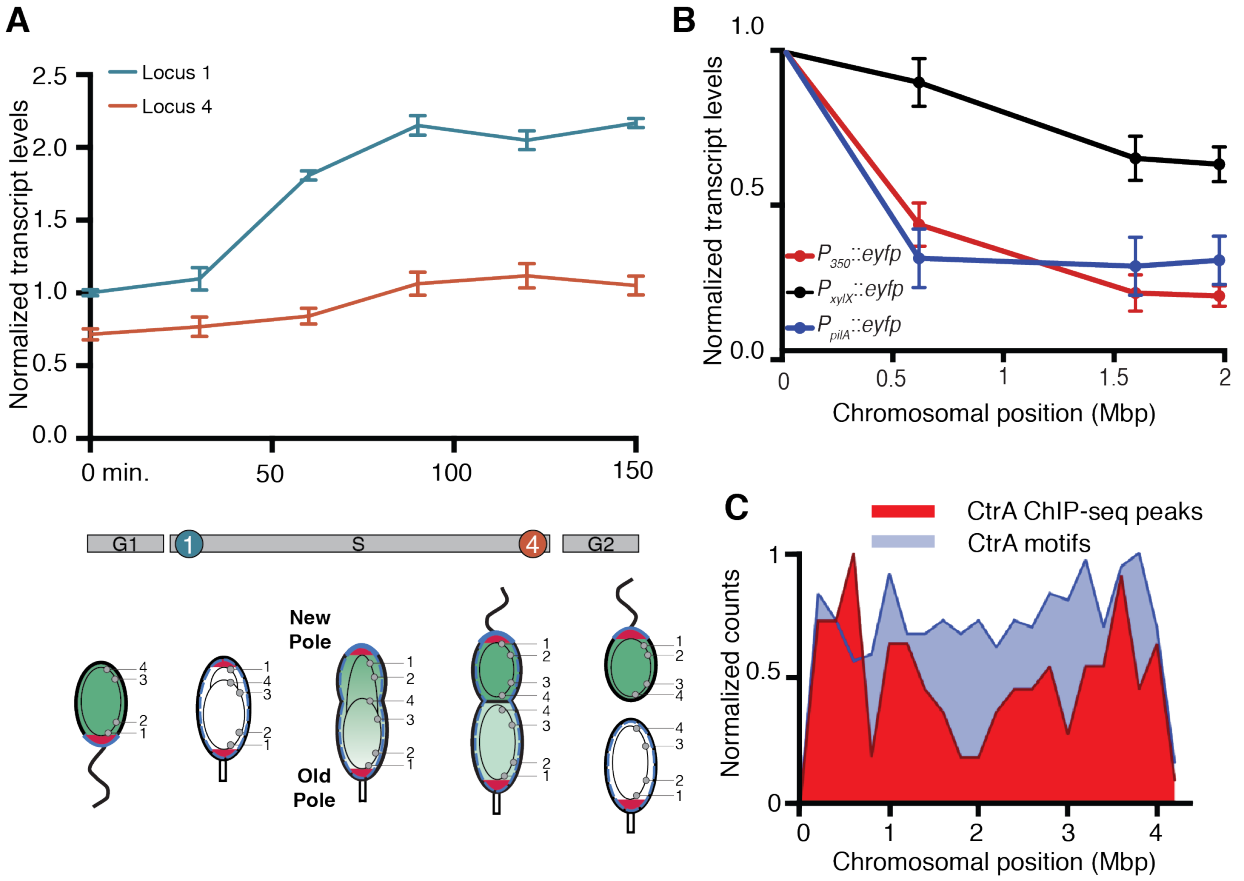

Figure S2. Promoter activity at loci 1-4, related to Figure 2.

(A) Integration of P_{xylX}::*eyfp* to chromosomal loci L1 and L4 demonstrates a copy number effect. The *xylX* promoter (P_{xylx}) is transcriptionally repressed by the protein XylR that binds to operator sites in the absence of xylose but dissociates from the operator when bound to xylose (Stephens et al., 2007). Thus, gene expression from the P_{xylX} promoter in the presence of the xylose inducer is

not dependent on transcription factor availability. Cell cycle time resolved qPCR of mRNA from an *eyfp* gene under the control of the *xylX* promoter is shown for integration at chromosomal loci L1 (blue) and L4 (red). Transcript levels were assayed every 30 minutes during the 150-minutes cell cycle. Replication time of loci L1 and L4 is shown below the qPCR time points. In addition, a cell cycle schematic illustrating the two chromosomal integration loci as well as the progression of DNA replication and segregation is shown. The chromosome is represented by black ovals and theta structures within each cell. The red areas of the cell poles indicate the PopZ microdomain and the green tone indicates CtrA-P levels. **(B)** Integration of P_{pilA}::*eyfp* to chromosomal loci 1-4 demonstrates a gradient of CtrA activity. *eyfp* mRNA levels driven by the *pilA* promoter were measured in synchronized predivisional cells at loci 1-4 (blue). *eyfp* mRNA driven by the *xylX* promoter (black) and by the *350* promoter (red) in synchronized predivisional cells are shown for comparison. Differences between the spatial expression profiles of P_{350}::*efyp* and P_{pilA}::*efyp* are due to differences in promoter regulation. The *350* promoter is regulated exclusively by CtrA and its activity peaks at the 90 minute time point (Zhou et al., 2015) while the *pilA* promoter is activated by CtrA and inhibited by MucR (Fumeaux et al., 2014; Skerker and Shapiro, 2000) and its activity peaks in G1 (~120 minute time point). (**C**) Cumulative occurrences of CtrA qChIP peaks *versus* CtrA binding motifs. Cumulated signal of CtrA binding to the chromosome as measured by quantitative chromatin immunoprecipitation assays (qChIP) using antibody to CtrA (Fumeaux et al., 2014) is shown in red. Cumulative occurrences of CtrA binding motifs on the chromosome, as calculated using the MEME suite (Bailey et al., 2009), is shown in blue. Despite uniform distribution of CtrA binding motifs across the chromosome, CtrA distribution on the chromosome, as captured by qChIP, is not uniform and exhibits a larger concentration of CtrA molecules in the origin-proximal region (0-0.5 and 3.5-4 Mbp).

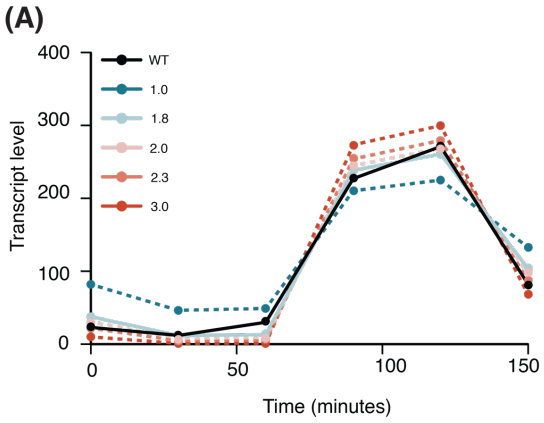

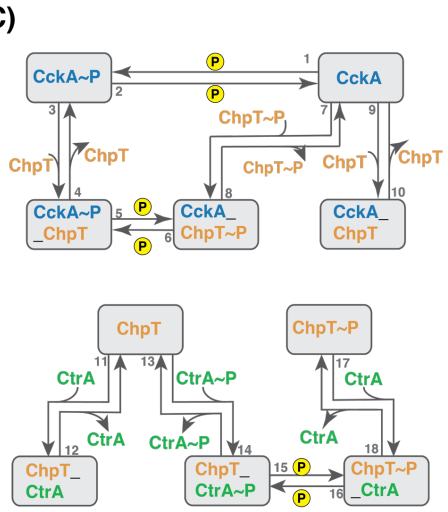

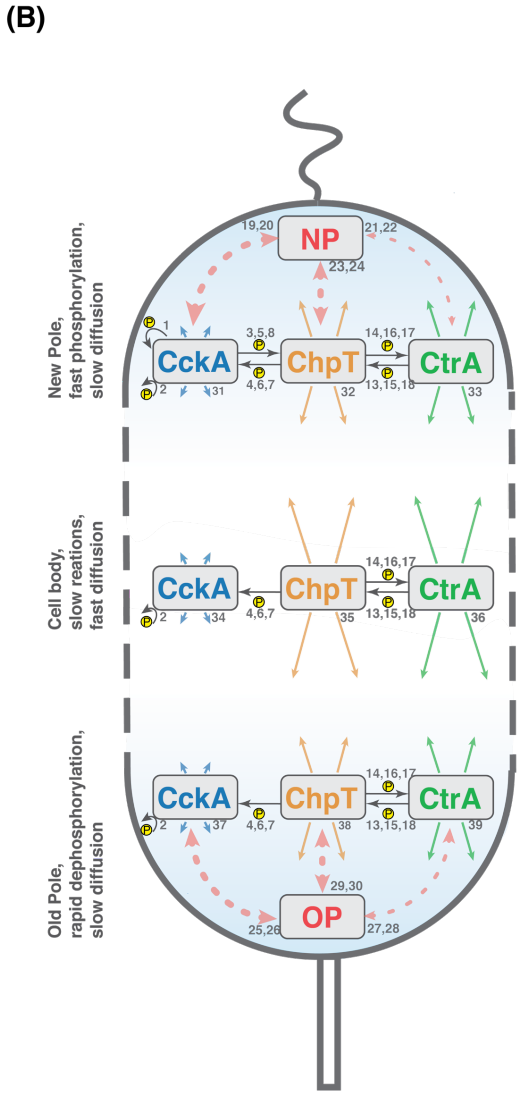

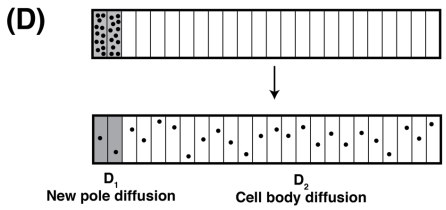

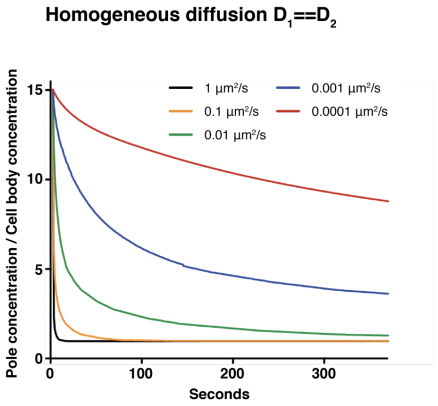

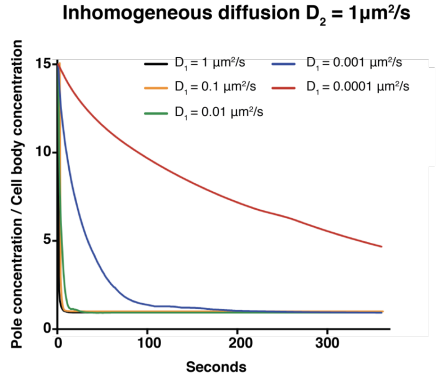

Figure S3. Reaction-diffusion model of CtrA activation, related to Figure 3.

(A) RNA-seq measuring the amount of *ccna_350* mRNA at six times over the cell cycle (Schrader et al., 2016) are shown in black. Modeled steady-state amounts of *ccna_350* mRNA at six times over the cell cycle using Equation S6 are shown in colors. All parameters were fixed (Table S6) except for Hill coefficient which ranged from 1 to 3 (blue to red, dashed lines). For the six time points, CtrA~P levels were set to 0.125, 0.025, 0.05, 0.4, 0.5, and 0.4 of total of CtrA molecules as determined by pulse chase experiments (Jacobs et al., 2003). The solution that best matched the RNA-seq data had a Hill coefficient 1.8 (blue, solid line). **(B)** A simplified schematic of the reactions and diffusion events used in our CtrA activation model. Dotted red arrows indicate CckA, ChpT, and CckA binding to either the new pole (NP) or the old pole (OP) species. The width of the arrow represents the strength of binding, with thicker arrows for tighter binding. The colored edges out of CckA (blue), ChpT (orange), and CtrA (green) boxes indicate diffusion inside the pole and in the body of the cell. The length of the arrow represents the rate of diffusion, with shorter arrows representing slower diffusion. Phosphotransfer reactions are shown in black. Each arrow is labeled with a reaction number from 1 to 39. Information on each reaction is found in Table S6. **(C)** A complete schematic of the phosphotransfer reactions including binding and transfer events. Reaction numbers match the simplified schematic in B. **(D)** Inhomogeneous diffusion is not sufficient for polar accumulation. At the beginning of the simulation all particles localized to the new pole. During the simulation particles diffuse. Ratio between the concentration of particles at the pole and the concentration of particles away from the pole is calculated at each time point. In the homogenous diffusion case (upper graph), the system quickly reached homogenous distribution (ratio equals to 1) matching theoretical results. When the diffusion was

slowed down specifically at the pole, while kept at 1 $\mu m^2/s$ away from the pole, the steady-state distribution remained homogenous and the diffusion away from the pole dominated the kinetics.

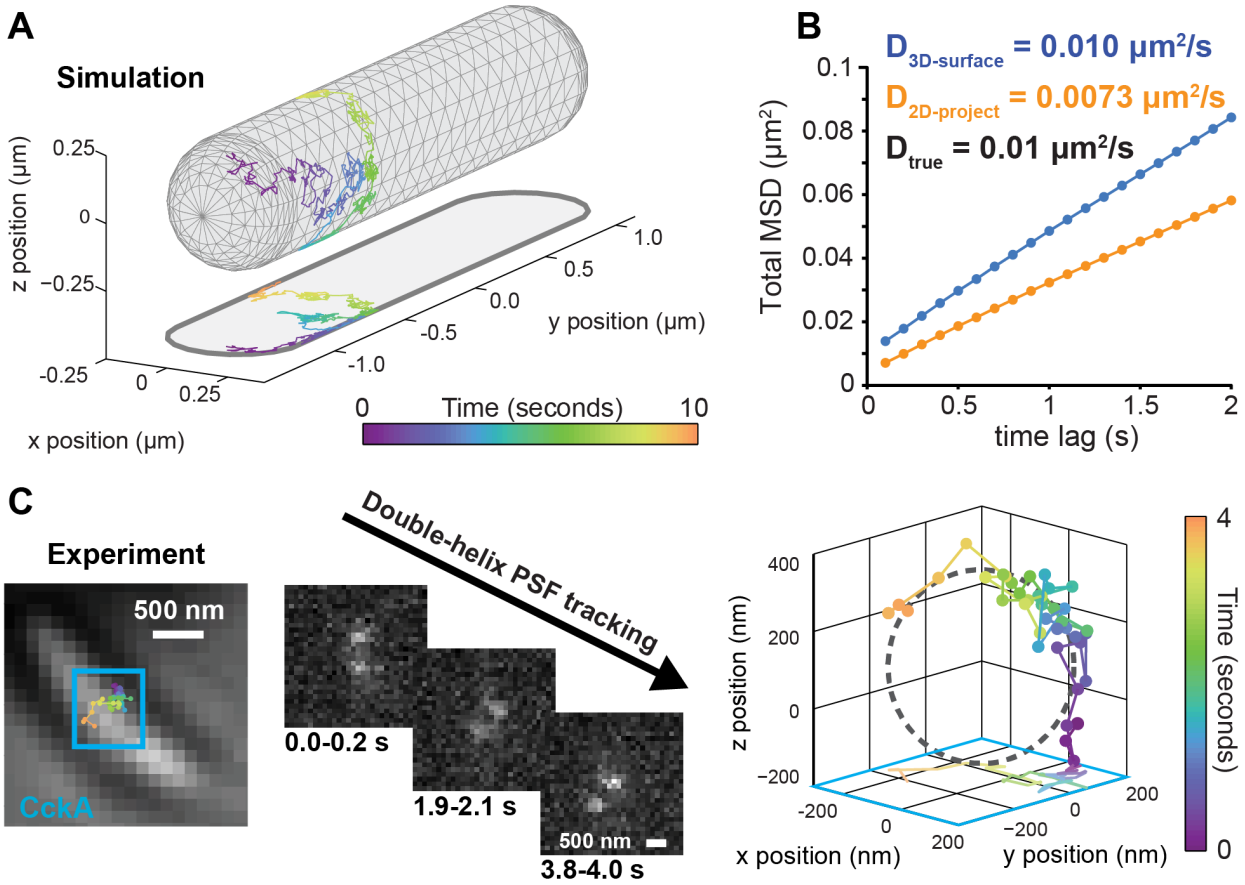

Figure S4. 3D localization of CckA-eYFP motion and concentration on the membrane, related to Figure 4.

(**A**) A simulated trajectory of a membrane-associated protein at high time resolution and without error. Free Brownian motion was simulated on the surface of a 2 μm cylinder with hemispherical caps, radius 250 nm. The 2D projection erroneously implies slower diffusion for parts of the trajectory inside the pole or at the "side" of the cell, as motion of the true 3D trajectory in the *z* axis is lost. (**B**) Mean-squared-displacement analysis including motion blur and localization error demonstrates that 3D measurements accurately measure diffusion, while 2D projection induces systematic errors. Extracting D from the 3D data yielded the correct value of D with <2% systematic error (standard deviation of 5 realizations). Analyzing 2D components of the motion alone ($D_{2D\text{-}project}$) resulted in 27% error in the diffusion estimate. (**C**) The experimental application of 3D tracking using the DH-PSF. Left, 4 second CckA-eYFP trajectory overlaid on brightfield image of a *Caulobacter* cell. Middle, the motion in the double-helix PSF is used to detect 2D and 3D motion. The DH-PSF produced from the diffusing CckA-eYFP molecule first rotates clockwise, corresponding to motion in *z*, then translates, indicating motion in *xy*. Right, the corresponding 3D trajectory sampled with 100 ms frames viewed down the cellular axis clearly exhibits motion along the circumference of the cell, as indicated by the 500 nm diameter dashed circle. (**D**) Single-molecule distributions of CckA and PopZ localizations averaged from old poles (N = 29 poles) and new poles (N = 13) of predivisional cells. The data for old poles is the same as Figure 4C, but not limited to a 200 nm thickness. Blue arrows show the measured diameters of CckA. (**E**) Projection of all single-molecule localizations of CckA and PopZ in the new pole, shown facing down the cell axis (531 and 477 localizations, respectively). Top and right: 1D histogram of CckA and PopZ with 25 nm bins. The approximate full widths at half maximum

(FWHM) are calculated for CckA from the standard deviations of molecule positions along the Y and Z axes, with magnitudes shown by blue arrows.

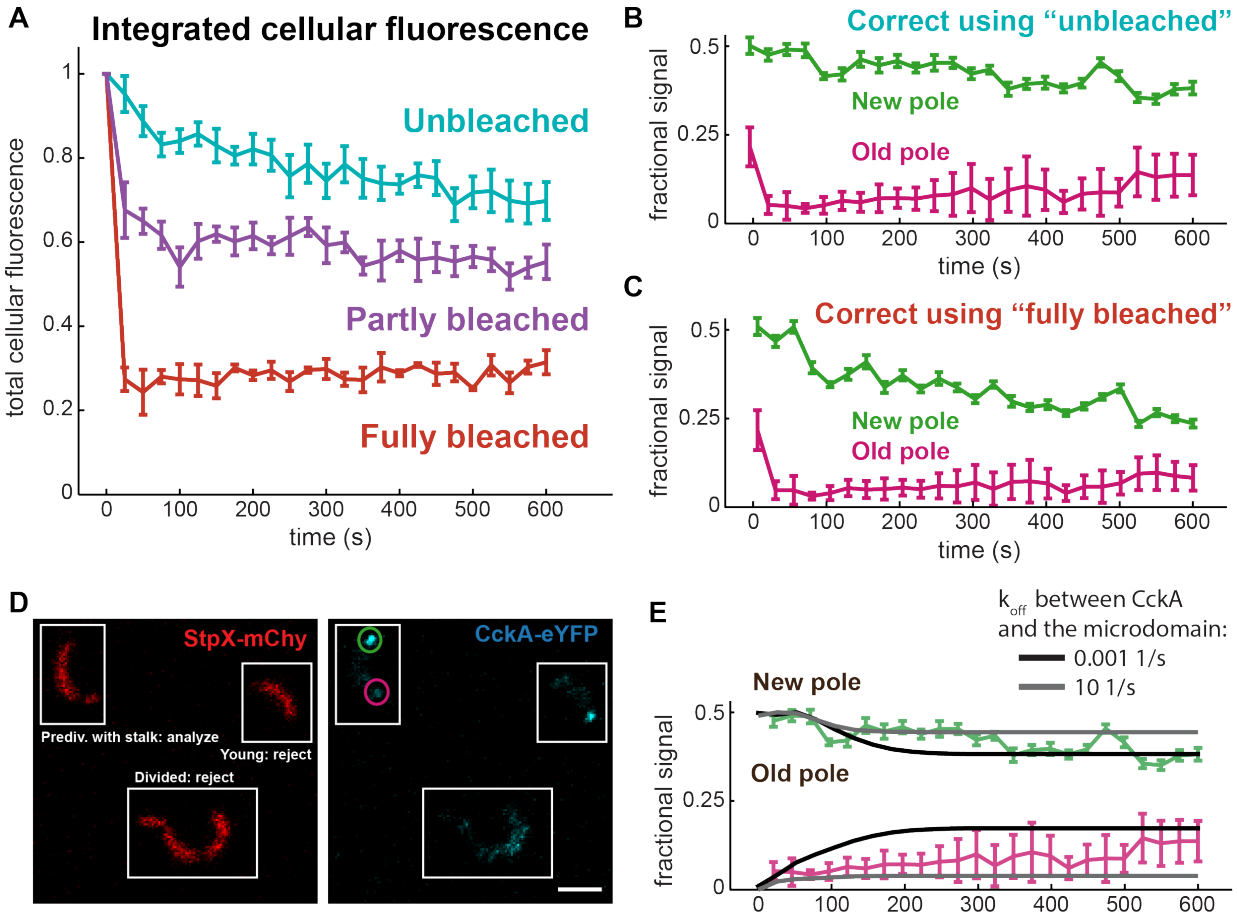

Figure S5. eYFP exhibits slight photorecovery in bleaching experiments, related to Figure 4.

(**A**) *Caulobacter* cells expressing CckA-eYFP were imaged for many frames of laser scanning confocal microscopy following targeted photobleaching with high-intensity 514 nm laser light. Cells that were not targeted exhibit steady loss in total cellular fluorescence due to photobleaching during imaging (N = 9, cyan). Cells that were uniformly bleached with the photobleaching laser exhibited an immediate 75% loss in fluorescence followed by slow, partial overall recovery over

the course of following imaging cycles (N = 3, red). Cells with bleached old poles exhibited intermediate behavior, with slow photobleaching over the course of imaging (N = 6, magenta). (**B**) The data shown in Figure 4 if corrected using a correction factor from "unbleached" cells. (**C**) The data shown in Figure 4 if corrected using a correction factor from "completely bleached" cells. In each case, new poles exhibit loss and old poles exhibit recovery. Errorbars: 95% confidence intervals, i.e. the standard error of the mean x 1.96. (**D**) Example images of cells showing how the StpX-mChy marker was used to identify stalks and discriminate predivisional cells from young cells (low length, monopolar CckA) and from compartmentalized cells (septation visible in the cytoplasmic StpX-mChy fraction). The circles in the CckA-eYFP channel indicate the new (green) and old (red-violet) poles, as defined by the stalk visible in the StpX-mChy channel Scale bar: 2 μm. **(E)** Reaction-diffusion simulations of CckA motion with fast and slow binding to the microdomain. Simulated FRAP experiments were started from steady state distribution (Figure 6A). The population of CckA molecules at the old pole was then "bleached" by marking the molecules as dark CckA molecules. The simulation then continued for 600 seconds and the motion of the "unbleached" CckA molecules was recorded. We show CckA motion in when tightly bound to the microdomains (k_{off} = 0.001, black) and when weakly bound to the microdomains (k_{off} = 10, gray).

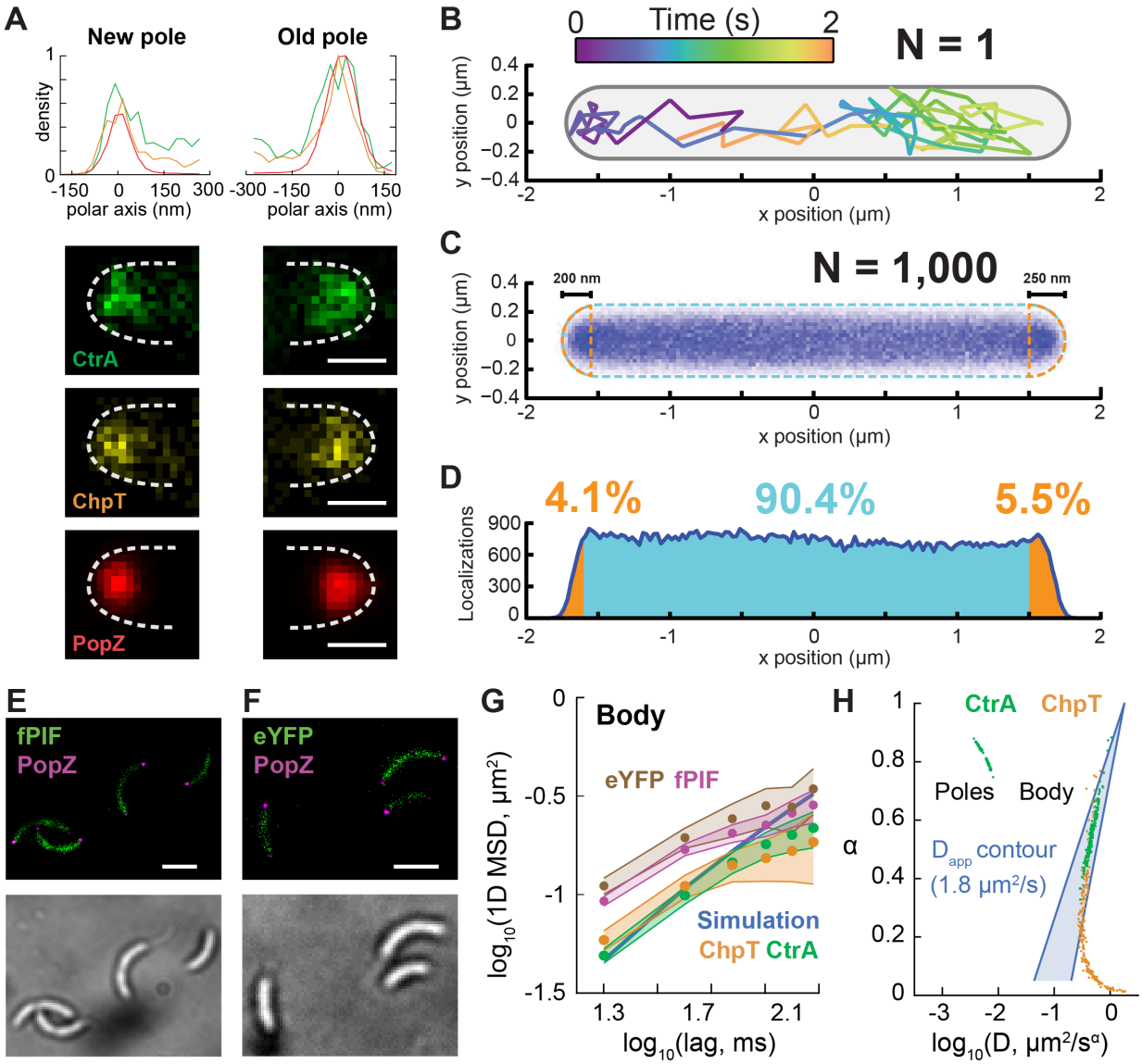

Figure S6. Selective polar permeability and motion of cytoplasmic proteins, related to Figure 5.

(**A**) The 1D profiles and 2D histograms (25 nm bin size) of localizations averaged from many cells. See Figure 5 for details. (**B-D**) Simulations of freely diffusing cytoplasmic molecules with a homogeneous diffusion coefficient D = 1.8 μm^2/s are observed in the poles even in the presence of motion blur and localization error. Motion was simulated in 3D within a 3 μm long cylinder with 250 nm hemispherical caps and absorbing (nonreflective) walls. A step size of 0.5 ms was

used, and to match experimental conditions, trajectories were reconstructed at 20 ms sampling rate (mimicking motion blur) and 40 nm localization error. (**B**) The XY components of a single 3D trajectory, corresponding to localizations of a single freely-diffusing molecule. (**C**) The histogram of localizations from 1,000 simulated 2-second trajectories exhibits high density throughout the cell regardless of motion blur and error, clearly appearing within the poles of the cell. For this analysis, the new and old poles were defined as the regions 200 and 250 nm away from the tip, respectively, consistent with the size of the polar regions used to define tracks in experimental data of Figure 5. (**D**) 1D profile of histogram shown in (**C**). Approximately 4.1% and 5.5% of localizations would be expected to appear within the new and old poles (orange), respectively, if molecular motion were unobstructed. (**E**) White light image and 2D histogram (40 nm bin size) of fPIF-eYFP and PAmCherry-PopZ single-molecule localizations. (**F**) White light image and 2D histogram (40 nm bin size) of eYFP and PAmCherry-PopZ single-molecule localizations. (**G**) 1D MSD values in the body of predivisional *Caulobacter* cells as shown in Figure 5F, including eYFP and fPIF. 95% CI shown. (**H**) Fitting the MSD data to an equation for anomalous diffusion was not able to precisely specify D and α due to the short track durations available. Points: fits values of D and α generated from 200 resamples of CtrA and ChpT tracks either from the cell body or from the poles. Blue lines mark combinations of D and α that would yield apparent diffusion coefficients D_{app} for a certain short-time approximation, calculated as $D_{app} = D\tau^{1-\alpha}$ for $D_{app} =$ 1.8 μm^2/s and τ = 20 ms (the frame integration time, right line) or τ = 100 ms (the maximum time included in the fit, left line). The trajectories measured are consistent with a short-time value of $D_{app} = 1.8$ μm^2/s and suggest that $\alpha < 0.7$. In contrast, diffusion within the poles appeared relatively Brownian, with $0.75 \leq \alpha \leq 0.9$. The MSD curve of ChpT at the poles cannot be accurately fit due to confinement effects (see Figure 5 and discussion above).

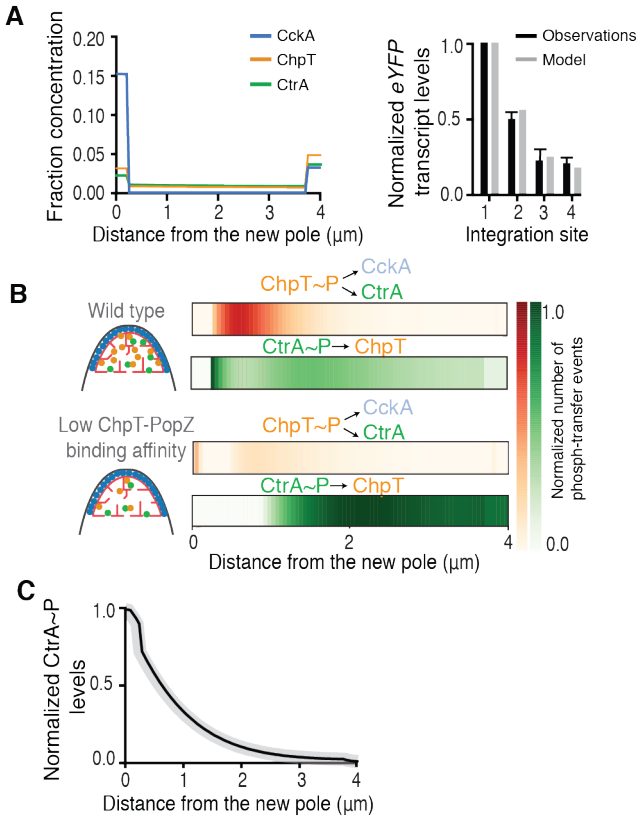

Figure S7. Further consequences of CckA, ChpT, and CtrA concentration within the PopZ microdomain, related to Figure 6.

(A) Protein distribution and *eyfp* mRNA levels based on our reaction-diffusion model of CtrA activation. (Left) Steady state protein concentrations for CckA (blue), ChpT (orange), and CtrA (green) as a function of distance from the new pole. (Right) Steady state relative amounts of *eyfp* mRNA production driven by the *350* promoter in predivisional cells from the four integration regions (gray). The calculated *eyfp* mRNA values recapitulated the measured *eyfp* mRNA levels (black). **(B)** Spatial distribution of phosphotransfer events where proteins lose phosphate (ChpT~P to CckA or CtrA, and CtrA~P to ChpT). Data plotted as relative number of phospho-transfer events at steady state. The phospho-transfer events occur away from the new pole microdomain in a

simulation using our measured parameters (upper phospho-graph). Most ChpT~P transfers to either CckA or CtrA occur close to the new pole microdomain, enhancing the gradient in CtrA~P distribution. However, in our *in silico* mutant with weak binding between ChpT and the PopZ microdomain, back phospho-transfer events are dispersed across the cell (lower phospho-graph). **(C)** CckA accumulation at the old pole does not affect CtrA~P distribution. The averaged steady-state profile of CtrA~P along the long axis of the cell is shown in black and fluctuation in the profile due to changes in CckA accumulation at the old pole are highlighted in gray. Modulation of CckA accumulation at the old pole was achieved by changing the k_{on} binding rate between CckA and the old pole microdomain. All other parameters remain constant.

REFERENCES

Abel, S., Bucher, T., Nicollier, M., Hug, I., Kaever, V., Abel Zur Wiesch, P., and Jenal, U. (2013). Bi-modal distribution of the second messenger c-di-GMP controls cell fate and asymmetry during the caulobacter cell cycle. PLoS Genet *9*, e1003744.

Alberti, S. (2017). The wisdom of crowds: regulating cell function through condensed states of living matter. J Cell Sci *130*, 2789-2796.

Ardissone, S., and Viollier, P.H. (2015). Interplay between flagellation and cell cycle control in Caulobacter. Curr Opin Microbiol *28*, 83-92.

Ash, K., Brown, T., Watford, T., Scott, L.E., Stephens, C., and Ely, B. (2014). A comparison of the Caulobacter NA1000 and K31 genomes reveals extensive genome rearrangements and differences in metabolic potential. Open Biol *4*.

Atay, O., and Skotheim, J.M. (2017). Spatial and temporal signal processing and decision making by MAPK pathways. J Cell Biol *216*, 317-330.

Backlund, M.P., Joyner, R., and Moerner, W.E. (2015). Chromosomal locus tracking with proper accounting of static and dynamic errors. Phys Rev E Stat Nonlin Soft Matter Phys *91*, 062716.

Bailey, T.L., Boden, M., Buske, F.A., Frith, M., Grant, C.E., Clementi, L., Ren, J., Li, W.W., and Noble, W.S. (2009). MEME SUITE: tools for motif discovery and searching. Nucleic Acids Res *37*, W202-208.

Banani, S.F., Lee, H.O., Hyman, A.A., and Rosen, M.K. (2017). Biomolecular condensates: organizers of cellular biochemistry. Nat Rev Mol Cell Biol *18*, 285-298.

Barkai, N., and Shilo, B.Z. (2009). Robust generation and decoding of morphogen gradients. Cold Spring Harb Perspect Biol *1*, a001990.

Ben-Yehuda, S., Rudner, D.Z., and Losick, R. (2003). RacA, a bacterial protein that anchors chromosomes to the cell poles. Science *299*, 532-536.

Berge, M., Campagne, S., Mignolet, J., Holden, S., Theraulaz, L., Manley, S., Allain, F.H., and Viollier, P.H. (2016). Modularity and determinants of a (bi-)polarization control system from free-living and obligate intracellular bacteria. Elife *5*.

Berge, M., and Viollier, P.H. (2017). End-in-Sight: Cell Polarization by the Polygamic Organizer PopZ. Trends Microbiol *111*, 1.

Bhattacharyya, R.P., Remenyi, A., Good, M.C., Bashor, C.J., Falick, A.M., and Lim, W.A. (2006). The Ste5 scaffold allosterically modulates signaling output of the yeast mating pathway. Science *311*, 822-826.

Biondi, E.G., Reisinger, S.J., Skerker, J.M., Arif, M., Perchuk, B.S., Ryan, K.R., and Laub, M.T. (2006). Regulation of the bacterial cell cycle by an integrated genetic circuit. Nature *444*, 899-904.

Blair, J.A., Xu, Q., Childers, W.S., Mathews, II, Kern, J.W., Eckart, M., Deacon, A.M., and Shapiro, L. (2013). Branched signal wiring of an essential bacterial cell-cycle phosphotransfer protein. Structure *21*, 1590-1601.

Bos, M.P., Robert, V., and Tommassen, J. (2007). Biogenesis of the gram-negative bacterial outer membrane. Annu Rev Microbiol *61*, 191-214.

Bowman, G.R., Comolli, L.R., Gaietta, G.M., Fero, M., Hong, S.H., Jones, Y., Lee, J.H., Downing, K.H., Ellisman, M.H., McAdams, H.H.*, et al.* (2010). Caulobacter PopZ forms a polar subdomain dictating sequential changes in pole composition and function. Mol Microbiol *76*, 173-189.

Bowman, G.R., Comolli, L.R., Zhu, J., Eckart, M., Koenig, M., Downing, K.H., Moerner, W.E., Earnest, T., and Shapiro, L. (2008). A polymeric protein anchors the chromosomal origin/ParB complex at a bacterial cell pole. Cell *134*, 945-955.

Bowman, G.R., Perez, A.M., Ptacin, J.L., Ighodaro, E., Folta-Stogniew, E., Comolli, L.R., and Shapiro, L. (2013). Oligomerization and higher-order assembly contribute to sub-cellular localization of a bacterial scaffold. Mol Microbiol *90*, 776-795.

Brassinga, A.K., and Marczynski, G.T. (2001). Replication intermediate analysis confirms that chromosomal replication origin initiates from an unusual intergenic region in Caulobacter crescentus. Nucleic Acids Res *29*, 4441-4451.

Brown, G.C., and Kholodenko, B.N. (1999). Spatial gradients of cellular phospho-proteins. FEBS Lett *457*, 452-454.

Chen, Y.E., Tropini, C., Jonas, K., Tsokos, C.G., Huang, K.C., and Laub, M.T. (2011). Spatial gradient of protein phosphorylation underlies replicative asymmetry in a bacterium. Proc Natl Acad Sci U S A *108*, 1052-1057.

Chen, Y.E., Tsokos, C.G., Biondi, E.G., Perchuk, B.S., and Laub, M.T. (2009). Dynamics of two Phosphorelays controlling cell cycle progression in Caulobacter crescentus. J Bacteriol *191*, 7417-7429.

Childers, W.S., Xu, Q., Mann, T.H., Mathews, II, Blair, J.A., Deacon, A.M., and Shapiro, L. (2014). Cell fate regulation governed by a repurposed bacterial histidine kinase. PLoS Biol *12*, e1001979.

Chong, P.A., and Forman-Kay, J.D. (2016). Liquid-liquid phase separation in cellular signaling systems. Curr Opin Struct Biol *41*, 180-186.

Coquel, A.S., Jacob, J.P., Primet, M., Demarez, A., Dimiccoli, M., Julou, T., Moisan, L., Lindner, A.B., and Berry, H. (2013). Localization of protein aggregation in Escherichia coli is governed by diffusion and nucleoid macromolecular crowding effect. PLoS Comput Biol *9*, e1003038.

DeWire, S.M., Ahn, S., Lefkowitz, R.J., and Shenoy, S.K. (2007). Beta-arrestins and cell signaling. Annu Rev Physiol *69*, 483-510.

Dingwall, A., and Shapiro, L. (1989). Rate, origin, and bidirectionality of Caulobacter chromosome replication as determined by pulsed-field gel electrophoresis. Proc Natl Acad Sci U S A *86*, 119-123.

Domian, I.J., Quon, K.C., and Shapiro, L. (1997). Cell type-specific phosphorylation and proteolysis of a transcriptional regulator controls the G1-to-S transition in a bacterial cell cycle. Cell *90*, 415-424.

Dubey, B.N., Lori, C., Ozaki, S., Fucile, G., Plaza-Menacho, I., Jenal, U., and Schirmer, T. (2016). Cyclic di-GMP mediates a histidine kinase/phosphatase switch by noncovalent domain cross-linking. Sci Adv *2*, e1600823.

Eberhard, S., Finazzi, G., and Wollman, F.A. (2008). The dynamics of photosynthesis. Annu Rev Genet *42*, 463-515.

Ebersbach, G., Briegel, A., Jensen, G.J., and Jacobs-Wagner, C. (2008). A self-associating protein critical for chromosome attachment, division, and polar organization in caulobacter. Cell *134*, 956-968.

Elf, J., Li, G.W., and Xie, X.S. (2007). Probing transcription factor dynamics at the single-molecule level in a living cell. Science *316*, 1191-1194.

Ely, B. (1991). Genetics of Caulobacter crescentus. Methods Enzymol *204*, 372-384.

Evinger, M., and Agabian, N. (1977). Envelope-associated nucleoid from Caulobacter crescentus stalked and swarmer cells. J Bacteriol *132*, 294-301.

Fu, G., Tu, L.C., Zilman, A., and Musser, S.M. (2017). Investigating molecular crowding within nuclear pores using polarization-PALM. Elife *6*.

Fujiwara, T.K., Iwasawa, K., Kalay, Z., Tsunoyama, T.A., Watanabe, Y., Umemura, Y.M., Murakoshi, H., Suzuki, K.G., Nemoto, Y.L., Morone, N.*, et al.* (2016). Confined diffusion of transmembrane proteins and lipids induced by the same actin meshwork lining the plasma membrane. Mol Biol Cell *27*, 1101-1119.

Fumeaux, C., Radhakrishnan, S.K., Ardissone, S., Theraulaz, L., Frandi, A., Martins, D., Nesper, J., Abel, S., Jenal, U., and Viollier, P.H. (2014). Cell cycle transition from S-phase to G1 in Caulobacter is mediated by ancestral virulence regulators. Nat Commun *5*, 4081.

Gahlmann, A., Ptacin, J.L., Grover, G., Quirin, S., von Diezmann, A.R., Lee, M.K., Backlund, M.P., Shapiro, L., Piestun, R., and Moerner, W.E. (2013). Quantitative multicolor subdiffraction imaging of bacterial protein ultrastructures in three dimensions. Nano Lett *13*, 987-993.

Gibson, D.G., Young, L., Chuang, R.Y., Venter, J.C., Hutchison, C.A., 3rd, and Smith, H.O. (2009). Enzymatic assembly of DNA molecules up to several hundred kilobases. Nat Methods *6*, 343-345.

Giessen, T.W. (2016). Encapsulins: microbial nanocompartments with applications in biomedicine, nanobiotechnology and materials science. Curr Opin Chem Biol *34*, 1-10.

Good, M., Tang, G., Singleton, J., Remenyi, A., and Lim, W.A. (2009). The Ste5 scaffold directs mating signaling by catalytically unlocking the Fus3 MAP kinase for activation. Cell *136*, 1085-1097.

Good, M.C., Zalatan, J.G., and Lim, W.A. (2011). Scaffold proteins: hubs for controlling the flow of cellular information. Science *332*, 680-686.

Heid, C.A., Stevens, J., Livak, K.J., and Williams, P.M. (1996). Real time quantitative PCR. Genome Res *6*, 986-994.

Hernandez-Vega, A., Braun, M., Scharrel, L., Jahnel, M., Wegmann, S., Hyman, B.T., Alberti, S., Diez, S., and Hyman, A.A. (2017). Local Nucleation of Microtubule Bundles through Tubulin Concentration into a Condensed Tau Phase. Cell Rep *20*, 2304-2312.

Holmes, J.A., Follett, S.E., Wang, H., Meadows, C.P., Varga, K., and Bowman, G.R. (2016). Caulobacter PopZ forms an intrinsically disordered hub in organizing bacterial cell poles. Proc Natl Acad Sci U S A *113*, 12490-12495.

Hong, S.H., Toro, E., Mortensen, K.I., de la Rosa, M.A., Doniach, S., Shapiro, L., Spakowitz, A.J., and McAdams, H.H. (2013). Caulobacter chromosome in vivo configuration matches model predictions for a supercoiled polymer in a cell-like confinement. Proc Natl Acad Sci U S A *110*, 1674-1679.

Iniesta, A.A., Hillson, N.J., and Shapiro, L. (2010a). Cell pole-specific activation of a critical bacterial cell cycle kinase. Proc Natl Acad Sci U S A *107*, 7012-7017.

Iniesta, A.A., Hillson, N.J., and Shapiro, L. (2010b). Polar remodeling and histidine kinase activation, which is essential for Caulobacter cell cycle progression, are dependent on DNA replication initiation. J Bacteriol *192*, 3893-3902.

Iyer-Biswas, S., Wright, C.S., Henry, J.T., Lo, K., Burov, S., Lin, Y., Crooks, G.E., Crosson, S., Dinner, A.R., and Scherer, N.F. (2014). Scaling laws governing stochastic growth and division of single bacterial cells. Proc Natl Acad Sci U S A *111*, 15912-15917.

Jacobs, C., Ausmees, N., Cordwell, S.J., Shapiro, L., and Laub, M.T. (2003). Functions of the CckA histidine kinase in Caulobacter cell cycle control. Mol Microbiol *47*, 1279-1290.

Jacobs, C., Domian, I.J., Maddock, J.R., and Shapiro, L. (1999). Cell cycle-dependent polar localization of an essential bacterial histidine kinase that controls DNA replication and cell division. Cell *97*, 111-120.

Jonas, K., Chen, Y.E., and Laub, M.T. (2011). Modularity of the bacterial cell cycle enables independent spatial and temporal control of DNA replication. Curr Biol *21*, 1092-1101.

Judd, E.M., Ryan, K.R., Moerner, W.E., Shapiro, L., and McAdams, H.H. (2003). Fluorescence bleaching reveals asymmetric compartment formation prior to cell division in Caulobacter. Proc Natl Acad Sci U S A *100*, 8235-8240.

Kalab, P., Weis, K., and Heald, R. (2002). Visualization of a Ran-GTP gradient in interphase and mitotic Xenopus egg extracts. Science *295*, 2452-2456.

Kerfeld, C.A., and Erbilgin, O. (2015). Bacterial microcompartments and the modular construction of microbial metabolism. Trends Microbiol *23*, 22-34.

Kerfeld, C.A., Heinhorst, S., and Cannon, G.C. (2010). Bacterial microcompartments. Annu Rev Microbiol *64*, 391-408.

Kerfeld, C.A., and Melnicki, M.R. (2016). Assembly, function and evolution of cyanobacterial carboxysomes. Curr Opin Plant Biol *31*, 66-75.

Kholodenko, B.N., Hancock, J.F., and Kolch, W. (2010). Signalling ballet in space and time. Nat Rev Mol Cell Biol *11*, 414-426.

Kiekebusch, D., and Thanbichler, M. (2014). Spatiotemporal organization of microbial cells by protein concentration gradients. Trends Microbiol *22*, 65-73.

Knockenhauer, K.E., and Schwartz, T.U. (2016). The Nuclear Pore Complex as a Flexible and Dynamic Gate. Cell *164*, 1162-1171.

Komeili, A., Li, Z., Newman, D.K., and Jensen, G.J. (2006). Magnetosomes are cell membrane invaginations organized by the actin-like protein MamK. Science *311*, 242-245.

Kozdon, J.B., Melfi, M.D., Luong, K., Clark, T.A., Boitano, M., Wang, S., Zhou, B., Gonzalez, D., Collier, J., Turner, S.W.*, et al.* (2013). Global methylation state at base-pair resolution of the Caulobacter genome throughout the cell cycle. Proc Natl Acad Sci U S A *110*, E4658-4667.

Kumar, M., Mommer, M.S., and Sourjik, V. (2010). Mobility of cytoplasmic, membrane, and DNA-binding proteins in Escherichia coli. Biophys J *98*, 552-559.

Kusumi, A., Sako, Y., and Yamamoto, M. (1993). Confined lateral diffusion of membrane receptors as studied by single particle tracking (nanovid microscopy). Effects of calcium-induced differentiation in cultured epithelial cells. Biophys J *65*, 2021-2040.

Laloux, G., and Jacobs-Wagner, C. (2013). Spatiotemporal control of PopZ localization through cell cycle-coupled multimerization. J Cell Biol *201*, 827-841.

Lam, H., Matroule, J.Y., and Jacobs-Wagner, C. (2003). The asymmetric spatial distribution of bacterial signal transduction proteins coordinates cell cycle events. Dev Cell *5*, 149-159.

Lasker, K., Mann, T.H., and Shapiro, L. (2016). An intracellular compass spatially coordinates cell cycle modules in Caulobacter crescentus. Curr Opin Microbiol *33*, 131-139.

Laub, M.T., Chen, S.L., Shapiro, L., and McAdams, H.H. (2002). Genes directly controlled by CtrA, a master regulator of the Caulobacter cell cycle. Proc Natl Acad Sci U S A *99*, 4632-4637.

Laub, M.T., McAdams, H.H., Feldblyum, T., Fraser, C.M., and Shapiro, L. (2000). Global analysis of the genetic network controlling a bacterial cell cycle. Science *290*, 2144-2148.

Le, T.B., Imakaev, M.V., Mirny, L.A., and Laub, M.T. (2013). High-resolution mapping of the spatial organization of a bacterial chromosome. Science *342*, 731-734.

Lenarcic, R., Halbedel, S., Visser, L., Shaw, M., Wu, L.J., Errington, J., Marenduzzo, D., and Hamoen, L.W. (2009). Localisation of DivIVA by targeting to negatively curved membranes. EMBO J *28*, 2272-2282.

Levskaya, A., Weiner, O.D., Lim, W.A., and Voigt, C.A. (2009). Spatiotemporal control of cell signalling using a light-switchable protein interaction. Nature *461*, 997-1001.

Lew, M.D., von Diezmann, A.R., and Moerner, W.E. (2013). Easy-DHPSF open-source software for three-dimensional localization of single molecules with precision beyond the optical diffraction limit. Protoc exch *2013*.

Li, G.W., Burkhardt, D., Gross, C., and Weissman, J.S. (2014). Quantifying absolute protein synthesis rates reveals principles underlying allocation of cellular resources. Cell *157*, 624-635.

Li, P., Banjade, S., Cheng, H.C., Kim, S., Chen, B., Guo, L., Llaguno, M., Hollingsworth, J.V., King, D.S., Banani, S.F*., et al.* (2012). Phase transitions in the assembly of multivalent signalling proteins. Nature *483*, 336-340.

Lin, L., Osorio Valeriano, M., Harms, A., Sogaard-Andersen, L., and Thanbichler, M. (2017). Bactofilin-mediated organization of the ParABS chromosome segregation system in Myxococcus xanthus. Nat Commun *8*, 1817.

Lori, C., Ozaki, S., Steiner, S., Bohm, R., Abel, S., Dubey, B.N., Schirmer, T., Hiller, S., and Jenal, U. (2015). Cyclic di-GMP acts as a cell cycle oscillator to drive chromosome replication. Nature *523*, 236-239.

Maeder, C.I., Hink, M.A., Kinkhabwala, A., Mayr, R., Bastiaens, P.I., and Knop, M. (2007). Spatial regulation of Fus3 MAP kinase activity through a reaction-diffusion mechanism in yeast pheromone signalling. Nat Cell Biol *9*, 1319-1326.

Mann, T.H., Seth Childers, W., Blair, J.A., Eckart, M.R., and Shapiro, L. (2016). A cell cycle kinase with tandem sensory PAS domains integrates cell fate cues. Nat Commun *7*, 11454.

Mao, Y.S., Zhang, B., and Spector, D.L. (2011). Biogenesis and function of nuclear bodies. Trends Genet *27*, 295-306.

McAdams, H.H., and Shapiro, L. (2009). System-level design of bacterial cell cycle control. FEBS Lett *583*, 3984-3991.

Meldi, L., and Brickner, J.H. (2011). Compartmentalization of the nucleus. Trends Cell Biol *21*, 701-708.

Mignolet, J., Holden, S., Berge, M., Panis, G., Eroglu, E., Theraulaz, L., Manley, S., and Viollier, P.H. (2016). Functional dichotomy and distinct nanoscale assemblies of a cell cycle-controlled bipolar zinc-finger regulator. Elife *5*.

Misteli, T. (2007). Beyond the sequence: cellular organization of genome function. Cell *128*, 787-800.

Molliex, A., Temirov, J., Lee, J., Coughlin, M., Kanagaraj, A.P., Kim, H.J., Mittag, T., and Taylor, J.P. (2015). Phase separation by low complexity domains promotes stress granule assembly and drives pathological fibrillization. Cell *163*, 123-133.

Moseley, J.B., Mayeux, A., Paoletti, A., and Nurse, P. (2009). A spatial gradient coordinates cell size and mitotic entry in fission yeast. Nature *459*, 857-860.

Nelder, J.A., and Mead, R. (1965). A Simplex Method for Function Minimization. The Computer Journal *7*, 308-313.

Nevo, R., Charuvi, D., Shimoni, E., Schwarz, R., Kaplan, A., Ohad, I., and Reich, Z. (2007). Thylakoid membrane perforations and connectivity enable intracellular traffic in cyanobacteria. EMBO J *26*, 1467-1473.

Nott, T.J., Craggs, T.D., and Baldwin, A.J. (2016). Membraneless organelles can melt nucleic acid duplexes and act as biomolecular filters. Nat Chem *8*, 569-575.

Nott, T.J., Petsalaki, E., Farber, P., Jervis, D., Fussner, E., Plochowietz, A., Craggs, T.D., Bazett-Jones, D.P., Pawson, T., Forman-Kay, J.D.*, et al.* (2015). Phase transition of a disordered nuage protein generates environmentally responsive membraneless organelles. Mol Cell *57*, 936-947.

Nunnari, J., and Suomalainen, A. (2012). Mitochondria: in sickness and in health. Cell *148*, 1145-1159.

Ovesny, M., Krizek, P., Borkovec, J., Svindrych, Z., and Hagen, G.M. (2014). ThunderSTORM: a comprehensive ImageJ plug-in for PALM and STORM data analysis and super-resolution imaging. Bioinformatics *30*, 2389-2390.

Perez, A.M., Mann, T.H., Lasker, K., Ahrens, D.G., Eckart, M.R., and Shapiro, L. (2017). A Localized Complex of Two Protein Oligomers Controls the Orientation of Cell Polarity. MBio *8*.

Pfaffl, M.W. (2001). A new mathematical model for relative quantification in real-time RT-PCR. Nucleic Acids Res *29*, e45.

Poindexter, J.S. (1964). Biological Properties and Classification of the Caulobacter Group. Bacteriol Rev *28*, 231-295.

Ptacin, J.L., Gahlmann, A., Bowman, G.R., Perez, A.M., von Diezmann, A.R., Eckart, M.R., Moerner, W.E., and Shapiro, L. (2014). Bacterial scaffold directs pole-specific centromere segregation. Proc Natl Acad Sci U S A *111*, E2046-2055.

Ptacin, J.L., and Shapiro, L. (2013). Chromosome architecture is a key element of bacterial cellular organization. Cell Microbiol *15*, 45-52.

Quon, K.C., Marczynski, G.T., and Shapiro, L. (1996). Cell cycle control by an essential bacterial two-component signal transduction protein. Cell *84*, 83-93.

Quon, K.C., Yang, B., Domian, I.J., Shapiro, L., and Marczynski, G.T. (1998). Negative control of bacterial DNA replication by a cell cycle regulatory protein that binds at the chromosome origin. Proc Natl Acad Sci U S A *95*, 120-125.

Ramamurthi, K.S., and Losick, R. (2009). Negative membrane curvature as a cue for subcellular localization of a bacterial protein. Proc Natl Acad Sci U S A *106*, 13541-13545.

Reisenauer, A., Quon, K., and Shapiro, L. (1999). The CtrA response regulator mediates temporal control of gene expression during the Caulobacter cell cycle. J Bacteriol *181*, 2430-2439.

Reisenauer, A., and Shapiro, L. (2002). DNA methylation affects the cell cycle transcription of the CtrA global regulator in Caulobacter. EMBO J *21*, 4969-4977.

Ritchie, K., Shan, X.Y., Kondo, J., Iwasawa, K., Fujiwara, T., and Kusumi, A. (2005). Detection of non-Brownian diffusion in the cell membrane in single molecule tracking. Biophys J *88*, 2266-2277.

Rudner, D.Z., and Losick, R. (2010). Protein subcellular localization in bacteria. Cold Spring Harb Perspect Biol *2*, a000307.

Ryan, K.R., Huntwork, S., and Shapiro, L. (2004). Recruitment of a cytoplasmic response regulator to the cell pole is linked to its cell cycle-regulated proteolysis. Proc Natl Acad Sci U S A *101*, 7415-7420.

Savin, T., and Doyle, P.S. (2005). Static and dynamic errors in particle tracking microrheology. Biophys J *88*, 623-638.

Schmidt, H.B., and Gorlich, D. (2016). Transport Selectivity of Nuclear Pores, Phase Separation, and Membraneless Organelles. Trends Biochem Sci *41*, 46-61.

Schmittgen, T.D., and Livak, K.J. (2008). Analyzing real-time PCR data by the comparative C(T) method. Nat Protoc *3*, 1101-1108.

Schrader, J.M., Li, G.W., Childers, W.S., Perez, A.M., Weissman, J.S., Shapiro, L., and McAdams, H.H. (2016). Dynamic translation regulation in Caulobacter cell cycle control. Proc Natl Acad Sci U S A *113*, E6859-E6867.

Shapiro, L., McAdams, H.H., and Losick, R. (2009). Why and how bacteria localize proteins. Science *326*, 1225-1228.

Shin, Y., and Brangwynne, C.P. (2017). Liquid phase condensation in cell physiology and disease. Science *357*.

Siam, R., and Marczynski, G.T. (2000). Cell cycle regulator phosphorylation stimulates two distinct modes of binding at a chromosome replication origin. EMBO J *19*, 1138-1147.

Skerker, J.M., and Shapiro, L. (2000). Identification and cell cycle control of a novel pilus system in Caulobacter crescentus. EMBO J *19*, 3223-3234.

Slaughter, B.D., Smith, S.E., and Li, R. (2009). Symmetry breaking in the life cycle of the budding yeast. Cold Spring Harb Perspect Biol *1*, a003384.

Stephens, C., Christen, B., Fuchs, T., Sundaram, V., Watanabe, K., and Jenal, U. (2007). Genetic analysis of a novel pathway for D-xylose metabolism in Caulobacter crescentus. J Bacteriol *189*, 2181-2185.

Su, X., Ditlev, J.A., Hui, E., Xing, W., Banjade, S., Okrut, J., King, D.S., Taunton, J., Rosen, M.K., and Vale, R.D. (2016). Phase separation of signaling molecules promotes T cell receptor signal transduction. Science *352*, 595-599.

Thanbichler, M., Iniesta, A.A., and Shapiro, L. (2007). A comprehensive set of plasmids for vanillate- and xylose-inducible gene expression in Caulobacter crescentus. Nucleic Acids Res *35*, e137.

Toro, E., Hong, S.H., McAdams, H.H., and Shapiro, L. (2008). Caulobacter requires a dedicated mechanism to initiate chromosome segregation. Proc Natl Acad Sci U S A *105*, 15435-15440.

Tropini, C., Rabbani, N., and Huang, K.C. (2012). Physical constraints on the establishment of intracellular spatial gradients in bacteria. BMC Biophys *5*, 17.

Tsai, J.W., and Alley, M.R. (2001). Proteolysis of the Caulobacter McpA chemoreceptor is cell cycle regulated by a ClpX-dependent pathway. J Bacteriol *183*, 5001-5007.

Tsokos, C.G., Perchuk, B.S., and Laub, M.T. (2011). A dynamic complex of signaling proteins uses polar localization to regulate cell-fate asymmetry in Caulobacter crescentus. Dev Cell *20*, 329-341.

Umbarger, M.A., Toro, E., Wright, M.A., Porreca, G.J., Bau, D., Hong, S.H., Fero, M.J., Zhu, L.J., Marti-Renom, M.A., McAdams, H.H*., et al.* (2011). The three-dimensional architecture of a bacterial genome and its alteration by genetic perturbation. Mol Cell *44*, 252-264.

Viollier, P.H., Thanbichler, M., McGrath, P.T., West, L., Meewan, M., McAdams, H.H., and Shapiro, L. (2004). Rapid and sequential movement of individual chromosomal loci to specific subcellular locations during bacterial DNA replication. Proc Natl Acad Sci U S A *101*, 9257-9262.

von Diezmann, A., Lee, M.Y., Lew, M.D., and Moerner, W.E. (2015). Correcting field-dependent aberrations with nanoscale accuracy in three-dimensional single-molecule localization microscopy. Optica *2*, 985-993.

Voronina, E., Seydoux, G., Sassone-Corsi, P., and Nagamori, I. (2011). RNA granules in germ cells. Cold Spring Harb Perspect Biol *3*.

Wartlick, O., Kicheva, A., and Gonzalez-Gaitan, M. (2009). Morphogen gradient formation. Cold Spring Harb Perspect Biol *1*, a001255.

Wei, M.T., Elbaum-Garfinkle, S., Holehouse, A.S., Chen, C.C., Feric, M., Arnold, C.B., Priestley, R.D., Pappu, R.V., and Brangwynne, C.P. (2017). Phase behaviour of disordered proteins underlying low density and high permeability of liquid organelles. Nat Chem *9*, 1118-1125.

Wodarz, A. (2002). Establishing cell polarity in development. Nat Cell Biol *4*, E39-44.

Wright, C.S., Banerjee, S., Iyer-Biswas, S., Crosson, S., Dinner, A.R., and Scherer, N.F. (2015). Intergenerational continuity of cell shape dynamics in Caulobacter crescentus. Sci Rep *5*, 9155.

Yoshiharu, S., Kitaura, Y., and Kadota, Y. (2012). [Diversity of physiological functions of branched-chain amino acids]. Seikagaku *84*, 938-942.

Zhou, B., Schrader, J.M., Kalogeraki, V.S., Abeliuk, E., Dinh, C.B., Pham, J.Q., Cui, Z.Z., Dill, D.L., McAdams, H.H., and Shapiro, L. (2015). The global regulatory architecture of transcription during the Caulobacter cell cycle. PLoS Genet *11*, e1004831.